# Kinematic GNSS tropospheric estimation and mitigation over a range of altitudes

Samuel Robert Webb

Thesis submitted for the Degree of

Doctor of Philosophy

School of Civil Engineering and Geosciences

Newcastle University

February 2015

# Abstract

This thesis investigates the potential for estimating tropospheric delay from Global Navigation Satellite Systems (GNSS) stations on moving platforms experiencing a change in altitude. The ability to accurately estimate tropospheric delay in kinematic GNSS positioning has implications for improved height accuracy due to the mitigation of a major GNSS error source, and for the collection of atmospheric water vapour data for meteorology and climate studies.

The potential for extending current kinematic GNSS positioning estimates of tropospheric delay from sea level based studies to airborne experiments, and the achievable height accuracy from a range of tropospheric mitigation strategies used in airborne GNSS positioning, are explored. An experiment was established at the Snowdon Mountain Railway (SMR), utilising the railway to collect a repeatable kinematic dataset, profiling 950 m of the lower atmosphere over a 50 day period. GNSS stations on stable platforms and meteorological sensors were installed at the extremities of the trajectory, allowing reference tropospheric delays and coordinates to be established.

The retrieval of zenith wet delay (ZWD) from kinematic GNSS solutions using tropospheric estimation strategies is validated against an interpolated reference ZWD between GNSS stations on stable platforms, together with profiles from 100 m resolution runs of the UK Met Office Unified Model. Agreement between reference ZWD values and a combined GPS+GLONASS precise point positioning (PPP) solution is demonstrated with an accuracy of 11.6 mm (RMS), similar to a relative positioning solution and previous shipborne studies.

The impact on the height accuracy from estimating tropospheric delay in kinematic GNSS positioning is examined by comparing absolute and relative GNSS positioning solutions to a reference trajectory generated from a relative GNSS positioning solution

processed with reference to the GNSS stations on stable platforms situated at the extremities of the SMR. A height accuracy with a standard deviation of 72 mm was demonstrated for the GPS+GLONASS PPP solution, similar to a GPS-only relative solution, and providing an improvement over the GPS-only PPP solution.

# Acknowledgements

I would initially like to thank the individuals and companies that enabled the fieldwork undertaken in this research project: Snowdon Mountain Railway, and in particular Rob Dineen, for the use of the railway and support in setting up the experiment, the loan of GNSS receivers from Leica Geosystems, the loan of a Paroscientific model 745 sensor from Derek Noble at ETLG Ltd, and the technical support of Martin Robertson.

I would like to thank ESA for their orbit and clock products, JPL for the GIPSY software, and MIT for the Track software. NERC BIGF is acknowledged for the provision of GPS data. The project was enabled by financial support from a UK Natural Environment Research Council (NERC) studentship, and part of the work was funded by the Royal Institution of Chartered Surveyors (RICS) Education Trust.

The UK Met Office are thanked for the tropospheric delay values provided, with specific thanks going to Dr Stuart Webster for running the numerical weather model and offering technical advice, and Gemma Bennitt for providing technical descriptions of the retrieval of tropospheric delay values from the model.

Many thanks go to my supervisors Dr Nigel Penna and Professor Peter Clarke for their advice, guidance, and feedback on my research methods, analysis of results, and presentation of the work undertaken during this project. Ian Martin is acknowledged for his development of PPPNCL, and his advice while working with a kinematic GNSS dataset.

Finally, thanks to my family and friends for their support throughout the PhD.

# Table of Contents

# List of Figures

# List of Tables

# List of Abbreviations

| | |
|---|---|
| ACARS | Aircraft Communications Addressing and Report System |
| AIRS | Atmospheric Infrared Sounder |
| AMDAR | Aircraft Meteorological Data Relay |
| AMSR-E | Advanced Microwave Scanning Radiometer |
| ARM | Atmospheric Radiation Measurement |
| C/A | Coarse/Acquisition |
| CGNSS | Continuous GNSS |
| DD | Double Differencing |
| DOY | Day of Year |
| ECMWF | European Centre for Medium Range Weather Forecasts |
| EGNOS | European Geo-stationary Navigation Overlay System |
| EM | Electromagnetic |
| EOS | Earth Observation System |
| ESA | European Space Agency |
| ESOC | European Space Operation Centre |
| FKA | Federal Space Agency |
| FOC | Full Operational Capability |
| GIPSY | GNSS-Inferred Positioning System |
| GLONASS | Globalnaya Navigatsionnaya Sputnikovaya Sistema |
| GMF | Global Mapping Function |
| GNSS | Global Navigation Satellite Systems |
| GPS | Global Positioning System |
| GPT | Global Pressure Temperature |
| IAC | Information-Analytical Centre |
| IGS | International GNSS Service |
| InSAR | Interferometric Synthetic Aperture Radar |
| IOV | In-Orbit Validation |
| IWV | Integrated Water Vapour |
| JPL | Jet Propulsion Laboratory |

| | |
|---|---|
| LIDAR | Light detection and ranging |
| MODIS | Moderate Resolution Infrared Spectrometer |
| MERIS | Medium Resolution Imaging Spectrometer |
| NASA | National Aeronautics and Space Administration |
| NVAP | NASA Water Vapour Project |
| NWM | Numerical Weather Model |
| OLCI | Ocean and Land Color Instrument |
| OTL | Ocean Tide Loading |
| PPP | Precise Point Positioning |
| PWV | Precipitable Water Vapour |
| RO | Radio Occultation |
| RTK | Real-Time Kinematic |
| SESSYL | Station d'Etude des Systemes de Localisation |
| SET | Solid Earth Tide |
| SMR | Snowdon Mountain Railway |
| SSM/I | Special Sensor Microwave Imager |
| UNB3m | University of New Brunswick 3 modified |
| USNO | United States Naval Observatory |
| VLBI | Very Long Baseline Interferometry |
| WVR | Water Vapour Radiometers |
| ZHD | Zenith Hydrostatic Delay |
| ZTD | Zenith Total Delay |
| ZWD | Zenith Wet Delay |

# 1. Introduction

## 1.1. Background to study

The delay to incoming Global Navigation Satellite Systems (GNSS) radio waves due to tropospheric gases is one of the largest unmitigated error sources in kinematic GNSS positioning following recent improvements in determining satellite orbits and clocks. The zenith total delay (ZTD) is typically around 2.3 m at sea level, with 90% comprising the zenith hydrostatic delay (ZHD), and 10% the zenith wet delay (ZWD). The variations in the ZTD are predominantly due to high frequency spatial and temporal perturbations of atmospheric water vapour, with errors in the empirical modelling of the tropospheric delay being dominated by misrepresenting the ZWD (King, 2009). Parameterising the tropospheric delay in the kinematic GNSS positioning solution allows for the variations to be estimated and the delay mitigated, improving the height accuracy.

High accuracy kinematic GNSS positioning is required for aircraft data campaigns such as LIDAR and photogrammetry (Krabill *et al.*, 2002), with absolute GNSS positioning techniques improving the cost effectiveness and allowing data collection in remote areas. The tropospheric delay is of greatest consequence to the height component in any GNSS positioning solution, with unmitigated ZTD amplifying into the height error by typically a factor of three (Santerre, 1991). The mitigation of tropospheric delay to improve positioning quality (e.g. Saastamoinen (1972); Dodson *et al.* (1996); Bock *et al.,* (2001)) is well established for static GNSS positioning, but the mitigation in kinematic GNSS positioning is more complex due to the dynamics of the receiver and changing atmospheric conditions. The strategies used to mitigate tropospheric delay in kinematic GNSS positioning involve modelling or parameterisation. The accuracy of the height component for an airborne dataset is important due to the propagation of errors in the geo-referencing of a dataset (Skaloud, 2002); however, assessing the accuracy of airborne GNSS positioning is problematic due to the difficulty in establishing an accurate reference comparator. Previous studies into airborne GNSS

positioning solutions have compared different GNSS positioning solutions to each other (e.g. Choy *et al.* (2013)*;* Martin *et al.* (2013)) to assess the performance of a solution; but this can result in the masking of systematic errors in the GNSS positioning solutions.

Atmospheric water vapour is a key atmospheric gas in climatology and meteorology due to its role in the transfer of energy in the atmosphere and its impact on precipitation events, with observations required for monitoring and prediction purposes. The current global water vapour observation dataset is limited due to the available global coverage, latency of data, and weather dependent limitations of instruments such as satellite radiometers in cloudy conditions (Prasad and Singh, 2009). Precipitable water vapour (PWV) can be measured using GNSS by retrieving the ZWD through parameterising the ZTD, and modelling the ZHD with pressure and temperature measurements. The collection of water vapour data (e.g. Rocken *et al.* (1995); Byun and Bar-Sever (2009); Dousa and Bennitt (2013); Dousa and Vaclavovic (2014)) from GNSS stations on stable platforms has been well documented, and the assimilation of GNSS measured tropospheric delay into numerical weather models (NWMs) is an operational technique (Gutman *et al.*, 2004) but is limited in coverage due to the distribution of such GNSS stations. Kinematic GNSS positioning offers the potential to increase the coverage of PWV observations, but the validation of kinematic GNSS positioning to estimate ZWD for meteorology has to date been confined to shipborne studies for relative (Chadwell and Bock, 2001; Dodson *et al.*, 2001) and absolute (Rocken *et al.*, 2005; Boniface *et al.*, 2012) GNSS positioning solutions, and these have only used observations from the Global Positioning System (GPS). Estimating water vapour from a GNSS station on a moving platform over a variety of altitudes would allow the collection of tropospheric delay data in areas that are currently sparse in terms of GNSS stations on stable platforms, and provide profiles for mesoscale and microscale meteorology.

## 1.2. Aims and objectives

The current limitations in validating tropospheric mitigation, and sensing atmospheric water vapour from kinematic GNSS positioning over a range of altitudes (discussed in section 1.1) informed the aims and objectives of this thesis. Therefore the aims of this research are to benchmark the height accuracy attainable with different tropospheric mitigation methods used in airborne GNSS positioning, and to investigate the feasibility of using kinematic GNSS positioning over a range of altitudes to collect atmospheric water vapour data. To achieve the project's aims, the objectives of the research are as follows:

- Identify a suitable test platform that provides a repeatable trajectory through a range of altitudes (~ 1 km) in the lower atmosphere.

- Test a range of empirical tropospheric models used in commercial kinematic GNSS positioning, and benchmark the height accuracy offered by these models over a range of altitudes.

- Examine the use of kinematic GNSS positioning techniques, both relative and absolute, to estimate ZWD from a moving platform over a range of altitudes.

- Compare multi system combined GNSS using observations from GPS and the Russian Globalnaya Navigatsionnaya Sputnikovaya Sistema (GLONASS) and observations from a singular GNSS system (GPS-only) in kinematic precise point positioning (PPP) solutions for estimating ZWD.

- Investigate the impact of tropospheric mitigation on the overall height accuracy of kinematic absolute GNSS positioning, both relative and absolute, over a range of altitudes.

- Compare the overall height accuracy of multi system combined GNSS (GPS+GLONASS) to singular GNSS system (GPS-only) PPP solutions over a range of altitudes.

## 1.3. Chapter Outline

The nine chapters that form this thesis can be summarised as follows.

**Chapter 1** introduces the research that forms the thesis along with the aims, objectives, and motivations of the research.

**Chapter 2** explores the significance of atmospheric water vapour to climate and meteorology, with the structure of the atmosphere and the distribution of water vapour in the atmosphere detailed. Current methods to retrieve water vapour data are described and assessed in terms of their accuracy, latency, spatial resolution, global coverage, and availability.

**Chapter 3** presents an introduction to GNSS and outlines the major error sources impacting on the height accuracy, such as tropospheric delay. A review is undertaken of previous work using kinematic GNSS positioning for the retrieval and mitigation of the tropospheric delay.

**Chapter 4** states the requirements needed of a data set to address the project's aims and objectives. The experimental design using the Snowdon Mountain Railway (SMR) and the resulting dataset is described, along with the generation of a reference trajectory using spline fitting.

**Chapter 5** details how reference ZWD values are derived for the later validation of kinematic GNSS positioning estimates of ZWD. The chapter outlines the use of GNSS-Inferred Positioning System (GIPSY) to generate ZWD estimates for GNSS stations on stable platforms, extrapolation of pressure over the test site, the interpolation of ZWD

to the GNSS station on a moving platform, and the use of an independent ZWD dataset from a NWM.

**Chapter 6** tests the performance of a number of empirical tropospheric delay models. The empirical tropospheric models are described and the resulting temperature, pressure and delay estimates are analysed against the comparators described in Chapter 5.

**Chapter 7** undertakes an assessment of estimated ZWD from kinematic GNSS positioning over a range of altitudes. A comparison of ZWD estimates from the Met Office's Unified Model to the interpolated reference is also undertaken. The estimation techniques are validated over a range of height, and the retrieval of ZWD from a combined GPS+GLONASS PPP solution is compared to a GPS-only PPP solution. The results presented in this chapter feature in the submitted manuscript by Webb *et al.* (2014).

**Chapter 8** investigates the height accuracy of kinematic GNSS positioning solutions obtained using different tropospheric mitigation methods, using the SMR data set. The solutions were validated against the reference trajectory and the validation of height accuracy allow GPS-only and GPS+GLONASS PPP solutions to be compared.

**Chapter 9** summarises the research and the conclusions drawn from the research. Suggestions for further work building on the results provided in this thesis are included.

# 2. Atmospheric water vapour

Atmospheric water vapour is a key component of the atmosphere's composition. Its role in the transfer of heat in the atmosphere and precipitation is of great interest to climatologists and meteorologists. The refraction of water vapour on microwaves and the resulting errors on instruments and systems that use the radiation has also increased interest in atmospheric water vapour. In the following section the structure of the atmosphere, the consequence of water vapour on climate and weather, the interaction of microwaves with water vapour, and instruments that can measure water vapour will be explored.

## 2.1. Atmospheric structure

The neutral atmosphere can be considered to have four main zones, the troposphere, stratosphere, mesosphere, and thermosphere. The distinction between the different layers can be made by the temperature profiles that exist in each layer, which are related to pressure, solar radiation, and emitted thermal energy from the Earth. Layers in the atmosphere as well as the vertical temperature profile are reproduced from Wallace and Hobbs (1977) and displayed in Figure 2-12.

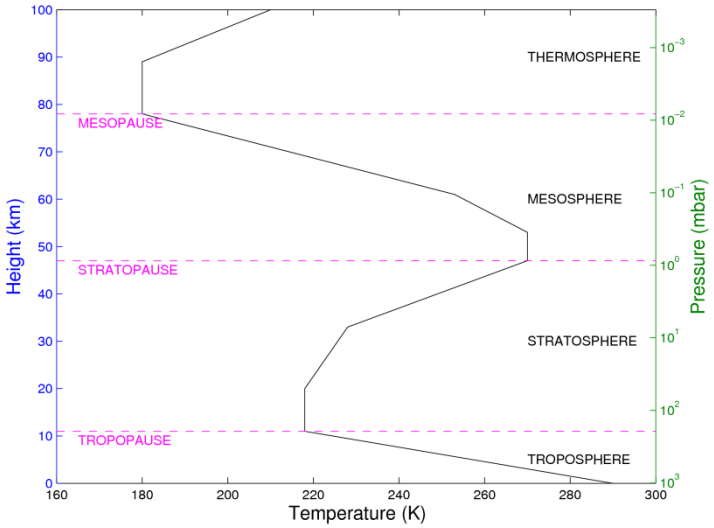


Figure 2-1. A vertical temperature profile (black line) of a standard atmosphere. The boundary layers between the atmospheric layers are defined in magenta.

### 2.1.1. Troposphere

The tropospheric layer can be characterised as having a temperature profile that generally decreases with altitude. This lowest layer of the atmosphere accounts for up to 80% of the atmospheric mass, with the vast majority of water vapour being in the troposphere. Due to the atmospheric temperature gradient, convection occurs, causing vertical mixing of the atmospheric particles leading to precipitation. The troposphere is capped by the tropopause, a layer of the atmosphere with a constant temperature, that defines where the atmosphere constituents change (there is very little water vapour above this layer), and where there is a lack of mixing between the lower, colder troposphere and the higher, warmer stratosphere.

### 2.1.2. Stratosphere

The stratosphere has a positive temperature gradient with height due to the absorption of ultra-violet radiation by ozone. The stratified structure of the atmospheric temperature results in a dynamically stable body of atmosphere with very little convection. The stratosphere upper boundary pressure is around 1 mbar meaning over 99% of atmospheric mass is contained within the troposphere and stratosphere.

### 2.1.3. Mesosphere and thermosphere

The upper atmosphere contains the mesosphere with a decreasing temperature with height, while the thermosphere has an increasing temperature with height that can reach up to 2000 K depending on the solar activity. The high temperature of the thermosphere is a result of the low density of atmospheric particles in the thermosphere such that very little energy is stored (the measurement of air temperature is a measure of the kinematic energy of air particles).

### 2.1.4. Ionosphere

The ionosphere is an electrically charged layer of the atmosphere and is situated within the upper atmospheric layers of the thermosphere and mesosphere, up to a height of 1000 km. The ionosphere is a result of radiated particles from the sun ionising atmospheric particles. The low density of particles in the upper atmosphere means that free ions and electrons do not recombine simultaneously, as occurs in the denser lower atmosphere. The resulting charged particles advance the GNSS carrier phase, and delay the modulated code. Due to the dispersive nature of refraction in the ionosphere first order effects can be mitigated by linearly combining signals on different frequencies, for example L1 and L2 in GPS processing (Petrie *et al.*, 2011).

## 2.2. Global distribution of atmospheric water vapour

The amount of atmospheric water vapour depends on the amount of evaporation and precipitation, with these processes balancing on a global scale. Due to the differences in the amount and strength of the sun's energy that the Earth's surface receives, and the spatial distribution of land and water bodies, there is an imbalance in the amount of evaporation and precipitation in localised areas. The greatest evaporation globally occurs in the subtropics, facilitated by the presence of oceanic anticyclones increasing exposure to the sun. Precipitation is generally greater than evaporation in the

equatorial zone and at latitudes greater than 40°, as a consequence of the monsoon (Wang and Ding, 2006) and baroclinic waves (Wallace *et al.*, 1988) respectively.

Water vapour is a key atmospheric component in the Earth's climate due to the transfer of heat. Water vapour does not absorb incoming shortwave radiation from the sun, but absorbs emitted infrared thermal energy from the Earth. Latent heat added to the atmosphere (resulting in evaporation) is converted to sensible heat (changing the temperature) when water vapour condenses (resulting in precipitation), fuelling thermal circulation.

Warm air can sustain more water vapour before becoming saturated. The global distribution of water vapour is therefore dependent on latitude. An example of the global total column water vapour, from a combination of radiosonde and passive satellite microwave and infrared sensor observations for July 2001, as provided by the NASA Water Vapour Project (NVAP) is displayed in Figure 2-2.

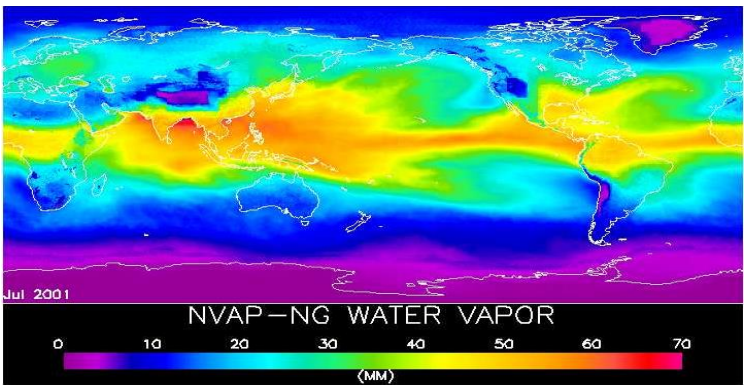


Figure 2-2. The global mean distribution of total column water vapour for July 2001 from NVAP (https://eosweb.larc.nasa.gov/PRODOCS/nvap/images/browse/index.html).

Due to the contribution of water vapour to the transfer of energy in the atmosphere, its distribution and concentration is of great interest to climate scientists and meteorologists. For meteorologists to forecast weather patterns, having knowledge of the amount of water vapour can enable modelling of the transfer of heat within the

atmosphere and resulting convection events, as well as having tangible estimates on the quantity of expected precipitation.

Water vapour is of great importance in long term climate studies due to the consequence of a warming planet leading to greater amounts of evaporation, which in turn leads to greater amounts of warming due to its part in atmospheric circulation. The consequence of a rise in air temperature is also expected to result in an increase in intense extreme precipitation events. The increase in extreme precipitation is a result of the Clausius-Clapeyron relationship where the atmospheric water holding capacity increases (Wentz and Schabel, 2000; Utsumi *et al.*, 2011; Berg *et al.*, 2013).

## 2.3. Relationship of ZWD to PWV/IWV

The amount of water vapour in a vertical column of the atmosphere is often described in GNSS literature as a distance, derived from converting the increase in time for a signal to reach a receiver (due to refraction from atmospheric gases) to a vertical distance, i.e. the zenith wet delay (ZWD). In climatology and meteorology, atmospheric water vapour is often described as integrated water vapour (IWV) or precipitable water vapour (PWV) or often simply PW. IWV is the mass of water vapour per unit area with units kg $m^{-2}$, while PWV is the equivalent height of a column of water with units in metres. IWV can be converted to PWV by simply dividing by the density of liquid water. ZWD can be related to PWV by the dimensionless constant $\Pi$ as described by Bevis *et al.* (1992) and shown in equations (2-1) to (2-3).

$$PW = \Pi \cdot \mathrm{ZWD} \tag{2-1}$$

With

$$\Pi = \frac{10^6}{\rho R_v[(k_3/T_m) + k_2']} \tag{2-2}$$

and

$$k_2' = k_2 - mk_1 \quad (2\text{-}3)$$

Where $\rho$ is the density of liquid water, $R_v$ is the specific gas constant for water vapour, $T_m$ the weighted mean temperature of the atmosphere, $k_{1-3}$ are refractivity constants and $m$ is the ratio of the molar masses of water vapour and dry air. An approximate value of $\Pi$ is 0.15.

## 2.4. Atmospheric water vapour sensing methods

There are numerous techniques and devices that are used to provide atmospheric water vapour data and products. The method used dictates the spatial coverage, temporal resolution, and spatial resolution of the dataset. The data collection techniques can be considered as satellite based global datasets and ground-based single point datasets.

### 2.4.1. Satellite based techniques

The satellite based retrieval of PWV from NASA's Earth observing system (EOS) satellites Aqua and Terra, and the ESA Envisat satellite, uses passive sensors that measure the absorption properties of reflected radiances by atmospheric water vapour in the thermal and near-infrared spectrum. It is also possible to measure radiance interaction with water vapour between satellites, as is the case of GNSS radio occultation.

#### 2.4.1.1. Passive instruments

There are a number of passive satellite based instruments that exploit the water vapour absorption spectral bands including the Atmospheric Infrared Sounder (AIRS), Moderate Resolution Infrared Spectrometer (MODIS), Medium Resolution Imaging Spectrometer (MERIS), Advanced Microwave Scanning Radiometer (AMSR-E), and

Special Sensor Microwave Imager (SSM/I). The use of different spectral bands, including methods based on microwave, solar reflectance and thermal-infrared, results in a range of spatial resolutions, with the shorter wavelength radiation offering higher accuracy but at the expense of the ability to collect data in cloudy conditions or at different times of the day. The low and constant emissivity of liquid water makes instruments measuring microwave radiation suitable for monitoring PWV over oceans. The SSM/I provide oceanic PWV estimates with a spatial resolution of 13 - 70 km, depending on the frequency, and RMS agreements of 3.7 mm to globally distributed radiosondes (Deblonde and Wagneur, 1997). The SSM/I campaign has been operational since 1987 so offers a long time series of global oceanic PWV measurements. The AMSR-E allows differencing of the separately measured polarised brightness temperatures; consequently PWV data can be collected over ocean and land areas. AMSR-E land based PWV values were found to have an RMS difference of 6 mm when compared to static GPS positioning solutions (Deeter, 2007), while oceanic PWV values are acquired with an absolute error of about 3.5 mm.

Instruments that measure emitted thermal-infrared and near-infrared radiation offer higher accuracy PWV measurements than the satellite microwave instruments. However, data collected in the infrared spectrum is not usable during precipitation events or with the cover of clouds due to the infrared radiation being absorbed. AIRS is one such instrument and is on-board the Aqua satellite (Parkinson, 2003), combining different absorption channels' radiance measurements along with additional channels measuring temperature to calculate a water vapour profile and PWV. Global coverage is achieved daily, with a spatial resolution of 13.5 km. Raja *et al.* (2008) undertook a six month comparison of AIRS PWV data, with PWV from a network of GPS stations on stable platforms around the USA and found an RMS agreement of 4 mm. Retrieval of PWV from AIRS has been found to be within 5% of the total PWV measured at a range of climatic sites situated in the tropics, central United States, and the Arctic when compared to ground-based water vapour radiometers (Bedka *et al.*, 2010). The accuracy of AIRS PWV can however be degraded for areas with small amounts of PWV where a moist bias can be introduced, as well as an underestimation for night time retrievals in mid-latitudes for moist atmospheres.

Along with AIRS, the MODIS instrument is on the Aqua satellite and employed on the TERRA satellite. MODIS makes measurements in the near-infrared spectrum with a spatial resolution of 1 km, and in the thermal band with a spatial resolution of 5 km. The near-infrared product provides PWV for land and ocean sun glint areas in the daylight, while the thermal product provides PWV for land and ocean regardless of the position of the sun but only with clear skies. MODIS PWV data collected over land was found to compare to PWV from static GPS positioning solutions and radiosonde with standard deviations of 1.4 mm and 2.2 mm respectively, with MODIS PWV overestimating in both comparisons (Li *et al.*, 2003), while Chen *et al.* (2008) found an RMS agreement of 3.3 mm between MODIS near-infrared and over 100 GPS stations on stable platforms across the USA. The near-infrared PWV estimates have also been shown to have large seasonal variability when compared to GPS PWV, with RMS biases ranging from 3.1 mm to 10.5 mm between winter and monsoon seasons (Prasad and Singh, 2009). Furthermore, Li *et al.* (2005) found a standard deviation of 1.6 mm for a comparison of MODIS to static GPS positioning solutions after applying an inverse distance weighted interpolation in the MODIS data to fill in cloudy pixels. The application of the cloud correction model resulted in a 22% increase of coverage for a series of scenes in Southern California.

There are a number of historical datasets such as MERIS on board the now expired Envisat satellite. The spatial resolution of the MERIS dataset was 0.3 km in full resolution and 1.2 km in reduced resolution, with agreement with static GPS positioning solutions estimates of PWV over a range of seasons of 1.1 mm standard deviation found by Li *et al.* (2006). Due to the MERIS instrument only measuring near-infrared, no measurements could be taken with cloud cover.

There are a number of planned satellite missions currently in development that will collect PWV from visible and near-infrared instruments, including the successor to MERIS, i.e. the Ocean and Land Color Instrument (OLCI) on the Sentinel-3 satellites (Diedrich *et al.*, 2013). OLCI will provide PWV with a spatial resolution of 0.3 km with global coverage achieved in four days. However, only upcoming satellite missions will

still have to deal with the consequence of the accuracy of PWV retrieval compared to the coverage achieved due to limitations of cloud cover.

An alternative technique from the satellite methods described above is the use of Interferometric Synthetic Aperture Radar (InSAR). InSAR is a widely used technique to monitor geophysical deformations (Li *et al*., 2011; Wen *et al*., 2012; Tomás *et al*., 2014), using a differential technique between repeat pass images (using the observed returned phase) to assess changes between the images. Due to using reflected microwaves the technique is affected by tropospheric delay. If the known baseline and topographic effects in a differential interferogram are removed, the change in the phase between the differenced data will be due to the variation in the tropospheric delay. Li *et al*. (2009) demonstrated an improvement in deformation mapping by integrating MERIS PWV data with a time series of interferograms. Due to measuring at microwave frequencies the InSAR technique overcomes the limitations of the MERIS sensor and is applicable at night and in cloudy conditions. The technique can provide sub-centimetre ZTD estimates at metre level spatial resolution, with the variation in ZTD mapped over a large area (~72 km).

#### 2.4.1.2. GNSS radio occultation

GNSS radio occultation (RO) observes the Doppler shift in the GNSS signal between a GNSS satellite and a GNSS receiver mounted on a low Earth orbiting satellite. The refractive index can be calculated and vertical profiles of pressure, temperature and water vapour content deduced. A benefit of GNSS RO is the ability to collect data in all weather conditions and over oceanic areas. To calculate PWV, ancillary temperature measurements are required. GNSS RO is a useful technique to derive temperature and pressure profiles in the atmospheric layers above the tropopause. However, it is problematic to separate temperature and water vapour estimates in the lower troposphere (von Engeln and Nedoluha, 2005) without additional atmospheric data. PWV can be calculated from RO by extrapolating through the lowest part of the troposphere as demonstrated by Teng *et al.* (2013), with RMS differences of 4 mm

compared to SSM/I and AMSR-E PWV ocean observations. Huang *et al.* (2013) also found a PWV bias between 1.5 mm and 2 mm, and a standard deviation of 3 mm between the RO COSMIC mission and the global GPS estimates from the International GNSS Service (IGS) and SuomiNet networks.

### 2.4.2. Ground-based techniques

Unlike the large spatial scale datasets that are available from satellite based techniques, ground-based techniques offer atmospheric samples from a single point. Through the use of networks of instruments, PWV estimates can be established over a local region or globally. Network datasets are therefore predominantly from ground-based monitoring sites. Due to the direct measurements employed and the positioning of instruments closer to the troposphere, ground-based technique accuracies can be higher than the satellite based methods.

#### 2.4.2.1. Water Vapour Radiometers

Water vapour radiometers (WVRs) use the absorption properties of water vapour of EM radiation around 22 GHz to observe the atmosphere temperature brightness. Two frequencies are used to separate the contributions to the temperature brightness from water vapour and liquid water (stored in clouds). PWV measurements can be calculated from the radiated energy by a tuned radiative transfer model from an ensemble of radiosonde profiles. The combination of errors from calculating the radiative transfer model and instrument noise is between 0.5 mm to 0.3 mm PWV, depending on the frequencies available (Cadeddu *et al.*, 2013).

The WVR global coverage is sparse with the Atmospheric Radiation Measurement (ARM) program providing five continuously operating sites at Oklahoma, USA; Alaska, USA; Darwin, Australia; Manus Island, Papua New Guinea; Denigomodu, Nauru; along with three mobile sites that can be re-located (Cadeddu *et al.*, 2013). There are also operational WVRs at sites at Onsala, Sweden (Emardson *et al.*, 1999; Elgered *et al.*,

2012) and at Wettzell, Germany (Bender *et al.*, 2008). WVRs have also been widely used for short period site specific studies to validate alternative column water vapour estimates from GPS, very long baseline interferometry (VLBI), and NWM (Liou *et al.*, 2000; Niell *et al.*, 2001; Teke *et al.*, 2013). However the technique has not been widely deployed due to the cost of the instruments, the requirement of radiosonde data to provide an accurate conversion from measured temperature brightness to PWV, and the consequence of scattering from liquid water on the observations, resulting in data not being able to be collected when there is precipitation.

#### 2.4.2.2. Sun photometers

Sun photometers or radiometers are passive instruments that measure the spectral transmission of the solar irradiance at 940 nm wavelength (Halthore *et al.*, 1997). Instruments are globally distributed in the AERONET (Holben *et al.*, 1998) programme, providing PWV profiles at a temporal resolution of 15 minutes and at an RMS accuracy of 0.5 mm when compared to static GPS positioning solution estimates of PWV (Bokoye *et al.*, 2007). The limitations of sun photometers are the requirements of a cloud free sky to collect data, and the collection in daylight.

#### 2.4.2.3. Very Long Baseline Interferometry

VLBI measures emitted microwave radio waves from astronomical bodies to calculate a relative position between two VLBI stations on stable platforms measuring the same emitting body. The troposphere refracts the incoming radio waves and causes a propagation delay similar to that experienced in GNSS. To mitigate the tropospheric delay, a correction for the residual tropospheric delay is estimated (Herring *et al.*, 1990). Similarly to GPS, mapping the delay to the zenith is important (Boehm *et al.*, 2006b). To retrieve PWV from the total delay, in-situ pressure measurements are used to calculate ZHD, and temperature data to transform from an integrated delay to PWV.

Haas *et al.* (2010) showed agreement between VLBI, radiosonde, and WVR data of 2 mm PWV over a 24 year test period at a single site, the Onsala Space Observatory. A five year comparison of PWV from 14 global VLBI stations and co-located GPS datasets was also carried out by Jin *et al.* (2009), with VLBI found to underestimate PWV by between 0.8 and 2.2 mm. VLBI offers high accuracy PWV measurements, but the resulting PWV is only really of use as a comparator for co-located instruments rather than for assimilation into weather and climate models, due to the low number of operating sites (with this unlikely to increase by a significant number due to the high cost of establishing and operating a VLBI), and the non-continuous nature of measurements.

#### 2.4.2.4. Raman LIDAR

Raman light detection and ranging (LIDAR) instruments emit radiation to measure the backscattering from water vapour (408 nm) and nitrogen (387 nm), allowing the water vapour mixing ratio to be calculated (as mass of water vapour divided by mass of dry air). PWV can be deduced from the mixing ratio by integrating as a function of altitude and using meteorological measurements, primarily from radiosondes. A Raman LIDAR does not sample through the entire atmosphere but relies on receiving back scattered signals. In dry cold conditions, Gerber *et al.* (2004) found that samples could only be collected up to an altitude of ~6 km with the instrument situated at ~3.5 km, though Ferrare *et al.* (1995) found that in different atmospheric conditions profiles were available to 9 km. Whiteman *et al.* (2006) obtained standard deviations of ~6.5% for mixing ratio data when compared with static GPS positioning solutions derived PWV estimates. However, even though the system offers high accuracy water vapour measurements, the cost of the instrument limits its use to calibration and site specific field work.

#### 2.4.2.5. Radiosondes

Radiosondes offer a direct measurement of water vapour, so can provide a near vertical (dependent on wind) profile of the atmosphere. Ray-tracing through the pressure and temperature profiles as outlined in Davis *et al.* (1985), or integration of the mass mixing ratio (Glowacki *et al.*, 2006), can provide PWV estimates. There are around 1500 radiosondes at sites distributed globally (Durre *et al.*, 2006), with certain sites offering time series of atmospheric data over 50 years. Included in these 1500 sites are 24 currently operational radiosondes at sites in the UK (http://badc.nerc.ac.uk/view/badc.nerc.ac.uk__ATOM__dataent_ABER, accessed July 2014). The spatial distribution of the sites' locations is skewed to the northern hemisphere where the greater land coverage is situated, along with large data gaps in the African continent. The temporal resolution varies between sites but typically there are only one to two launches a day.

Bruegge *et al.* (1992) outlined certain errors in the retrieval of column water vapour from radiosondes, such as the effect of freezing and the later latent heat release affecting the humidity probe, the different time lags between wet and dry bulb temperature measurements, and the lack of sampling of the upper atmosphere. Liu *et al.* (2000) estimated the overall uncertainty of PWV estimates from radiosondes to be ± 1.3 mm; as a combination of approximation and observation errors.

Variations in different humidity sensors used on radiosondes can also result in a range of uncertainties from global moisture measurements (Kuo *et al.*, 2005). Wang and Zhang (2008) tested 14 different types of radiosonde, and when compared to static GPS positioning solutions, found a range of biases between instruments with negative and positive biases of ~1 mm PWV depending on the sensor type used. The widely used Vaisala RS92 radiosonde's humidity sensor has also been shown to have a dry bias of 9% at the surface, increasing to 50% at 15 km altitude (Wang *et al.*, 2013), as a consequence of solar radiation heating of the humidity sensor (Vomel *et al.*, 2007).

#### 2.4.2.6. GNSS meteorology

The use of GNSS as a meteorological data collection technique has been envisaged for over 20 years as outlined in Bevis *et al.* (1992), with the estimation of zenith total delay (ZTD) with GNSS, from which the ZWD may be obtained by using pressure data to estimate ZHD, and then the ZWD converted to PWV. In the intervening years there have been numerous regional (e.g. Thomas *et al.,* 2011)) and global (e.g. Heise *et al.,* 2009) assessments of GNSS derived PWV. GNSS water vapour products have also been assimilated into NWMs with positive results (Poli *et al.*, 2007; Bennitt and Jupp, 2012), have been used to validate alternative column water vapour measurements (Liu *et al.*, 2006), have been used to validate NWMs (Vey *et al.*, 2010), and acted as a correction method to scale radiosonde water vapour profiles (McMillin *et al.*, 2007). Due to the retrieval of atmospheric water vapour from kinematic GNSS positioning being the main focus of this thesis, the use of GNSS ZTD estimates in static and kinematic modes for the purpose of mitigating and measuring tropospheric delay are discussed further in Chapter 3.

## 2.5. Summary

Atmospheric water vapour is a key observable for weather forecasting and climate prediction. The magnitude and distribution of water vapour has a consequence on the transfer of heat in the atmosphere and can be an indicator of climate change. There are limitations in the global observation dataset of atmospheric water vapour due to poor spatial sampling, instrument constraints, absolute accuracy, and latency. A combination of techniques is therefore required to maximise the amount of available data, but with close attention needed to be given to the biases between different techniques.

# 3. Kinematic GNSS positioning

Atmospheric water vapour and GNSS are intrinsically linked due to the propagation of GNSS signals through the troposphere. For positioning applications the delay caused from water vapour is an error that must be mitigated, but if the magnitude of the delay can be defined by a GNSS positioning solution, this error can then become a desirable signal for meteorology, due to the column water vapour magnitude in the atmosphere being deduced. Tropospheric delay maps directly into the height of GNSS positions, and is one of the major error sources in airborne GNSS positioning. The ability to accurately account for the ZWD in kinematic GNSS positioning should reduce the height error, and would extend the potential of GNSS meteorology to a variety of moving platforms providing high temporal measurements of ZWD, in all weather conditions, and the ability to profile the atmosphere.

A summary of GNSS theory will be presented including errors and processing strategies. Previous work on retrieving ZTD from GNSS for sensing and mitigation purposes will then be reviewed. The work presented in section 3.2.2 is included in the submitted manuscript Webb *et al.* (2014).

## 3.1. Overview of GNSS theory

### 3.1.1. Available systems

There are currently two fully operational GNSS offering global coverage, the American military operated GPS, and the Russian operated GLONASS. There are also a number of other GNSS in development designed to offer global coverage, including the Chinese BeiDou and European Galileo systems. Combining multiple GNSS observations offers redundancy into a solution and increases the potential of receiving satellite signals. However, the validation of multiple GNSS observations in kinematic positioning and atmospheric sensing has so far been limited. The retrieval of ZWD and the height

quality from a kinematic multi-GNSS solution and a single system solution will therefore be assessed in Sections 7 and 8.

#### 3.1.1.1. GPS

The United States Department of Defense operated Global Positioning System consists of at least 24 operational satellites (up to 32 satellites providing redundancy to keep the system at full operational capability (FOC)) orbiting in six planes, all inclined at an angle of 55° to the equator and with equally separated ascending nodes. Each satellite completes two revolutions per sidereal day, with the satellite constellation repeating for a GNSS station on a stable platform four minutes earlier each day. 'Legacy' signals are broadcast for each satellite on the L1 and L2 bands at frequencies of 1575.42 MHz and 1227.60 MHz respectively. Known pseudo-random sequences unique to each satellite are modulated onto the carrier frequencies. There are two 'legacy' sequences available, the civilian course acquisition (C/A) code, and the encrypted military P(Y) code, which has an order of magnitude higher transmission rate. A navigation message is also broadcast on each frequency with orbit, clock, almanac and health information for the user.

#### 3.1.1.2. GLONASS

The Russian operated GLONASS constellation operates at FOC with 24 satellites in three orbital planes, inclined at an angle to the equator of 64.8°. The system first gained FOC in 1995 but the system was not maintained and the number of satellites dropped to just six in 2001. In the last decade an increase in funding has seen the system reach global FOC again in 2011 (Groves, 2013). The GLONASS satellites broadcast in the L1 and L2 band but each satellite broadcasts on a separate frequency. The L1 frequencies are centred around 1602 MHz, and the L2 frequencies around 1246 MHz, with the division following the frequency division multiple access (FDMA) method and protocol. Due to the frequency of each signal being unique, satellites can be identified accordingly, and therefore the same pseudo-random code can be

modulated onto each carrier frequency. Similar to GPS, a civilian and encrypted signal is encoded onto the broadcast signals.

#### 3.1.1.3. Future: BeiDou and Galileo

There are a number of GNSS initiatives currently in development aiming to provide global coverage including the Chinese BeiDou system and the European Galileo system. Both of these are currently in development and so, even though data from these systems are not used in this thesis, the systems will be described as they should have a positive impact on height and tropospheric estimation, due to increased satellite availability and the potential of combining signals for real-time GNSS applications.

Galileo will be a 30 satellite system orbiting in three planes inclined at 56° to the equator and with an orbit repeat time of 14 hours 4 minutes and 45 seconds. Ongoing in-orbit validation (IOV) is currently being carried out with four Galileo IOV test satellites and initial results from the test constellation have established a Galileo only position fix from the four IOV satellites (Goode *et al.*, 2013). Positive results have also been seen by the incorporation of Galileo and GPS signals in a single parameter estimation process, with a reduction in noise in the E5 band (Springer *et al.*, 2013). Galileo has two operational satellites built and waiting deployment in late 2014, with the initial Galileo constellation currently forecast to reach global FOC in 2020.

The Chinese government funded BeiDou system will consist of five geostationary satellites, 27 medium Earth orbit satellites, and three geosynchronous orbit satellites. Signals are broadcast at three frequencies, with two open bands and one restricted band. There are currently thirteen satellites available at the IOV stage, with the distribution of the satellites enabling system testing over the Asia-Pacific region, with initial positive results from the use of triple frequency combination in ambiguity fixing in relative positioning (Montenbruck *et al.*, 2013).

### 3.1.2. GNSS concept

GNSS systems use trilateration to calculate a position. Distances are calculated by measuring the time for the known modulated code to travel between the satellite and receiver. The frequency of the modulated code and length of message dictates the best possible precision of a measured distance, which for the C/A code used in GPS equates to 3 m. Due to errors in the satellite and receiver clocks the calculated distance is known as the pseudorange. A minimum of four observations are required to solve for the three unknown coordinate positions, and a correction to the error in the receiver clock.

To allow for more precise measurements the number of cycles of the incoming carrier wave must be established. The shorter wave length of the carrier wave compared to the modulated code allows for an improvement in precision in establishing the range between receiver and satellite and is known as the carrier phase observable.

### 3.1.3. Error sources

Due to the similar methods used within all GNSS the same error sources are experienced in each system. The error sources in GNSS will be described, with the errors grouped into random and systematic effects.

#### 3.1.3.1. Random errors

Error sources that vary in magnitude and sign and do not follow a pattern in their distribution are considered random errors. They are referred to as random due to unpredictable variations in the driving forces behind the signals. The precision of measurements are affected by random errors, therefore the error can be reduced by averaging from a large sampled dataset. In GNSS positioning solutions the current sources of random error can be considered to occur from signal noise and human error.

With every set of observations there will be a certain amount of uncertainty (or noise) in a measurement due to constraints of the system. In pseudorange measurement the signal noise is dictated by the resolution of the C/A code, while for carrier phase measurement it depends on the wavelength of the carrier frequency. The observation type being used will influence the magnitude of the signal noise.

In the collection of any dataset the operation of the instrument also has to be considered. Errors can arise in GNSS positioning from unstable mounts, errors in antenna height measurements and incorrectly centred antennas. To minimise the consequence of human errors on a GNSS field work campaign, a detailed station checklist and a record of station metadata should be undertaken.

#### 3.1.3.2. Systematic errors

Systematic error sources are caused from a physical attribute, a hardware issue, or a limitation in the computational algorithm (e.g. Stewart *et al.*, 2005). If the contributing factor can be understood and mathematically modelled, the error can be mitigated. With systematic errors the accuracy of the measurements are affected, whereas the precision of the measurements is maintained. Systematic errors propagating from the satellite, signal transmission, and receiver segment will now be reviewed.

Satellite errors (clock, orbits, attitude, and satellite antenna phase centres)

Errors are introduced into the overall GNSS positioning error budget from the satellite segment due to errors in the modelling and estimation of the satellites' orbits and clocks. Due to the trilateration method used to compute position, any error in the satellite orbits directly propagate into the estimated coordinates. Satellites deviate from their predicted orbit positions (embedded in the satellite navigation message) due to errors in the tracking data, and un-modelled forces such as solar radiation pressure, tidal field, and infrared radiation from the Earth (Colombo, 1986). GNSS satellites use atomic clocks for the high accuracy required to establish the time for a signal to travel between satellite and receiver.

Orbit and clock offsets can be estimated from global networks of GNSS stations on stable platforms. The IGS distribute post processed orbits from 12 IGS Analysis Centres using a range of independent solutions at a range of accuracies from 25 mm to 50 mm depending on the temporal latency. Ultra-rapid, rapid, and final IGS orbit products are available within 3 hours, 17 hours, and 13 days respectively (Dow *et al.*, 2009). All the orbits and clock offsets from the IGS Analysis Centres are of a higher accuracy than the broadcast ephemeris data in the navigation message, which is around ~1.0 m and ~5 ns, compared to ~0.10 m and 3 ns for ultra-rapid and 0.025 m and 0.075 ps for final orbits (http://igscb.jpl.nasa.gov/components/prods.html, accessed December 2014).

Currently two IGS Analysis Centres are providing GPS+GLONASS orbit and clock products, the European Space Agency (ESA) European Space Operation Centre (ESOC) and the Russian Federal Space Agency (FKA) Information-Analytical Centre (IAC). Commercial service providers such as Veripos and Fugro also offer GPS+GLONASS orbit and clock products to their clients, and GMV provide combined orbit and clock products for their online MagicGNSS service (Píriz *et al.*, 2009). Furthermore, since April 2013 the IGS also provide real-time orbit estimates and Hadas and Bosy (2014) compared these real-time orbits to ESA final orbits and found agreement of 48 mm and 132 mm for GPS and GLONASS respectively.

The attitude of a satellite is also important in order to enable solar radiation pressure effects to be modelled for orbit determination and to correct phase wind-up. To relate measurements to the centre of mass of the GNSS satellite (Kouba, 2009), the antenna phase centre eccentricity must be known and uncertainties in these can be the largest error. For GPS II/IIA satellites, the antenna phase centre offset is 0.279 m in the X-plane; whereas, for GPS IIR-M satellites this antenna phase centre offset in the X-plane is minimal, therefore the eccentricity error does not exist. However for GPS IIF satellites there is once again an antenna phase centre offset of 0.394m in the X-plane.

Atmospheric refraction

The atmosphere refracts incoming GNSS signals, introducing a delay (or advance) to the GNSS signal. The delay (or advance) can be considered as separate values from the charged ionosphere and the neutral atmosphere. The ionosphere, which is described in section 2.1, delays the pseudorange and advances the carrier phase. The error from the ionosphere can be up to 100 m if not appropriately modelled for single frequency receivers. For precise applications the combination of the L1 and L2 frequencies allows the first order effects of the delay to be mitigated due to the dispersive nature of the ionosphere. The troposphere is neutral and non-dispersive; therefore the delay cannot be mitigated with a combination of frequencies as with the ionosphere. Due to tropospheric delay being a main feature of the research it is reviewed in further detail in section 3.1.4.

Multipath

Multipath is the consequence of GNSS signals being reflected from surrounding objects around an antenna, as demonstrated in Figure 3-1. The consequence of a reflected signal is a non-direct signal, introducing a ranging error, along with interference of the phase and amplitude of the signal (Byun *et al.*, 2002). For signals reflected from the ground the use of an appropriate elevation cut off angle and an antenna ground plane can exclude these erroneous signals. For multipath affected sites, studies have also looked at mapping of the multipath environment (Bilich and Larson, 2007) and identifying reflected signals using the dual polarisation to exclude erroneous signals (Groves *et al.*, 2010). However, such multipath mapping and the identification of reflected signals by polarisation is only suitable for GNSS stations on stable platforms, and the environment in which any kinematic GNSS data is collected has to be carefully considered.

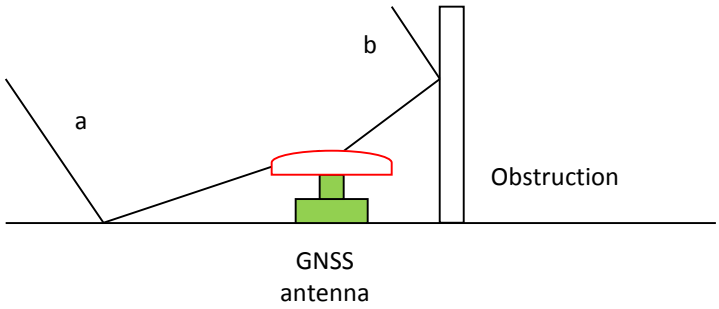


Figure 3-1. Diagram representing multipath scenarios from a) ground or mounting plate reflection, and b) local environment such as buildings.

Receiver antenna phase centres

The antenna phase centre is the point in the receiver antenna where a signal is received. This phase centre is dependent on frequency, elevation and azimuth of the incoming signal. A receiver dependent antenna phase centre correction model can be used to match the instantaneous antenna phase centre to the antenna's physical centre for each signal received. To enable this, antennas are calibrated with either robotic or anechoic chamber calibration methods (Gorres *et al.*, 2006), with the latest absolute calibration values available from the International GNSS Service (IGS) in the IGS08.atx file (http://igscb.jpl.nasa.gov/igscb/station/general/igs08.atx, accessed July 2014).

Geophysical signals

Geophysical processes causing movements of the Earth's surface also have to be considered in GNSS positioning, and can introduce errors into GNSS coordinates if the resulting signals are not modelled. Effects such as solid Earth tide (SET) and ocean tide loading (OTL) can result in (peak-to-peak) vertical displacements of around 800 mm (e.g. Baker, 1984) and 100 mm (Penna *et al.*, 2008) respectively, with the magnitude varying globally and changing slowly over time (with a dominant period of about 12 hours).

### 3.1.4. Refractivity and delay in the troposphere

The non-dispersive delay to GNSS radio waves from refraction caused by the neutral part of the atmosphere is often referred to as the tropospheric delay. This neutral layer of the atmosphere can reach from the surface of the Earth to a height of ~50 km (the upper stratosphere). The majority of the delay occurs in the bottom 3 km (the troposphere) of the atmosphere where the majority of atmospheric gases including atmospheric water vapour are found. The resulting tropospheric delay therefore refers to the section of atmosphere where the dominant contribution results from, although the term 'neutral atmosphere delay' is preferred by some authors (Leandro *et al.*, 2008). The diagram in Figure 3-2 shows the idealised GNSS signal path along a geometric straight line (G), and the refracted signal path (S).

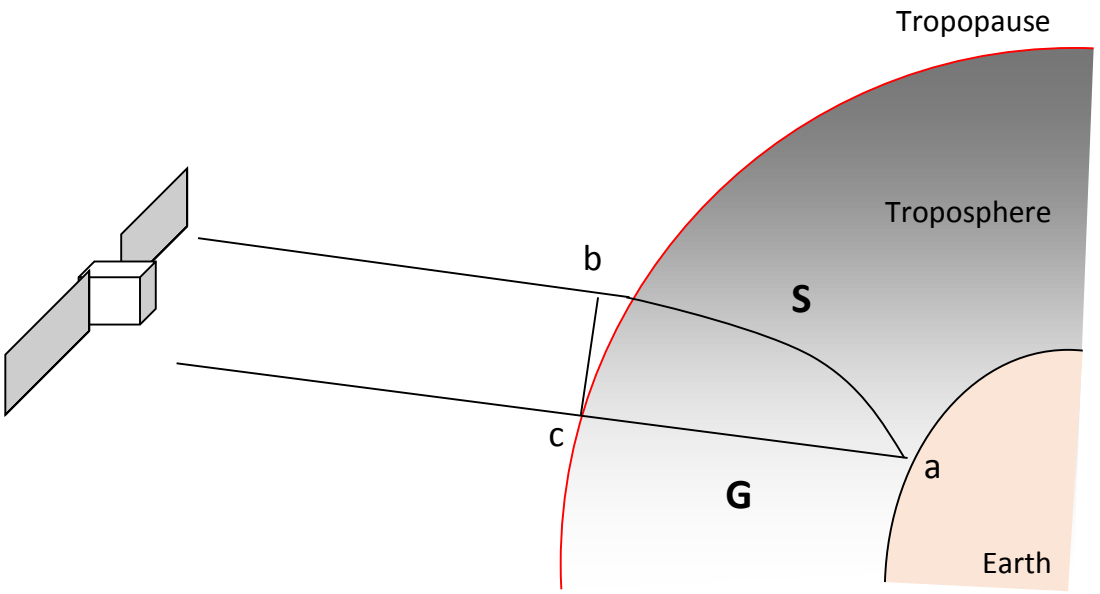


Figure 3-2. GNSS signal diagram highlighting idealised path (G) and realistic refracted path (S) through the neutral part of the atmosphere.

The idealised GNSS signal path along a geometric straight line (G) can be expressed as

$$G = \int_a^c dG \tag{3-1}$$

Due to the atmosphere not being a vacuum, the GNSS signal is refracted and follows path S. The time for light to travel between two points (which holds true for GNSS radio waves travelling between satellite and receiver) should be a minimum, and can be deemed to follow the minimum electrical path length (L)

$$L = \int_a^b n\, ds \tag{3-2}$$

Where $n$ is the varying refractive index of the atmosphere.

The additional path delay can be given by combining equations (3-1) and (3-2) as outlined in Dodson *et al.* (1996)

$$L - G = \int_a^b (n-1)\, ds + (S - G) \tag{3-3}$$

The first term of equation (3-3) relates to the larger atmospheric wave speed source of path delay, while the second term is the consequence of bending which is usually neglected. The tropospheric delay, $\Delta trop$, can therefore be defined by

$$\Delta trop = \int_a^b (n-1)\, ds \tag{3-4}$$

Due to the refractive index of microwave frequencies being close to 1, refractivity $N$ is used to describe the refraction occurring in the atmosphere.

$$N = 10^6(n-1) \tag{3-5}$$

When establishing refractivity the atmosphere can be considered to be comprised of two ideal gases, dry air and water vapour (Hopfield, 1971).

$$N = N_d + N_w \tag{3-6}$$

The refractivity depends on the densities of dry air and water vapour which can be defined by the ideal gas law:

$$\rho_d = \frac{p-e}{R_d T} \qquad \rho_w = \frac{e}{T R_w} \tag{3-7}$$

Where $p$ is the total pressure, $T$ the absolute temperature, $e$ the partial pressure of water vapour, and $R_d$ and $R_w$ are the gas constants for dry and wet air respectively. Therefore the total density of air can be represented as

$$\rho = \frac{p}{R_d T} - \left(1 - \frac{R_d}{R_w}\right)\frac{e}{R_d T} \tag{3-8}$$

If the atmosphere is assumed to be in hydrostatic equilibrium, the pressure measured at any height is equal to the weight of air within a vertical column from that height to the top of the atmosphere. If equation (3-8) is integrated this leads to

$$N = k_1\left(\frac{p}{T}\right) - k_2\left(\frac{e}{T}\right) + k_3\left(\frac{e}{T^2}\right) \tag{3-9}$$

The first term of equation (3-9) describes the sum of distortions from dry gases under the influence of an applied electromagnetic (EM) field, the second term the distortion

from water vapour, and the last term the effect of the orientation of the electric dipoles of water vapour under a field (Smith and Weintraub, 1953). Coefficients used in the Saastamoinen (1972) and Hopfield (1971) tropospheric models are listed in Table 3-1., due to the magnitude of the second term being small the Hopfield model omit it.

Table 3-1. Refractivity coefficients used in a range of tropospheric models.

| Method | $k_1$ $(K\ mbar^{-1})$ | $k_2$ $(K\ mbar^{-1})$ | $k_3$ $(K^2\ mbar^{-1})$ |
|---|---|---|---|
| Saastamoinen | 77.624 | 12.92 | 371900 |
| Hopfield | 77.607 ±0.013 | - | 374700 ±3100 |

The refractivity of the water vapour and dry air in the atmosphere can therefore be represented by

$$N_d = k_1 \left(\frac{p}{T}\right) \tag{3-10}$$

$$N_w = -k_2 \left(\frac{e}{T}\right) + k_3 \left(\frac{e}{T^2}\right) \tag{3-11}$$

The ZTD for a vertical column of air at a given height (h) can therefore be obtained from

$$ZTD = 10^{-6} \int_a^b N_d(h)\, dh + 10^{-6} \int_a^b N_w(h)\, dh \tag{3-12}$$

with the first term in equation (3-12) representing the zenith hydrostatic delay (ZHD) and the second term the zenith wet delay (ZWD).

It is apparent from equation (3-12) that ZTD, ZHD, and ZWD can be calculated if measurements of pressure, temperature and relative humidity (equivalent to partial pressure of water vapour) are available. If the ideal gas laws are assumed and the

atmosphere is in static equilibrium, ZHD can be modelled to millimetre level accuracy if appropriate surface pressure measurements are recorded (1 mbar error in pressure results in 2.3 mm of error in ZHD (Bevis *et al.*, 1992)). However, the accuracy of calculating ZWD from local meteorological measurements is poorer due to the extremely variable nature of partial water vapour pressure with height. The relative humidity is therefore often set to a mean value, though this can lead to errors, with an error of 5% in relative humidity resulting in a 12 mm ZWD error.

### 3.1.5. Processing methods

High precision, static GNSS positioning solutions can be computed by processing GNSS data from an unknown station relative to a known station. By differencing the observations made at each station the corresponding systematic errors can then be mitigated to some extent. An alternative approach is to model the systematic errors in GNSS (satellite orbit and clocks, antenna phase centres, SET, and OTL), and parameterise variable error sources (tropospheric delay) allowing an absolute position to be computed for a single station.

Kinematic GNSS positioning is more complex than static GNSS positioning due to not being able to assume that a position is fixed to a single location over a period of time. Kinematic GNSS positioning software usually uses a Kalman filter to estimate parameters with a changing state. Appropriate measurement and system process models are applied along with stochastic process noise to represent the behaviour of the parametric models. The modelling of position and velocity, clock offsets, and atmospheric delay form the dynamic model which aims to describe how a system will change over a period of time dependent on a set of observables. The recursive estimation of the current system state then aims to minimise the mean squared errors from the dynamic modelled predicted state and the current set of observations.

#### 3.1.5.1. Relative GNSS positioning

If multiple (two or more) receivers are observing the same satellites they will be subjected to the same error sources in each solution if the baseline length is short and receivers are at the same altitude. In this case by using two receivers, with one at a known station and one at an unknown station the observations can be differenced and the common errors removed.

The single baseline double-difference solution can be an effective approach for relative GNSS positioning up to 10 - 20 km where tropospheric and ionospheric conditions are similar at both stations. Over distances greater than 20 km, or when one station is at a significantly different height to the other station, the atmospheric conditions are different so the errors do not cancel out, resulting in a residual error and the need for tropospheric parameterisation. This approach can be used for both post-processing and also for real-time applications, with a radio transmitter required to broadcast the reference station's data for real-time kinematic (RTK) solutions.

Furthermore, A network approach allows a greater distance between the GNSS stations while keeping an accuracy of within 35 mm in height and 20 mm in plan (Edwards *et al.*, 2010) for RTK solutions as spatially variable errors are mitigated by interpolating the errors between GNSS stations on stable platforms that form the network.

Clearly, a limitation of all relative GNSS positioning solutions is the requirement of a known station, and the distance between the known station and unknown station being limited before solution accuracies are degraded. Relative GNSS positioning solutions are therefore not plausible for GNSS offshore positioning, impractical or expensive in mountainous and desert locations, and limited for airborne GNSS positioning due to the change in tropospheric effects with altitude.

#### 3.1.5.2. Absolute GNSS positioning

Absolute GNSS positioning refers to solution types where the unknown station's data are not processed relative to a known station, but use models and estimation procedures to mitigate error sources. Absolute code and carrier phase GNSS positioning is referred to as precise point positioning (PPP) and relies on the accurate generation of satellite orbit and clock products (Zumberge *et al.*, 1997). For real-time applications orbit and clock products can be disseminated by either geostationary communication satellites or internet links.

For real-time solutions, PPP requires carrier phase ambiguities to have converged to either estimated floating points or fixed integer values using ambiguity resolution, with the duration depending on satellite visibility geometry, receiver dynamics, and observation quality (Bisnath and Gao, 2009). Ambiguity resolution has been shown to reduce convergence time and improve positional accuracy in GPS-only PPP (Li and Zhang, 2014; Pan *et al*., 2014) compared to estimating a float ambiguity value, with further improvement demonstrated with the inclusion of GLONASS observations when fixing GPS ambiguities. The combined GPS+GLONASS solutions fix ambiguities for the GPS observables, but due to inter-frequency biases from the use of FDMA, the GLONASS ambiguities are kept as float values. If there is a loss of lock onto satellites then the solution will have to reinitialise and the convergence period will start again. However, for post-processed PPP solutions a back-smoother can be applied, overcoming such convergence problems.

Provided that satellite orbits and clocks are available a benefit of PPP is the global coverage it offers as it is not constrained to be relative to a known station. However, for real-time applications PPP convergence and re-convergence can be a significant limitation if working in an environment with a large number of obstructions or instances of loss of lock. A selection of available PPP software is displayed in Table 3-2.

Table 3-2. A review of a selection of available PPP software's

| | GNSS observations | Static/Kinematic | Institute | Online service |
|---|---|---|---|---|
| GIPSY | GPS | Static | JPL/NASA | APPS |
| Bernese | GPS+GLONASS | Static | Uni. of Berne | - |
| PANDA | GPS, GLONASS, Bediou | Static | Wuhan Uni. | - |
| PPPNCL | GPS+GLONASS | Static & Kinematic | Newcastle Uni. | - |
| NRCAN | GPS+GLONASS | Static & Kinematic | Natural Resources Canada | CSRC-PPP |
| GAPS | GPS | Static & Kinematic | Uni. Of New Brunswick | GAPS |
| CNES | GPS+GLONASS | Static & Kinematic | Centre National d'Etudes Spatiale | PPP-Wizard |
| Magic | GPS+GLONASS | Static & Kinematic | GMV | MagicGNSS |

## 3.2. Estimation of ZTD in GNSS

### 3.2.1. Static GNSS positioning ZTD estimation

The estimation of tropospheric delay in relative GNSS positioning was developed and outlined in papers such as Tralli *et al.* (1988), Dixon and Wolf (1990), and Wolfe and Gutman (2000). The estimation of tropospheric delay removed the requirements for co-located WVR measurements to mitigate tropospheric effects in order to achieve the highest accuracy positioning. In the estimation approach, the dry component of the delay is modelled with a standard atmospheric model, with any residual dry and wet delay estimated as a parameter in a least squares batch or Kalman filter solution.

The relationship between tropospheric delay and PWV and the potential for static GNSS relative positioning to be used as a meteorological data source was outlined in Bevis *et al.* (1992). For post-processed applications it has been shown that it is possible to derive ZTD to within 5 mm when compared to WVR or NWM (Bock *et al.*, 2001; Ning *et al.*, 2012; Teke *et al.*, 2013), and with suitable pressure and temperature measurements, ZWD within the same accuracy is available. Agreement between post-processed PPP and radiosonde PWV estimates has also been demonstrated, with a mean difference of 1.1 mm and a standard deviation of 2.7 mm for 98 IGS stations over an eight year period, using interpolated pressure from nearby synoptic sites, and temperature from the NCEP/NCAR reanalysis (Wang *et al.*, 2007). Ge *et al.* (2002) showed that radial orbit errors have the greatest effect on zenith total delay (ZTD) estimation, resulting from biases in the orbital semi-major axis and eccentricity. For example, a 1 m orbit error in the radial direction can result in a 15 mm bias in ZTD, therefore an orbital accuracy of better than 0.4 m in the radial direction (and 1 m in the other orbital components) is required to retrieve ZTD within 6 mm (the accuracy needed to derive PWV within 1 mm) for a network solution.

A key component of GNSS water vapour estimates for meteorological forecasting purposes is latency. GNSS water vapour estimates for assimilating into NWM rely on ultra-rapid satellite orbit and clock products, with any errors in the orbits degrading

the tropospheric delay estimate. Rocken *et al.* (1997) achieved PWV estimates within 2 mm from a regional network of 16 GNSS station on stable platforms in the USA with a latency of 30 minutes for a 4 month campaign, validated against radiosonde and WVR measurements. Dousa (2001) also demonstrated a standard deviation of 1.2 mm for the GPS and radiosonde PWV differences for four European GNSS stations on stable platforms (with three hour latency).

The IGS has offered tropospheric delay products for its global network of continuous GNSS (CGNSS) stations since 1997. However, the initial delay products were limited due to inconsistencies between processing strategies between the IGS Analysis Centres. The IGS tropospheric product followed a standardised generation procedure between 2003 to 2011, as outlined in Byun and Bar-Sever (2009) using the National Aeronautics and Space Administration (NASA) Jet Propulsion Laboratory (JPL) PPP software GIPSY, with the accuracy of ZTD being within 4 mm with a 4 week latency using final orbits, and 6 mm with a 3 hour latency using ultra-rapid orbits. Since 2011, the IGS tropospheric product has been generated by the United States Naval Observatory (USNO) from a PPP solution using the Bernese GPS software (Byram *et al.*, 2011). Dousa (2010) examined the accuracy of satellite orbits required to achieve estimates of ZTD within 10 mm from both double-difference and PPP solutions and conclude that the radial error of orbits for PPP has to be within 10 mm to achieve 10 mm ZTD estimates. However, the orbital error can be absorbed by estimates of the satellite clock and phase ambiguities in PPP which allows the use of poorer orbit accuracies to still achieve an accuracy of 10 mm ZTD. Dousa and Bennitt (2013) implemented the delivery of hourly updated global GPS ZTD estimates for NWM assimilation purposes. The standard deviation between the near real-time ZTD estimates and post-processed ZTD estimates were between 3 - 6 mm and between 5 - 16 mm when compared to a radiosonde dataset.

In recent years the development of satellite orbit products has allowed the computation and delivery of high accuracy real-time tropospheric delay for a network of GNSS stations on stable platforms. Lee *et al.* (2013) demonstrated real-time

retrieval of PWV to agree with radiosondes to within 3.6 mm for a network of four GNSS stations and using IGS ultra-rapid orbits. For larger networks though, the computational expense and the long baselines for a global network is a limitation for the network double-difference approach. Since 2013, the delivery of real-time orbits from the IGS real-time service has allowed PPP to provide real-time solutions for GNSS stations on stable platforms. Li *et al.* (2014) validated a real-time PPP solution using the Earth Parameter and Orbit determination System – Real Time (EPOS-RT) software, using integer ambiguity fixing, through comparison of a co-located WVR and to post-processed GPS estimates for the SAPOS network, with PWV agreement of 2 mm and 1 mm respectively. Dousa and Vaclavovic (2014) also tested 36 globally distributed GNSS stations on stable platforms with PPP and IGS real-time orbits and found standard deviations of 6 - 10 mm in ZTD when compared to final orbit solutions. The initial results from real-time PPP ZTD estimation from GNSS stations on stable platforms (enabled from high quality orbits) have therefore been highly promising, with the accuracy of the results close to the 1 mm PWV required for NWM forecasting as outlined by the World Meteorological Organisation.

### 3.2.2. Kinematic GNSS positioning ZTD estimation

Besides the densification of networks of ground-based GNSS stations on stable platforms, another option to widen the availability of ZWD data is to use GNSS stations on moving platforms. Such platforms include ships, aircraft and trains, or dedicated devices tasked with the collection of atmospheric data, such as buoys or unmanned aerial vehicles. A moving platform approach would allow data collection where installing multiple meteorological sites is not practical, e.g. deep oceanic areas and deserts. Airborne platforms during ascent and descent from an airport could also offer additional vertical profiling constraints for high resolution NWMs aimed at delivering mesoscale and microscale meteorology.

The possibility of estimating ZWD from a GNSS station on a moving platform was first explored around a decade after its use for GNSS stations on stable platforms was first

introduced by Bevis *et al.* (1992). Kinematic GNSS positioning must deal with the dynamics of the moving platform, and being unable to constrain the position solution to a single location over a period of time reduces redundancy in the system, and therefore tends to worsen the accuracy of the estimated ZWD. Relative GNSS positioning solutions were first explored with 'levered' ZTD estimates (Rocken *et al.*, 1995), whereby the ZTD at the GNSS station on a stable platform is somehow known and fixed, and the difference in ZTD between this GNSS station and a GNSS station on a moving platform is then estimated. Dodson *et al.* (2001) considered a GPS unit on a moored boat, and used a levered approach over a short baseline of ~200 m to obtain an agreement of 1 - 2 mm in ZTD. Chadwell and Bock (2001) used a GPS buoy 8 km from a reference station, processed with a network equivalent double-differenced ambiguity-fixed solution, obtaining an agreement of 1.5 mm PWV with radiosonde launches 8 km away. Kealy *et al.* (2012) found agreement in PWV of 2.2 mm for the levered approach from a 10 day shipborne experiment around Hawaii with baseline lengths up to 120 km, but often shorter.

An alternative approach to a relative GNSS positioning solution is the use of absolute GNSS positioning or PPP. Rocken *et al.* (2005) used a post-processed three-step iterative kinematic PPP solution to analyse a two week long GPS dataset collected on a Caribbean cruise, and found RMS errors for PWV of 1.5 mm and 2.8 mm when compared with on-board radiosonde launches and WVRs respectively. Fujita *et al.* (2008) found a night-time agreement of 2.3 mm PWV for GPS and radiosondes over a two month period on a cruise ship. Boniface *et al.* (2012) compared four months of shipborne GPS PWV estimates from an RTnet PPP solution to MODIS and the ALADIN 10 km NWM, with an RMS agreement of 3.5 mm and 1.4 mm respectively. Skone *et al.* (2006) explored the use of an airborne platform in the collection of PWV from a real-time GPS-only PPP solution. GPS ZWD was collected from a single 15 minute upwards trajectory covering ~5500 m of height change. The GPS estimates were compared to ZWD extracted from the Canada Meteorological Center's Global Environmental Multiscale model, with agreement between methods of 10 - 20 mm ZWD.

## 3.3. Previous studies validating kinematic GNSS positioning

Sub-decimetre GNSS positional accuracy for GNSS stations on moving platforms enables direct georeferencing in photogrammetry and LIDAR applications (Skaloud, 2002), calibration of altimetry instruments (Cretaux *et al.*, 2011), and GNSS meteorology (Rocken *et al.*, 2005). However, validating kinematic GNSS positioning solutions is complicated due to the lack of a reference to compare against. It is common in studies of kinematic GNSS positioning quality to validate solutions against static GNSS positioning, allowing the optimal performance of the processing technique to be assessed. However, testing at GNSS stations on stable platforms lacks the dynamics experienced by a GNSS station on a moving platform and does not represent the conditions that such a station will be subjected to. Testing GNSS positioning solutions against other GNSS positioning solutions, such as absolute against relative GNSS positioning solutions, can also result in systematic errors in both solutions being masked.

Landau (1989) found an RMS position agreement of 20 mm for dual frequency carrier phase and code measurements with a double-difference positioning solution over a 6 km baseline. The validation method consisted of comparing solution coordinates at seven GNSS stations on stable platforms over a 3 km trajectory that were occupied at different times over one hour. Chen (1998) developed the kinematic double-difference positioning GPS software *Track* for post-processing of GPS and found agreement between trajectories of an aircraft of 30 mm in height while on the runway after a flight. A GPS and laser altimeter dataset was also collected over a lake and the derived height of the lake was compared from five overpass flights to a tide gauge derived lake surface height with an RMS scatter of 25 mm. Han and Rizos (2000) compared solutions for two airborne datasets with baselines less than 100 km and found a relative precision of 20 mm from comparing two solutions for the same antenna. A second airborne experiment was carried out to assess the effect of multipath on the solutions and used two antennas on the aircraft and compared the derived distance between the antennas. The computed difference between the receivers was found to vary by 0.1 m and interpreted as an error from multipath. It is

likely the solutions were being affected by multipath along with other unmitigated errors associated with long baseline GNSS. LIDAR data was collected on the dual antenna test to measure sea level as a form of control on the GPS solutions. The derived sea level height varies by ~0.5 m and is likely to be from noise in the LIDAR data, multipath, and unmitigated tropospheric delay.

The Station d'Etude des Systemes de Localisation (SESSYL) 180 m oval monorail described in Betaille (2003) was used to establish a reference trajectory by establishing reference control on the trajectory from static GPS positioning solutions. Fairhurst (2007) then tested an integrated GPS and INS system on the SESSYL reference trajectory and found centimetre level of accuracy from a short baseline (less than 100 m) double-difference positioning solution, and found the INS allowed the system to maintain the accuracy of the original estimate for 20 seconds when GPS observations were interrupted.

For kinematic GNSS positioning of moving platforms the reliance on a known station in relative GNSS positioning is a limitation due to the increase in error with the increase in distance from the known station. For applications in remote areas a GNSS station on a stable platform cannot always be established. PPP is an absolute positioning technique that has enabled high precision positioning in oceanic, desert, and mountainous areas where establishing GNSS stations on stable platforms is problematic. Gao and Shen (2004) tested kinematic PPP solutions on a land and airborne platform and found RMS agreement between absolute and relative GNSS positioning solutions of within 10 mm. The baselines of the trajectories were kept within 10 km in plan and 250 m in height and the solution was computed with real-time satellite orbit and clock products. Colombo *et al.* (2004) found a 3D RMS agreement of 55 mm between a post-processed kinematic PPP and double-difference positioning solution for a land based vehicle. Leandro *et al.* (2006) used the University of New Brunswick GPS data analysis and positioning software (GAPS) to create a kinematic PPP solution and compare this to a multiple known station double-difference positioning solution for an 80 km boat journey with RMS values in height of

139 mm. Flight, vehicle, and walking trajectories were collected and three (GAPS, NRCan, and MagicGNSS) online PPP software packages in kinematic mode were tested by Martín *et al.* (2012). Of the online PPP solutions tested, MagicGNSS offered the optimal result with the smallest mean bias of 30 mm in height. A post-processed kinematic PPP solution for a low flying (below 300 m) long range (up to 800 km) airborne dataset was compared to a commercial double-difference positioning solution and satellite altimetry by Zhang and Forsberg (2007), with GPS heights transferred to sea level by an on-board LIDAR. The kinematic PPP solution agreed to the kinematic double-difference positioning solution with a standard deviation of 110 mm and the altimetry data with a standard deviation of 300 mm as the use of non-specialised kinematic GNSS positioning software for long baselines without features such as tropospheric estimation introduces uncertainties in the accuracy of the reference trajectory. Marreiros *et al.* (2013) validated a shipborne kinematic PPP solution against a kinematic double-difference positioning solution with a standard deviation of 100 mm, and a mean difference of -10 mm. Sea surface measurements from kinematic PPP were also compared to altimetry data from the Envisat and Jason-1 satellite and showed a standard deviation agreement of 90 mm and 130 mm respectively.

Another development in kinematic GNSS positioning has been the incorporation of GPS and GLONASS observations. Moving platforms can experience changing environments with obstructed sky views; reduced satellite numbers is a major issue in kinematic GNSS positioning. Maintaining lock on satellites is important for real-time kinematic PPP due to the initialisation period for solutions to converge. The ability to use multiple GNSS observations increases the potential of receiving satellite signals and offers redundancy in a solution.

The use of combined GNSS signals in kinematic PPP solutions tested at GNSS stations on stable platforms have not seen a significant improvement in coordinate accuracy from the addition of GLONASS observations, but have seen an improvement in the convergence time (Hesselbarth and Wanninger, 2008; Li and Zhang, 2014). Recently

there have been a number of tests of GPS+GLONASS kinematic PPP solutions, but so far the validation techniques have only tested small sample datasets. Kjørsvik *et al.* (2009) undertook a 16 day ferry experiment during 2006 in a Norwegian fjord with a trajectory of 1.5 km comparing kinematic GPS-only and GPS+GLONASS kinematic PPP solutions to a kinematic double-difference positioning solution with standard deviations of 100 mm and 103 mm respectively in height. However, GLONASS was not at FOC and orbit and clock products were not available at a high rate in 2006. Martin (2013) demonstrated a reduction in convergence time from a kinematic GPS+GLONASS PPP solution in real-time mode with ESA final orbits and clocks. A similar total position error RMS of 30 mm was found for converged kinematic GPS-only and GPS+GLONASS PPP solutions when compared to a kinematic double-difference positioning solution for a two hour shipborne dataset with a baseline not exceeding 2.5 km. Anquela *et al.* (2013) tested post-processed kinematic GPS+GLONASS and GPS-only PPP solutions from MagicGNSS with a car based trajectory based on kinematic double-difference positioning with a maximum distance of 5 km from the known station. A reduction in the standard deviation for the kinematic GPS+GLONASS PPP solution in the height component was found, though the RMS increased. Cai and Gao (2013) found a reduction in convergence time for a kinematic PPP solution tested at GNSS stations on stable platforms with the inclusion of GLONASS, and found an improvement in each positional component with the inclusion of GLONASS when only a few GPS satellites were available during a two hour vehicle test. Choy *et al.* (2013) found an improvement from GPS+GLONASS for a post-processed kinematic PPP solution for an airborne data set, when compared to a kinematic GPS-only PPP solution, when validated against a reference trajectory from a kinematic double-difference positioning solution. The converged GPS+GLONASS positional accuracy offered an improvement on the kinematic GPS-only PPP solution with standard deviations of 45 mm and 53 mm respectively, and a reduction in the convergence time.

## 3.4. Summary

The estimation of tropospheric delay (and derived PWV) from GNSS positioning has become an important atmospheric water vapour data source, with a positive impact demonstrated from assimilation into NWM and calibrating alternative PWV techniques. The impact of global real-time GNSS estimates of PWV is putting further relevance onto the collection method. The collection of PWV from kinematic GNSS positioning on moving platforms, including aircraft, offers the possibility of retrieval in currently data sparse areas where ground-based GNSS stations on stable platforms cannot be established, and vertical profiling of the atmosphere at a high temporal accuracy.

The estimation and consequent mitigation of the tropospheric delay has also allowed an improvement in kinematic GNSS positioning. Previous studies validating kinematic GNSS positioning solutions have relied on comparisons to other static or kinematic GNSS positioning solutions, validating solutions post-trajectory to GNSS stations on stable platforms, or using LIDAR and tide gauge data. However, sample datasets have often only been for a few hours and consisted of a low number of trajectories.

# 4. Experimental design

A dataset was required to investigate the mitigation and sensing of tropospheric delay in kinematic GNSS positioning over a range of altitudes to accomplish the aim of this research. A test scenario with the ability to establish a reference trajectory, and reference tropospheric delay profiles, was paramount to allow the objectives outlined in Chapter 1 to be achieved.

A kinematic GNSS data set was required that would experience a variation in altitude (~1 km or greater) to simulate an airborne trajectory. For redundancy purposes the data set was desired to provide a repeatable trajectory over a period of several months to experience a range of atmospheric conditions. The location of the dataset also required the installation of GNSS stations on stable platforms and meteorological sensors at the extremities of the trajectory to establish reference tropospheric delay values. This chapter describes the selection and collection of the dataset, and the establishment of reference coordinates for the GNSS stations on both the stable and moving platforms. The establishment of reference tropospheric delay values will be described separately in Chapter 5.

## 4.1. Observational data set

### 4.1.1. Snowdon Mountain Railway

A train and railway was sought to establish the experiment, allowing repeated trajectories to be collected. Rail based platforms have been used in previous kinematic GNSS positioning studies to acquire repeated data sets (Fairhurst, 2007; Jakobsen and Pedersen, 2009). However, these datasets involved minimal height change, with coordinate variations predominantly in plan. Whereas, in this research a test scenario was required to enable the collection of a kinematic data set that varied in height, and sampled through a large section of the troposphere.

The Snowdon Mountain Railway (SMR) was chosen as a suitable test site. SMR is situated in Snowdonia National Park, North Wales, UK (Figure 4-1), and is a tourist railway taking customers to the summit of the highest mountain in Wales. The SMR had the potential to provide a moving platform that experiences a large height difference (from 115 m to 1065 m above mean sea level), and could also provide a train carriage for the GNSS station on a moving platform. The low starting altitude of the railway would allow profiling of the lower part of the troposphere where ZTD is at its greatest, and most of the atmospheric water vapour is contained, and the multiple repeat trajectories per day would ensure a large number of repeatable trajectories could be collected over the fieldwork campaign.

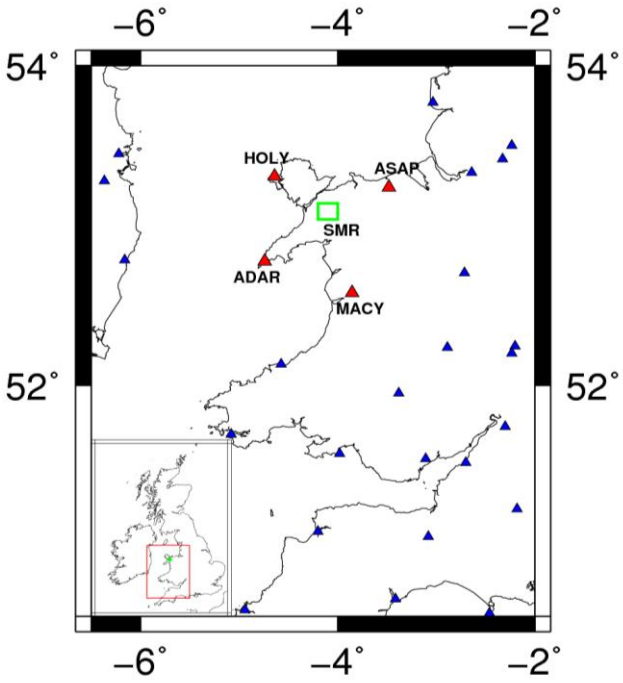


Figure 4-1. Location of SMR (marked with a green box) in comparison to the rest of the UK. OS CGNSS stations are displayed (triangle markers), with the stations used in the project highlighted in red.

The railway starts at Llanberis, North Wales (SNLB), at a height of ~115 m above sea level and reaches a height of ~1065 m near the summit (SNSU) of the mountain as shown in Figure 4-2 and Figure 4-3. From the start to the end of the railway is roughly 6 km in plan. The train travels at an average speed of 2.2 m $s^{-1}$ and never exceeds a

maximum speed of 3.4 m $s^{-1}$ due to an automated safety braking system used on the carriage. A journey on the train involves three stops on every ascent or descent at designated passing places, allowing multiple trains to use the railway at one time. The railway follows a single track apart from at the embarking and disembarking platforms at the termini of the railway, and at the passing places where the track splits into two sections. The train is stationary for roughly 30 minutes at the summit terminus and for a varying time span at the Llanberis terminus depending on the operating railway schedule.

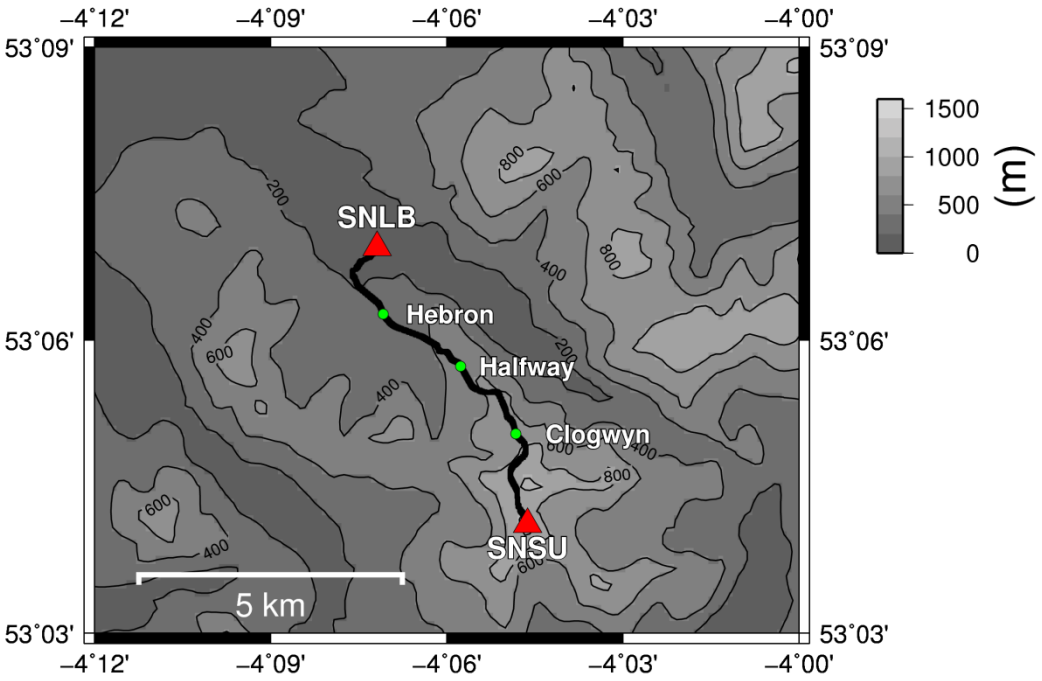


Figure 4-2. Location of the GNSS stations on stable platforms at Llanberis (SNLB, altitude 115 m) and Snowdon summit (SNSU, altitude 1065 m), the ~6 km trajectory of the SMR (thick black line), and the railway passing places (green circles) displayed on a topographic plot of the area.

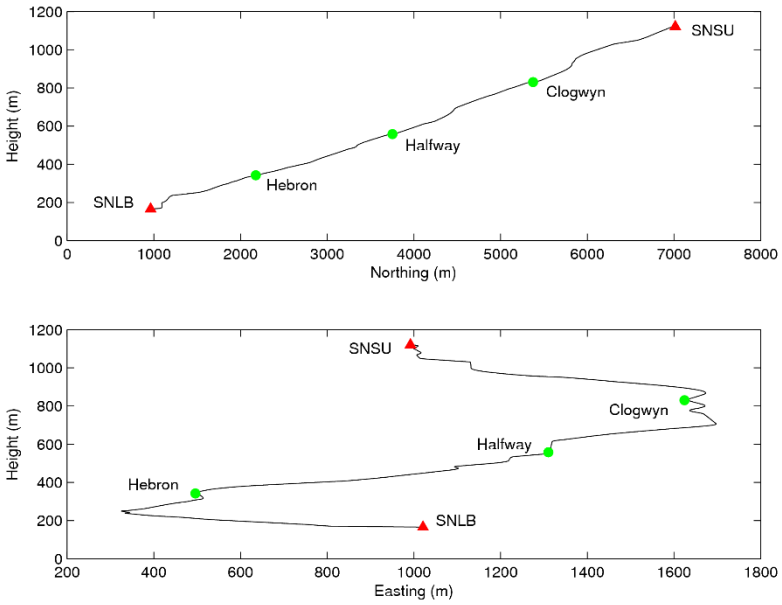


Figure 4-3. Height profile of the SMR trajectory (black line) plotted in a local Cartesian coordinate system against Northing (top pane) and Easting (lower pane). The railway termini SNLB and SNSU (red triangles), and the railway passing places (green circles) are also included.

GNSS stations on stable platforms were established at the extremities of the railway at the Llanberis terminus SNLB (Figure 4-4) on the roof of the SMR office building, and at the summit terminus SNSU (Figure 4-5) on an SMR equipment pole. A GNSS station on a moving platform was then created by using an antenna mounted on the roof of an SMR carriage (SNTR) as can be seen highlighted (circled in red) in Figure 4-6. The location of SMR in relation to nearby Ordnance Survey (OS) CGNSS stations can be seen in in Figure 4-1, with the height, and distance between the GNSS stations SNLB and SNSU and the OS CGNSS stations displayed in Table 4-1. The OS CGNSS stations were included as they allow testing of relative kinematic GNSS positioning solutions over baselines that are representative of distances experienced in airborne GNSS campaigns within the UK.

Figure 4-4. GNSS station on a stable platform (SNLB) with Leica AS10 GNSS antenna and co-located Met4 sensor.

Figure 4-5. GNSS station on a stable platform (SNSU) with Leica AS10 GNSS antenna and co-located Met4 sensor.

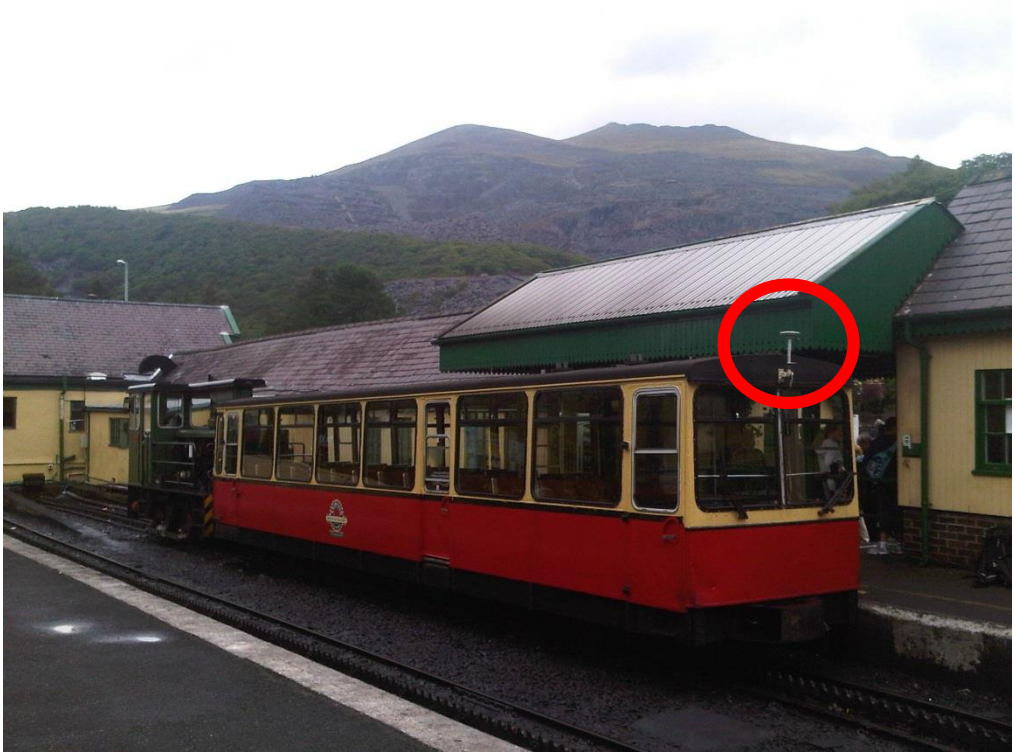

Figure 4-6. GNSS station on a stable platform (SNTR) with Leica AS10 GNSS antenna mounted onto an SMR carriage, shown at the Llanberis terminus (where GNSS station SNLB is also located).

Table 4-1. Distances between GNSS stations SNLB and SNSU and surrounding OS CGNSS stations, and the orthometric heights of the OS CGNSS stations.

| | Distance to SNLB (km) | Distance to SNSU (km) | Height (m) |
|---|---|---|---|
| ASAP | 45.3 | 44.8 | 50 |
| ADAR | 55.4 | 54.4 | 94 |
| HOLY | 41.5 | 46.9 | 13 |
| MACY | 61.4 | 55.5 | 22 |

### 4.1.2. Instrumentation

The GNSS station on a moving platform (SNTR) was a Leica GS10 GNSS receiver with an AS10 antenna mounted on the roof of the carriage. Dual frequency GPS and GLONASS code (C/A code on the L1 band, and P2 code on the L2 band) and phase data was recorded at 10 Hz. A Paroscientific Model 745 pressure unit with a manufacturer stated (Paroscientific, 2009) instrument accuracy of ±0.08 mbar was installed in the carriage, recording pressure measurements every two minutes.

The GNSS stations on stable platforms (SNLB and SNSU) each consisted of a Leica GS10 GNSS receiver with an AS10 antenna, with dual frequency GPS and GLONASS code and phase data recorded at 10 Hz. Paroscientific Met4 pressure and temperature sensors were co-located with the GNSS stations on stable platforms, mounted 0.1 m below the GNSS antenna. Pressure and temperature were logged every five minutes with a manufacturer stated (Paroscientific, 2011) instrument accuracy of ±0.08 mbar and ±0.5 °C respectively. Short data gaps in both GNSS and the meteorology time series occurred when manually downloading the data on day of year (DOY) 241, 253, 268, and 280 for roughly 30 minutes at each site.

#### 4.1.3. Data period

Data was collected over 50 days between 28th August and 16th October 2011 (day of year 240 to 289). Data for the GNSS station on a moving platform (SNTR) was collected between 0600 and 1900 UTC for a total of 87 return trips to the summit (equating to 174 trajectories), and 23 return trips to an altitude of 500 m when the train did not reach the summit (equating to a further 46 trajectories), as the train, and therefore the dataset, was sometimes restricted by weather conditions. For example, if wind speeds exceeded 40 mph then the train's journey was restricted to only go part way up the mountain, or the service was totally stopped with trains not departing from Llanberis terminus at all, as occurred on day of year 255. A logging error also meant that no data was available from SNTR between day of year 271 and 280. Data was collected continually for the GNSS stations on stable platforms (SNLB and SNSU) with an automated restart each day at 22:50 UTC, when the instruments were automatically powered down for 10 minutes to rectify potential logging problems.

### 4.2. Reference coordinates for the GNSS stations on stable platforms

Reference coordinates for the CGNSS stations on stable platforms (SNLB and SNSU) were established for use in relative GNSS positioning, determination of the reference trajectory for the CGNSS station on a moving platform (SNTR) and testing of empirical

tropospheric models, providing a control dataset for the testing of kinematic GNSS positioning solutions, and establishing reference ZTD time series. GPS data from the 50 day experimental window was processed by Dr Nigel Penna using the NASA/JPL GIPSY 6.1.2 scientific software to produce a static PPP solution as sets of daily coordinates. ZTDs were estimated at five minute intervals using established GIPSY processing options (Williams and Penna, 2011) and are described further in section 5.2. OTL displacement were corrected using SPOTL (Agnew, 1997) and FES2004 (Lyard *et al.*, 2006) models, SET were modelled according to the IERS Conventions 2010 (McCarthy and Luzum, 2010), and antenna phase centres modelled following Schmid *et al.* (2007). Ambiguities were fixed according to Bertiger et al (2010). Reprocessed final ESA satellite orbit and clock products were held fixed.

The detrended coordinate time series, in the IGS08 reference frame, for SNLB and SNSU are shown in Figure 4-7. It can be seen that the coordinates vary from day to day by ± 10 mm in plan and ± 20 mm in height with the coordinate time series' standard deviations listed in Table 4-2. The standard deviations suggest that the daily coordinates are of a high quality and that SNLB and SNSU may be used with confidence as known stations for the determination of the reference trajectory of the train by relative GNSS positioning. The multipath effect was assessed by using the 'teqc' software (Estey and Meertens, 1999) to generate daily RMS MP1 and MP2 values for SNLB and SNSU, as can be seen in Figure 4-8. The larger MP1 and MP2 values at SNLB compared to SNSU are consistent with the greater scatter in the coordinate time series experienced at SNLB. The final coordinates were determined as the weighted mean of all daily coordinate estimates obtained for the 50 day period.

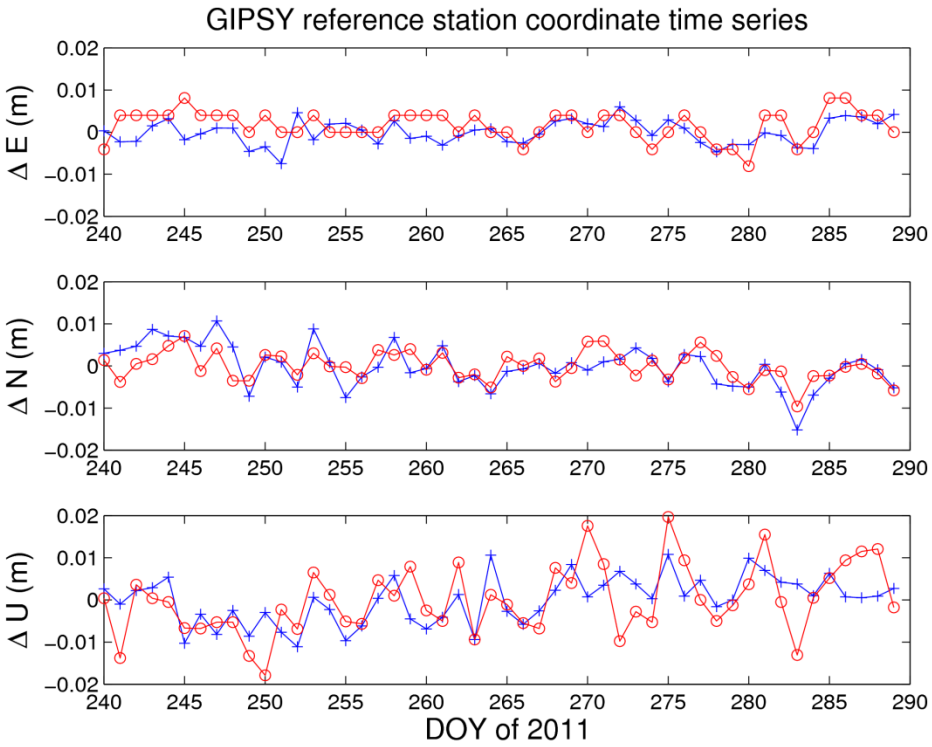


Figure 4-7. Detrended coordinate time series from daily GIPSY PPP coordinate estimates for SNLB (red) and SNSU (blue).

Table 4-2. Day-to-day coordinate repeatability (standard deviations) for the 50 day time series from the GIPSY static PPP solutions for SNLB and SNSU. All quantities are expressed in mm.

| | SNLB | | | SNSU | | |
|---|---|---|---|---|---|---|
| | E | N | U | E | N | U |
| GIPSY | 3.5 | 3.5 | 8.2 | 2.9 | 5.0 | 5.6 |

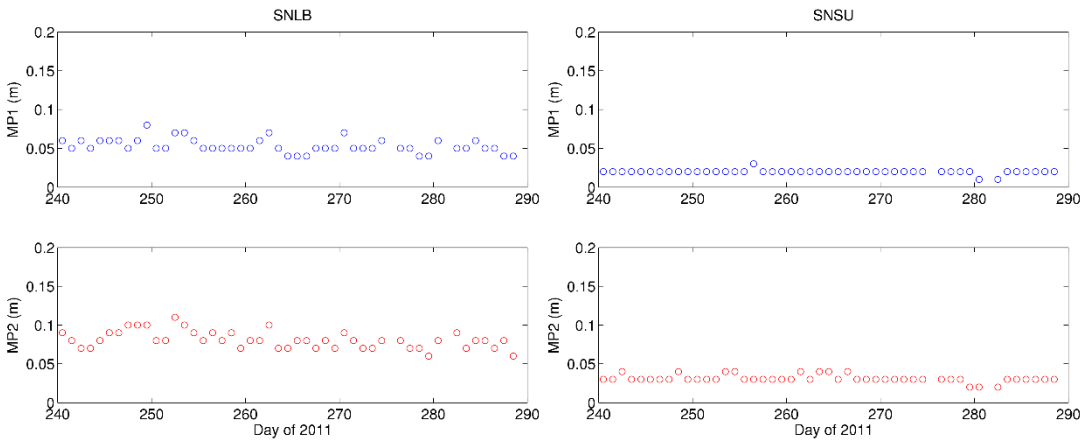


Figure 4-8. Daily MP1 (blue) and MP2 (red) multipath values for SNLB (left) and SNSU (right).

## 4.3. Reference trajectory

A large number of trajectories were collected over the 50 day period as SNTR ascended and descended SMR. A range of atmospheric conditions, satellite numbers, and satellite geometries were experienced at the test site, resulting in a variation in the solution quality at SNTR. By collecting a large sample size and adopting a double-difference positioning solution relative to the known stations at the extremities of the trajectory, the random and systematic errors experienced at SNTR can be mitigated by calculating an average reference trajectory. A minimum distance cubic spline was used to generate a reference trajectory through the multi-baseline relative solutions for the trajectories collected over the 50 day data campaign.

### 4.3.1. Reference trajectory: Relative GPS positioning solutions

Double-difference positioning solutions were computed for the GNSS stations on a moving platform (SNTR) using MIT's GAMIT/GLOBK module Track version 1.24 (Chen, 1998; Herring *et al.*, 2010). Data was processed relative to the established GNSS stations on the stable platforms (SNLB and SNSU), located at the extremities of the railway, at a one second interval. IGS final satellite orbits were held fixed, the tropospheric delay was estimated, using the GMF mapping function (Boehm *et al.*, 2006a) with a cut off elevation angle of 10°. The default value of relative humidity in the GMF was altered from 0 to 0.5, similar to an update available in Track version 1.27. An initial uncertainty of 20 m was set for each coordinate component and a process noise of 4 m $s^{-0.5}$. Track currently does not support GLONASS data, so only the GPS (L1 and L2 carrier phase, and P1 and P2 pseudorange) observables were used. The L1 and L2 carrier phase signals were combined linearly to mitigate 1$^{st}$ order ionospheric effects, and double-difference carrier phase ambiguities were resolved to integer values using a wide-lane linear combination. SNTR was processed relative to both SNLB and SNSU to minimise the baseline length, and to minimise the residual systematic error from variations in altitude.

### 4.3.2. Reference trajectory: Computation

To acquire a reference trajectory a line of best fit was fitted through the coordinates attained from the double-difference positioning solutions relative to both SNLB and SNSU, as detailed in section 4.3.1. A line of fit was required for a data set that was obtained at a varying spatial distribution (dependent on the velocity of SNTR), and at varying points along the trajectory. A line of best fit was obtained by fitting a least squares minimum distance cubic spline through the trajectories collected over the 50 day period.

Before the spline was fitted the data was filtered: points with formal errors greater than 0.5 m were initially removed. Data was also removed when SNTR was moving slower than 0.1 m $s^{-1}$, as if all the trajectory data were included the periods that SNTR was stationary would result in high density of points and could skew the spline. The spline was fitted through the data in a local (topocentric) cartesian coordinate frame, and to allow the spline to be fitted the coordinates of the trajectory had to be a function of monotonically increasing Northing values. Therefore the Northing and Easting coordinate values were rotated by 80 degrees. Due to the gradient of the railway from SNLB to SNSU being positive (carriage wheels are not connected to the engines; they rely on gravity for carriages to roll down the railway and use the engine as a 'bump' brake) for the entirety of the track it is only the plan coordinates that need rotating.

Fitting a spline to form a reference trajectory relies on the assumption that there is a single trajectory being taken. Due to passing places, and embarking and alighting platforms, SNTR can take multiple routes. To overcome this, each path was identified manually and splines were fitted for the corresponding railway sections at the passing places and termini. At the Llanberis termini there is also an alternative railway section used for carriage maintenance and storage, and the runs that experienced these deviations have been excluded from the spline fitting data set. In this respect, the

excluded trajectories were as follows: 243a, 244a, 245a, 248a, 252f, 253b, 254c, 254d, 264a (where letters represent the trajectory of the day).

The cubic spline fitting function '*csaps*' in Matlab 2011b was used to fit a least squares minimum distance cubic spline. The spline is fitted in two dimensional planes in Northing and Easting, and then Northing and height for the same set of points. The spline points are output at the same Northing values for both spline planes. The two planes are then joined together at the corresponding Northing value to provide a spline representing a series of 3D coordinates.

For the sections between the passing places and termini, all the data points that passed the filtering criteria detailed in the previous paragraph were included. At the passing places and termini, splines were formed from the identified trajectories of SNTR. A consequence of splitting the trajectory into sections is that the separation between adjoining spline coordinates is minimised, and the shape of the trajectory sections is less complex (fewer curves). The Matlab spline function only fits a 1000 knots per spline segment, therefore the distance between knots has to be small enough to represent the railway with a linear function between knots to allow the differencing technique outlined in Section 4.3.3 to be used (average distance between spline knots of 0.9 m). The number of points, height range and length of each spline section are displayed in Table 4-3.

Table 4-3. Number of data points, height range, and distance of sections of railway track used to form overall splines for representing the best fit reference trajectory.

| | Number of points | ΔH (m) | Distance (m) |
|---|---|---|---|
| Llanberis L | 6932 | 31.325 | 590.067 |
| Llanberis R | 11437 | 31.486 | 591.487 |
| Llanberis to Hebron | 79467 | 166.046 | 1966.454 |
| Hebron L | 19837 | 64.106 | 644.706 |
| Hebron R | 22518 | 64.113 | 662.057 |
| Hebron to halfway a | 89504 | 140.316 | 1763.724 |
| Hebron to halfway b | 20144 | 40.996 | 361.960 |
| Hebron to halfway c | 29193 | 59.490 | 544.514 |
| Halfway L | 24717 | 86.372 | 839.460 |
| Halfway R | 27289 | 86.385 | 838.736 |
| Halfway to Clogwyn a | 44506 | 95.390 | 811.677 |
| Halfway to Clogwyn b | 17203 | 41.535 | 311.166 |
| Halfway to Clogwyn c | 51756 | 126.286 | 927.465 |
| Clogwyn L | 10562 | 56.774 | 504.125 |
| Clogwyn R | 18157 | 57.308 | 503.429 |
| Clogwyn to Summit a | 49468 | 137.571 | 1096.295 |
| Clogwyn to Summit b | 74678 | 174.149 | 1539.120 |
| Summit L | 5580 | 42.383 | 296.778 |
| Summit R | 12941 | 42.496 | 294.110 |

The spline sections were joined to form a set of continuous splines by splicing them at the midpoint of the overlapping sections between adjoining splines. The locations of the adjoining spline sections are displayed in Figure 4-9, with a schematic representation of the railway and the spline sections displayed in Figure 4-10.

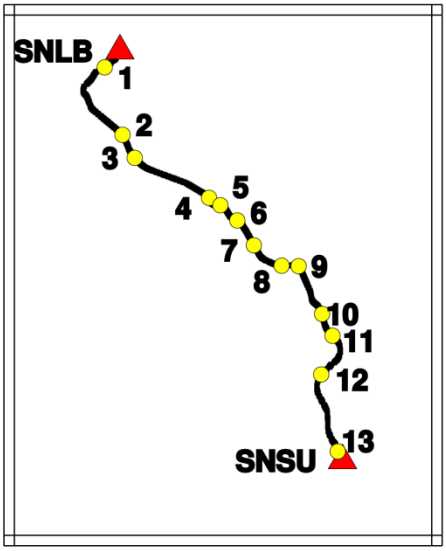


Figure 4-9. Locations of the adjoining spline points (yellow circles) for the reference trajectory.

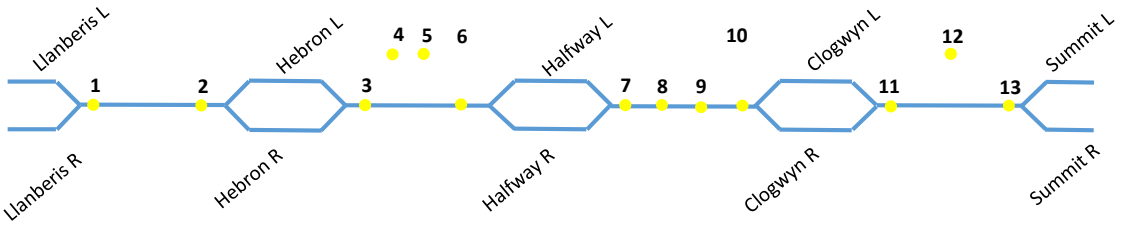


| | |
|---|---|
| 1 – 2 | Llanberis to halfway |
| 3 – 4 | Hebron to halfway a |
| 4 – 5 | Hebron to halfway b |
| 5 – 6 | Hebron to halfway c |
| 7 – 8 | Halfway to Clogwyn a |
| 8 – 9 | Halfway to Clogwyn b |
| 9 – 10 | Halfway to Clogwyn c |
| 11 – 12 | Clogwyn to Summit a |
| 12 – 13 | Clogwyn to Summit b |

Figure 4-10. Schematic plot of the SMR with the spline sections at the passing places and termini labelled and the adjoining points of the splines denoted by yellow circles and numbered to correspond to their location in Figure 4-9. The spline sections between the termini and passing places with respect to the adjoining spline points are listed below the schematic.

There were 32 overall spline combinations in total due to the two termini and three passing places on the railway. An iterative approach was used to smooth the spline from any erroneous points in the data set, with each data point compared to the spline. If the distance to the closest point on the spline is greater than one metre it is deemed an outlier and excluded from the dataset; 6098 points were removed to leave a dataset of 564578. The spline process was then repeated on the filtered dataset. An example of the spline with the collated train positions in the Northing and Easting plane for the entire reference trajectory, and with a zoomed in section, is displayed in Figure 4-11.

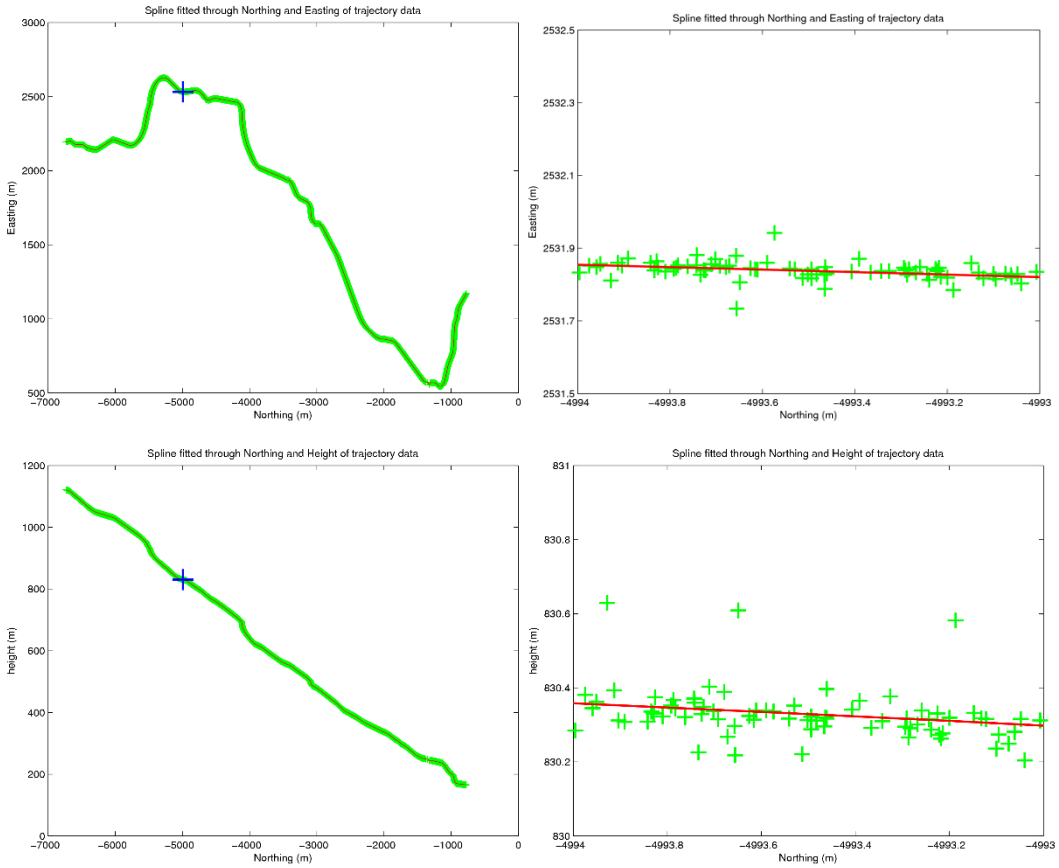


Figure 4-11. Collated discrete SNTR positions (green crosses) from the filtered dataset for the trajectories collected between DOY 240-289, and the fitted spline plotted in a local coordinate system. The entire reference trajectory is displayed on the left pane, and a zoomed in section (identified by the blue cross) on the right pane.

### 4.3.3. Reference trajectory: Goodness of fit

To validate the use of the spline described in section 4.3.2 the GPS-derived coordinates that the spline was fitted through were compared with the resulting reference trajectory. The point on the reference trajectory to compare a GPS point to is defined as the minimum 3D distance, with an example shown in Figure 4-12.

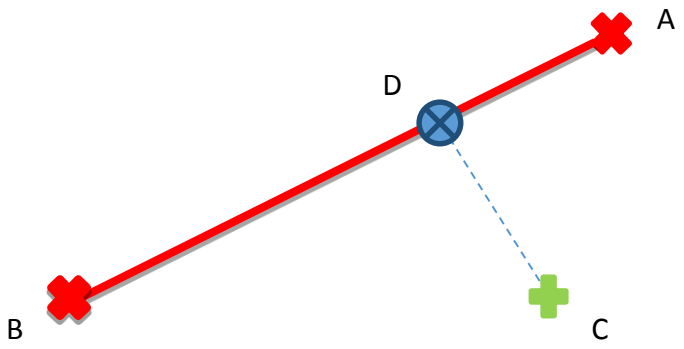


Figure 4-12. Diagram representing the method to determine the shortest distance between GPS-derived position C, and the closest point (D) on the spline.

The method used to compare a GNSS-derived position (point C) to the reference trajectory was as follows:

**I.** Define the nearest spline knot point by minimum distance (point A).

**II.** Select the 2nd closest spline knot point (point B).

**III.** Calculate the point on the spline (point D) between the two identified spline knot points (point A and B) closest to the GPS-derived position (point C).

Therefore the known coordinates of A, B, and C are defined as:

$$A = (x_a, y_a, z_a) \qquad B = (x_b, y_b, z_b) \qquad C = (x_c, y_c, z_c)$$

Where point D can be defined as:

$$D = A + (t * AB) \tag{4-1}$$

and calculated using the geometric relationships outlined below.

The dot product of orthogonal vectors is equal to zero:

$$(B - A) \bullet (D - C) = 0 \tag{4-2}$$

Or

$$AB \bullet CD = 0 \tag{4-3}$$

Substituting equation (4-1) into equation (4-3) leads to:

$$AB \bullet (A + tAB - C) = 0 \tag{4-4}$$

And rearranging equation (4-4) via the following steps:

$$AB \bullet (A - C) + t(AB \bullet AB) = 0 \tag{4-5}$$

$$t(AB \bullet AB) = -AB \bullet (A - C) \tag{4-6}$$

$$t = (AB \bullet AC)/(AB \bullet AB) \tag{4-7}$$

Leads to the coordinates of D being calculated by:

$$D = A + \{AB \bullet AC/AB \bullet AB\} * AB \tag{4-8}$$

Where • denotes the dot product.

**IV.** Calculate the difference between the GNSS-derived position (point C) and the interpolated spline point (point D).

$$CD = D - C \tag{4-9}$$

To test the assumption that the trajectory can be represented by a straight line between the spline knots, the difference in height and plan for each spline knot was computed as a straight line fitted between the adjoining spline knots. The RMS, median, 5th and 95th centiles of the differences in height are given in Table 4-4 and the differences displayed against the spline height in Figure 4-13. The majority of the points are within 2 mm of the straight line in height and in plan, with RMS values of 0.9 mm and 0.4 mm respectively. The assumption that a straight line can represent the trajectory between spline knots is based on the noise of kinematic GNSS positioning being at least an order of magnitude greater than the differences from the straight line.

Table 4-4. RMS, median, 5th centile, and 95th centile of the differences in height and in plan between spline knots and the straight line linking the adjoining spline knots. All quantities are expressed in mm

| | RMS | Median | 5th centile | 95th centile |
|---|---|---|---|---|
| Height | 0.9 | 0.0 | -1.4 | 1.4 |
| Plan | 0.4 | 0.1 | 0.2 | 0.6 |

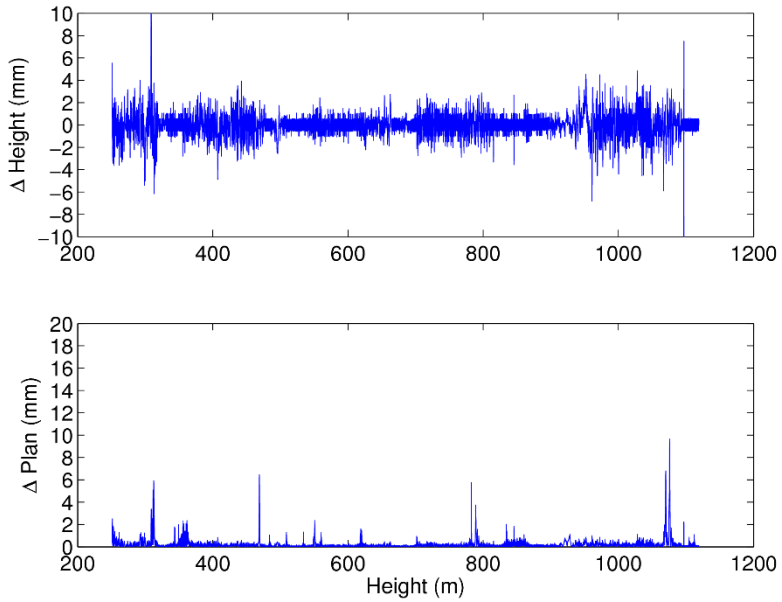


Figure 4-13. Difference in height (top panel) and plan (lower panel) for spline knots compared to the closest point to the linear fit between the adjoining spline knots.

The dataset that the spline was fitted through could then be compared to the spline. The RMS, standard deviation, and median differences along with the interquartile range of the 3D minimum distances of each spline section are displayed in Table 4-5. The higher RMS and median difference values at Llanberis and between Llanberis and Hebron sections, is a result of the railway track in these sections having poorer satellite coverage and more multipath due to tree coverage and the proximity of buildings and equipment to the railway track. Excluding the sections Llanberis (L and R) and Llanberis to Hebron, the median and standard deviation of the minimum 3D distance to the spline ranges between 0.032 m and 0.041 m, and 0.083 m and 0.117 m respectively. Error bars of the Easting and height differences for each section are displayed in Figure 4-14. The greater range between the $5^{th}$ and $95^{th}$ centile for the height component compared to Easting is expected due to the high accuracy of GNSS positioning in plan compared to height. Due to the large number of reference trajectories collected during a range of atmospheric conditions and satellite geometry configurations, random errors from the GPS solutions should be averaged to give a single reference trajectory for later analysis.

Table 4-5. RMS, standard deviation, median, 5th centile, and 95th centile of the minimum 3D distance (in metres) between GPS-derived positions and the reference trajectory.

| | RMS | STD | Median | 5th centile | 95th centile |
|---|---|---|---|---|---|
| Llanberis L | 0.465 | 0.288 | 0.261 | 0.047 | 0.898 |
| Llanberis R | 0.454 | 0.325 | 0.186 | 0.021 | 0.947 |
| Llanberis to Hebron | 0.323 | 0.260 | 0.066 | 0.010 | 0.764 |
| Hebron L | 0.114 | 0.097 | 0.033 | 0.009 | 0.185 |
| Hebron R | 0.103 | 0.085 | 0.032 | 0.007 | 0.225 |
| Hebron to halfway a | 0.105 | 0.088 | 0.032 | 0.008 | 0.192 |
| Hebron to halfway b | 0.115 | 0.097 | 0.035 | 0.008 | 0.185 |
| Hebron to halfway c | 0.114 | 0.095 | 0.035 | 0.008 | 0.226 |
| Halfway L | 0.122 | 0.103 | 0.037 | 0.009 | 0.287 |
| Halfway R | 0.102 | 0.084 | 0.033 | 0.008 | 0.207 |
| Halfway to Clogwyn a | 0.111 | 0.094 | 0.034 | 0.008 | 0.223 |
| Halfway to Clogwyn b | 0.123 | 0.106 | 0.036 | 0.009 | 0.217 |
| Halfway to Clogwyn c | 0.117 | 0.100 | 0.033 | 0.008 | 0.245 |
| Clogwyn L | 0.123 | 0.108 | 0.032 | 0.008 | 0.161 |
| Clogwyn R | 0.114 | 0.095 | 0.034 | 0.008 | 0.280 |
| Clogwyn to Summit a | 0.129 | 0.110 | 0.036 | 0.009 | 0.252 |
| Clogwyn to Summit b | 0.123 | 0.105 | 0.036 | 0.009 | 0.241 |
| Summit L | 0.135 | 0.117 | 0.032 | 0.008 | 0.380 |
| Summit R | 0.106 | 0.083 | 0.041 | 0.009 | 0.177 |

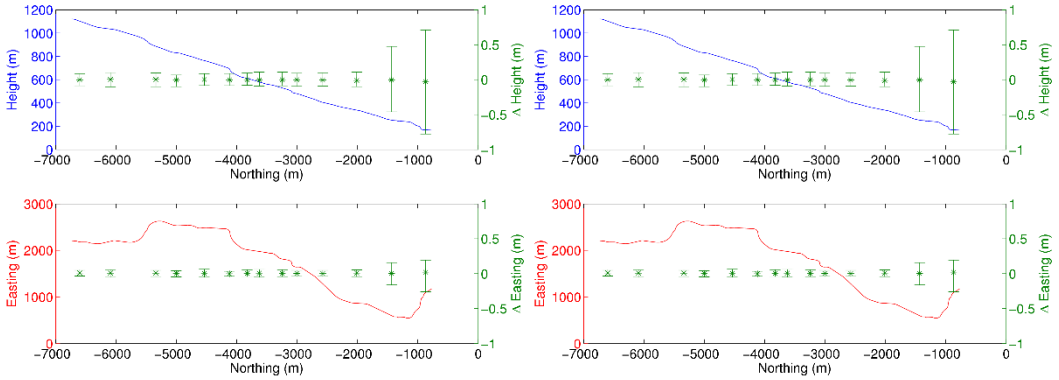


Figure 4-14. Height (top pane, blue line) and Easting (lower pane, red line) of the SMR, with median error bars of the height and plan differences for the spline section between GPS-derived positions and the reference trajectory on the right-hand scales. Tails of the error bars define the 5$^{th}$ and 95$^{th}$ centile. Spline sections fitted to the left-hand passing places (when travelling uphill) are included on the left panes and passing places to the right (when travelling uphill) on the right panes.

## 4.4. Summary

A suitable moving platform was identified and utilised to obtain a unique dataset to assess the mitigation and sensing of tropospheric delay from kinematic GNSS positioning over a range of altitudes. The collected 50 day dataset included over 200 trajectories through the lower atmosphere, providing a suitable dataset for a reference trajectory to be established from, a large sample size of trajectories and profiles to be assessed, and a range of atmospheric conditions to be experienced. The location of SMR also meant reference tropospheric delay values could be established at the maximum and minimum heights of the atmospheric profile.

Absolute GNSS positioning was employed to provide high accuracy GPS-derived coordinates and reference tropospheric delay values (that will be described in further detail in Chapter 5) for the GNSS stations on stable platforms (SNLB and SNSU). Relative GNSS positioning was then used with reference to the two GNSS stations on stable platforms situated at the extremities of the trajectory of the GNSS station on a moving platform (SNTR), with the average GPS-derived position computed from the resulting trajectories and a spline used to provide a single reference trajectory. The reference trajectory will be used to assess tropospheric mitigation in GNSS and is covered in Chapter 8.

# 5. Tropospheric comparators

Reference tropospheric delay values are required for the GNSS station on the moving platform (SNTR) in order to compare and assess the quality of empirically modelled or estimated delay values. The use of static GNSS positioning to estimate ZTD is an established technique for validating the retrieval of ZTD (or ZWD) from alternative sensors (e.g. Deeter (2007)), or from numerical weather models (NWM) (e.g. Chen *et al.* (2011)). Reference tropospheric delay time series were established at the extremity of the trajectory for the GNSS stations on stable platforms (SNLB and SNSU), allowing kinematic GNSS solutions to be tested at the CGNSS stations on stable platforms (SNLB and SNSU), and allowing reference tropospheric delay values to be interpolated for the GNSS station on a moving platform (SNTR). The SMR dataset provided an opportunity for an accurate reference of tropospheric delay over a ~1 km altitude range to be established during a variety of meteorological conditions. The use of a comprehensive reference dataset allowed a rigorous assessment of the retrieval of ZWD from kinematic GNSS positioning on a moving platform over a varying altitude. This chapter describes the tropospheric comparators used on the SMR data set, including the generation of zenith tropospheric delays at the GNSS stations on stable platforms (SNLB and SNSU), extrapolation of pressure observations, interpolated ZWD values for the GNSS station on a moving platform (SNTR), and NWM derived delay values. The GIPSY-derived ZTD, interpolated reference ZWD, and NWM tropospheric comparators described in this chapter are taken from Webb *et al.* (2014).

## 5.1. Pressure observations and extrapolation for ZHDs at SNLB and SNSU

To obtain ZWD from a GNSS solution the delay from the stable hydrostatic elements of the atmosphere, the ZHD, is subtracted from ZTD. ZHD is calculated from atmospheric pressure. If pressure is not available at a GPS site then a pressure value will either have to be obtained by extrapolation, from a NWM, or from empirical models with standardised mean values. The change in pressure and temperature with

height can vary depending on atmospheric conditions. Pressure and temperature differences between SNLB and SNSU are displayed in Figure 5-1. The variation in the lapse rates of temperature and pressure limits the effectiveness of mitigation from extrapolation techniques that use a standardised modelled rate.

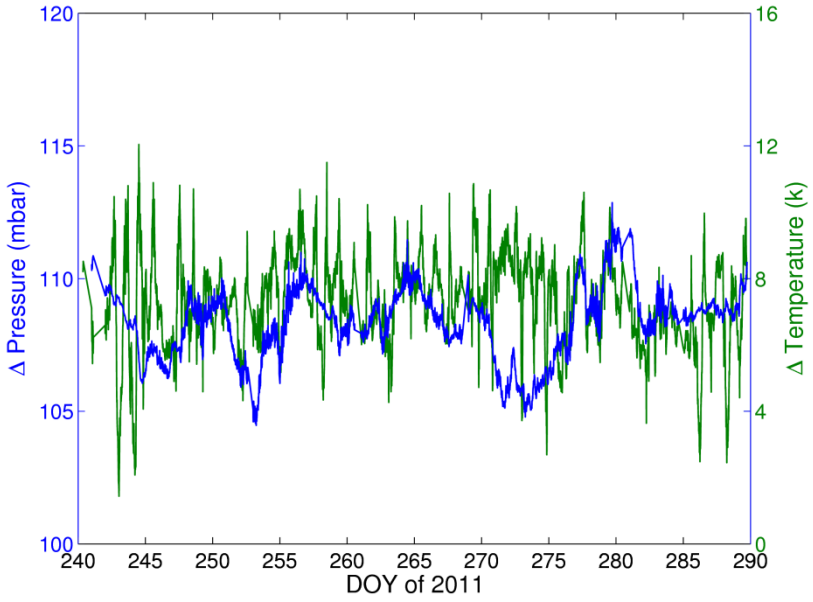


Figure 5-1. Difference in pressure (blue) and temperature (green) between reference sites SNLB and SNSU.

The error that could be introduced into a ZWD measurement if in-situ pressure is not recorded will be examined. Three extrapolation methods referred to herein as Berg (listed in Berg (1948) and used in Boehm *et al.* (2007) and Kouba (2008)), Hopfield(1971), and the Hydrostatic equation (HQ) (Wallace and Hobbs, 1977) are tested. The models are outlined in equations (5-1) to (5-7).

*Berg:*

$$P_{sl} = \frac{P_{ref}}{(1 - 0.0000226H_{ref})^{5.225}} \tag{5-1}$$

$$P_{extr} = P_{sl}(1 - 0.0000226H_{extr})^{5.225} \tag{5-2}$$

*Hopfield:*

$$P_{sl} = {P_{ref}} \Big/ {\left(\frac{T_{sl} - \propto H_{ref}}{T_{sl}}\right)^{(g/R\propto)}} \tag{5-3}$$

$$T_{sl} = T_{ref} + \propto H_{ref} \tag{5-4}$$

$$P_{extr} = P_{sl}\left(\frac{T_{sl} - \propto H_{extr}}{T_{sl}}\right)^{(g/R\propto)} \tag{5-5}$$

*Hydrostatic equation* (HQ):

$$P_{extr} = P_{ref} exp(-g(H_{extr} - H_{ref})/RT_0) \tag{5-6}$$

$$T_0 = mean(T_{ref}) + \propto ((H_{ref} - H_{extr})/2) \tag{5-7}$$

Where:

| | | |
|---|---|---|
| $P_{extr}$ | = | Extrapolated Pressure (mbar) |
| $P_{sl}$ | = | Pressure at sea level (mbar) |
| $P_{ref}$ | = | Pressure at reference station (mbar) |
| $T_{sl}$ | = | Temperature at sea level (K) |
| $T_{ref}$ | = | Temperature at reference station (K) |
| $T_0$ | = | Average temperature (K) |
| $H_{ref}$ | = | Height of reference station (km) |
| $H_{extr}$ | = | Extrapolation height (km) |
| $\propto$ | = | Temperature lapse rate ($\propto$ = 7 K km$^{-1}$) |
| $R$ | = | Dry air gas constant (R = 0.287 J kg$^{-1}$ K$^{-1}$) |
| $g$ | = | Acceleration due to gravity (g = 9.81 m s$^{-2}$) |

The extrapolated ZHD values were tested between the two GNSS stations on stable platforms (SNLB and SNSU). Due to the stations being located at the extremities of the test area the differences between the extrapolated pressure based ZHD and the reference ZHD will be a maximum for the test site. Truth ZHD values for SNLB and SNSU were calculated using equation (5-8), utilising in-situ pressure measurements at each site recording at a five minute interval.

$$zhd = 0.0022768 \frac{\mathrm{P}}{(1 - 0.00266\cos(2\varphi) - 0.28 \times 10^{-6})} \quad (5\text{-}8)$$

The differences between ZHD derived from in situ pressure measurements at SNSU and the three pressure extrapolation methods are displayed in Figure 5-2, with the RMS, standard deviation, median, maximum differences and minimum difference displayed in Table 5-1. The Hopfield derived ZHD performs noticeably better between day of year 270 to 275 compared to that using HQ and Berg. It can be seen from Figure 5-1 that the difference in pressure does not match the trend of the difference in temperature between day of year 270 to 275 as it does for the majority of the rest of the time series. The improved performance of Hopfield over these five days could be attributed to the use of actual temperature values, rather than using a nominal temperature as used in the Berg and HQ methods.

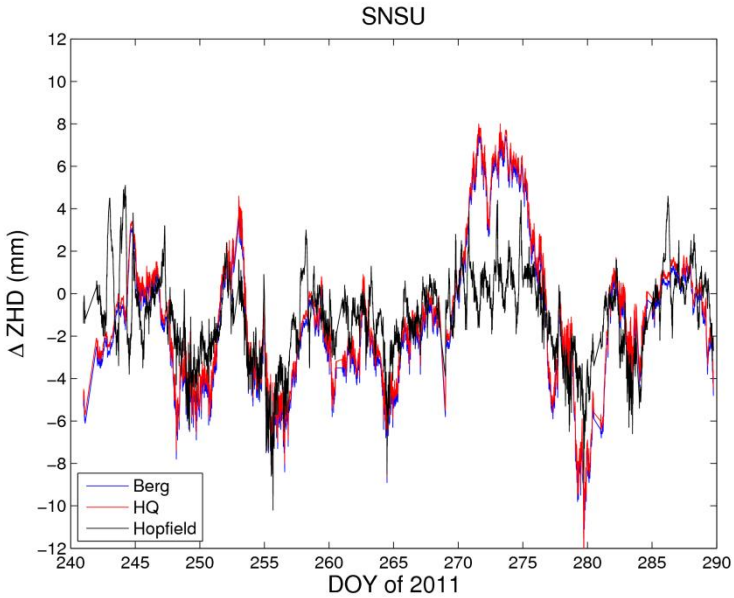


Figure 5-2. Differences between derived ZHD at SNSU from in situ pressure, and extrapolated pressure from SNLB using the Berg (blue), HQ (red), and Hopfield (black) models.

Table 5-1. RMS, standard deviation, median, maximum value, and minimum value of ZHD differences at SNSU between ZHD values derived from extrapolated pressure values from SNLB, and ZHD derived from in-situ pressure measurements at SNSU. All quantities are expressed in mm.

| | SNSU | | | | |
|---|---|---|---|---|---|
| | RMS | STD | Median | Max | Min |
| Berg | 3.6 | 3.4 | -1.6 | 7.6 | -12.9 |
| HQ | 3.5 | 3.4 | -1.2 | 8.0 | -12.5 |
| Hopfield | 2.3 | 2.0 | -1.0 | 5.1 | -10.2 |

Over the 50 day test period the error from misrepresenting the change in pressure with altitude was shown to lead to an error of up to 13 mm from using extrapolation techniques over an altitude range of ~1 km. The RMS and median ZHD differences of 2.3 mm to 3.6 mm, and -1.0 mm to -1.6 mm respectively, suggest that the overall trend of the derived ZHD from pressure and temperature extrapolation can be modelled. However, for applications with short periods of data collection that require ZHD mitigation, such as airborne GNSS positioning, the errors in ZHD cannot be assumed to average out over a period of time. Therefore it is recommended that for meteorological airborne GNSS positioning, in situ pressure measurements rather than extrapolated pressure from ground-based sensors should be used.

## 5.2. GIPSY estimated ZTDs and ZWDs at SNLB and SNSU

Reference ZTDs were established at SNLB and SNSU using the NASA/JPL PPP software GIPSY 6.1.2 using the processing options outlined in Section 3.3. ZTD estimates were computed at five minute intervals, and averaged in 15-minute windows (within the minimum frequency recommended by the World Meteorological Organization (Haan and Jones, 2013)), for the daily processing runs. ZWDs were established from the estimated ZTD by subtracting ZHD calculated from co-located pressure measurements as described in section 5.1. The ZWD values for SNLB and SNSU, as well as the differences between these sites can be seen in Figure 5-3. The mean ZWD differences

between SNLB and SNSU of 52.8 mm highlights the large proportion of the water vapour in the atmosphere being profiled.

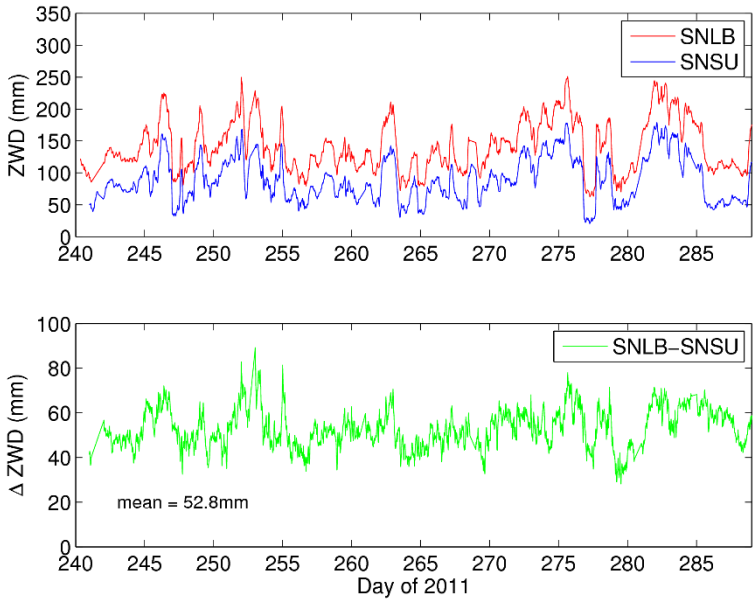


Figure 5-3. GIPSY-generated reference ZWDs for SNLB and SNSU (upper pane), and the differences between them (lower pane).

## 5.3. Interpolated ZWDs at SNTR

A comparator ZWD acting as a reference for SNTR was obtained by interpolating the GIPSY-estimated ZWDs from SNLB and SNSU. At each epoch an empirical decay coefficient (EDC) was computed (equation (5-9), following Kouba (2008)), inputting the known heights and ZWD estimates from SNLB and SNSU. The SNTR ZWD was then computed using equation (5-10).

$$EDC(t) = -\left(h_{SNSU} - h_{SNLB}\right) / \ln\left(zwd_{SNSU}(t) / zwd_{SNLB}(t)\right) \tag{5-9}$$

$$zwd_{SNTR}(t) = zwd_{SNLB}(t) \cdot e^{\left(h_{SNTR}(t) - h_{SNLB}\right)/EDC(t)} \tag{5-10}$$

To validate this approach, ZWD values were extrapolated from SNLB to SNSU and from SNSU to SNLB respectively with a fixed EDC of 2000 m, as established in Kouba (2008), and each was compared with the GIPSY-estimated reference ZWD values. The

differences between the extrapolated and GIPSY reference ZWD values for SNLB and SNSU for a 5 day subset of the data set are shown in Figure 5-4. For the whole dataset, the RMS and median of the differences are 17.8 mm and -0.5 mm respectively for SNLB, and 11.0 mm and -0.3 mm for SNSU. Because these statistics are for extrapolated ZWD over the full altitude range of the railway, they provide very conservative upper bounds on the quality of the SNTR reference ZWD values derived using equation (5-10), since the latter are interpolated and there is usually a much smaller altitude difference from SNLB or SNSU. The actual quality of the SNTR reference ZWD is inferred to be sub-centimetre (RMS), with negligible bias, based on calculation of a variable EDC.

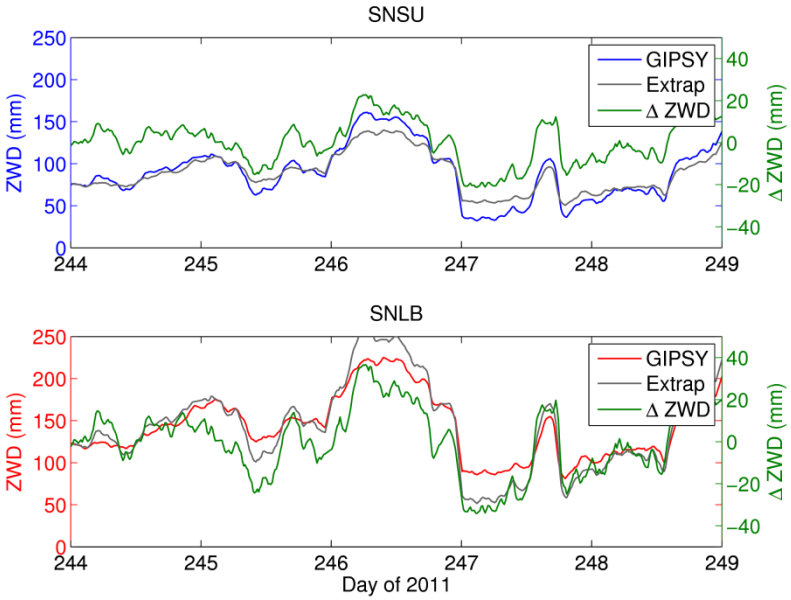


Figure 5-4. Reference ZWD for DOY 244 - 248 estimated using GIPSY for SNSU (upper pane, blue line) and SNLB (lower pane, red line), and ZWD extrapolated to each site from the other (grey lines). The difference between the estimated and extrapolated values is also shown (green lines, right-hand scale).

## 5.4. NWM estimated ZTDs, ZHDs, and ZWDs at SNLB, SNSU, and SNTR

A tropospheric dataset independent from the installed instruments at SMR was sought to provide further confidence in the reliability of reference and GNSS estimates of tropospheric delay. The UK Met Office Unified Model was used to provide ZTD and ZHD (therefore allowing ZWD to be deduced). The Unified Model is a suitable

comparator with its ability to operate at a spatial resolution of 100 m. Due to the steep topography of the SMR test site a NWM model that uses a high spatial resolution terrain model is paramount for representing atmospheric conditions such as pressure and water vapour content. The description in this section of the Unified Model was provided by Gemma Bennitt and Dr Stuart Webster, collaborators on this project at the UK Met Office.

The Met Office Unified Model solves the non-hydrostatic, deep-atmosphere equations of motion on a rotated latitude–longitude grid using a semi-implicit, semi-Lagrangian numerical scheme (Davies *et al.*, 2005). It uses Arakawa C-grid staggering in the horizontal and a terrain-following hybrid-height Charney–Phillips vertical grid. A comprehensive set of physical parameterisations is used, including surface (Best *et al.*, 2011), boundary-layer (Lock *et al.*, 2000) and mixed-phase cloud microphysics (Wilson and Ballard, 1999).

The configuration used in this study consists of a set of one-way nested domains with horizontal grid lengths of 4 km, 1 km, 333 m and 100 m. The 4 km resolution domain is the Met Office UK4 model, which covers the whole of the UK and includes a full data assimilation system and hence generates operational analyses every 3 hours. The 1 km domain is based on the Met Office operational UK 1.5 km model (the UKV) but uses a smaller domain covering only a 100 km × 100 km domain centred on Snowdon. The 1 km model uses the standard boundary-layer scheme for vertical sub-grid mixing but, unlike the UK4 configuration, uses a stability-dependent Smagorinsky–Lilly diffusion scheme in the horizontal. The 333 m and 100 m models cover 50 km × 50 km and 20 km × 20 km respectively and both use the Smagorinsky–Lilly diffusion scheme in the vertical as well as in the horizontal, since at these microscale resolutions the three-dimensional nature of the boundary layer eddies may be partially resolved. All the models use 70 levels in the vertical, the spacing of which increases quadratically with height up to the domain top at 40 km. The majority of the levels are located near the surface, with five levels in the lowest 100 m and 16 levels in the lowest 1 km of the atmosphere.

The nested model set was run as a 'dynamical adaptation' of the UK4 model, keeping the simulation as close as possible to the operational analysis. The 4 km model was re-run from the operational analysis every 3 hours, to provide the lateral boundary condition (LBC) data for the 1 km model, which provided LBC data for the 333 m model which in turn provided LBC data for the 100 m model. The 1 km, 333 m and 100 m models were all initialised with the interpolated 4 km analysis, but were then free-running, such that no further re-initialisation took place. Hereafter, NWM refers to the data output by the 100 m model.

Using model fields of pressure, temperature and humidity, the wet and dry refractivity was calculated for each model grid point. The total refractivity was then used to find the contribution to the satellite signal delay for each model layer, at each grid point. To obtain the ZTD for each surface grid point, the vertical total of all the layer delays above that point were found, and then added the contribution to the delay of the atmosphere above the model top, as detailed in Bennitt and Jupp (2012). To calculate the ZWD, the dry refractivity when calculating the refractivity at each grid point was omitted, before using this value to calculate the contribution of a layer of atmosphere to the total ZTD, assuming the atmospheric refractivity decays exponentially with height from the surface. ZHD was then calculated as the difference between the ZTD and ZWD.

Atmospheric simulations of tropospheric delay were conducted for the 50 day study period, with outputs generated every 15 minutes for the GNSS stations on stable platforms (SNLB and SNSU), and at every 25 m of vertical height change of the trajectory for the GNSS station on a moving platform (SNTR). The NWM ZHD and ZWD values were corrected for the difference between the topographic height of the model (the 90 m horizontal resolution SRTM-3 digital terrain model used in the NWM) and the actual terrain height by the extrapolation methods outlined in Kouba (2008). The NWM ZHD and ZWD outputs were linearly interpolated to the location of SNTR from the bounding NWM time series to correct for differences in height and epoch of output.

The generated ZHD and ZTD values were validated at the GNSS stations on stable platforms (SNLB and SNSU) using the reference ZTD obtained from GIPSY (see section 5.2) and in-situ pressure derived ZHD values. The NWM and reference ZTD and ZHD for the 50 day data period and the differences between the time series are displayed in Figure 5-5 and Figure 5-6, with the differences summarised in Table 5-2.

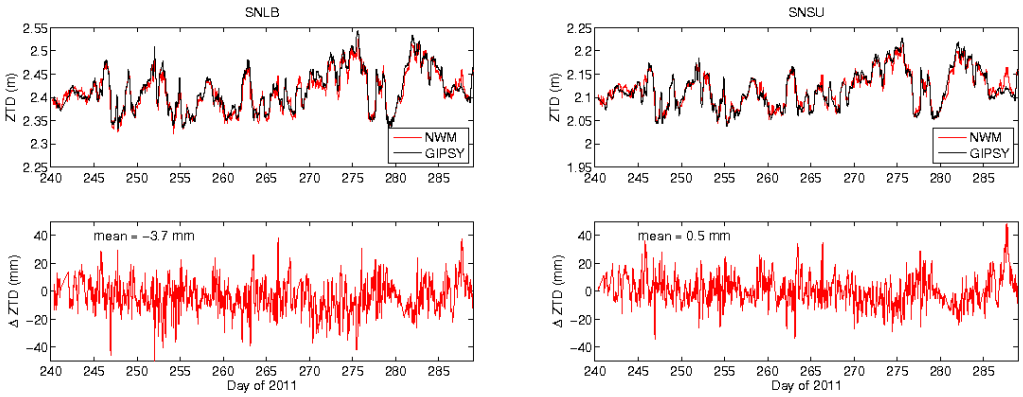


Figure 5-5. Reference ZTD time series obtained from GIPSY (reference, black), and ZTD time series from the Unified Model (red), for SNLB and SNSU on DOY 240-289 of 2011 (upper panes). Lower panes show the differences between the Unified Model estimation and the reference ZTD values.

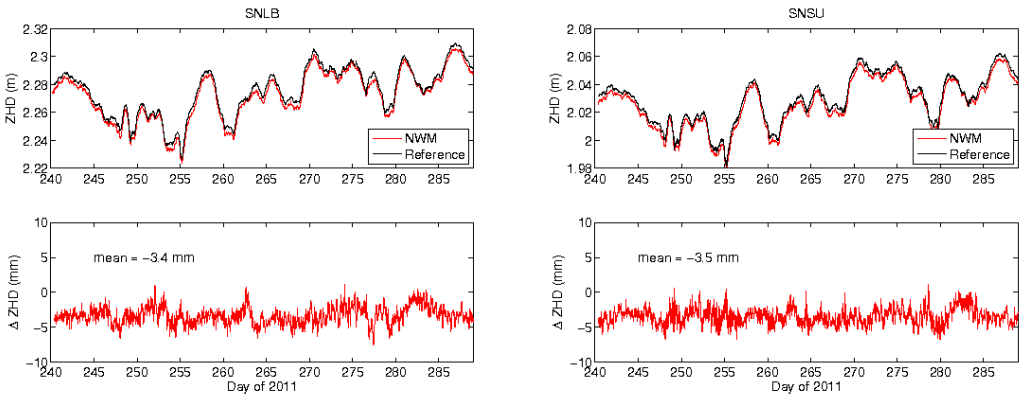


Figure 5-6. Reference ZHD time series obtained from in-situ pressure measurements (reference, black), and ZHD time series from the Unified Model (red), for SNLB and SNSU on DOY 240-289 of 2011 (upper panes). Lower panes show the differences between the Unified Model estimation and the reference ZHD values.

Table 5-2. RMS, standard deviation and median of the differences between ZTD and ZHD estimates from the Unified Model and reference ZTD and ZHD values at SNLB and SNSU. All quantities are expressed in mm.

| | SNLB | | | SNSU | | |
|---|---|---|---|---|---|---|
| | RMS | STD | Median | RMS | STD | Median |
| Unified Model ZTD | 11.7 | 11.1 | -4.0 | 10.4 | 10.4 | -0.3 |
| Unified Model ZHD | 3.6 | 1.2 | -3.4 | 3.7 | 1.1 | -3.5 |

The larger-than-average difference in ZTD between the NWM estimates and the reference values around day of year 287 was investigated. For both SNLB and SNSU an increase in the difference can be seen, with the magnitude of the bias larger at SNSU. The magnitude of the ZHD bias does not increase over day of year 287, suggesting that it is the ZWD that is being misrepresented in the model.

From examining the model the high ZTD during day of year 287 appears to result from an erroneously thick near surface moist layer. The model appears to represent the temperature inversion of the 1 - 2 km layer reasonably well, but not the humidity field. The erroneously moist layer of 2 - 5 km, as shown in Figure 5-7, would appear to account for the larger difference in ZTD values for day of year 287.

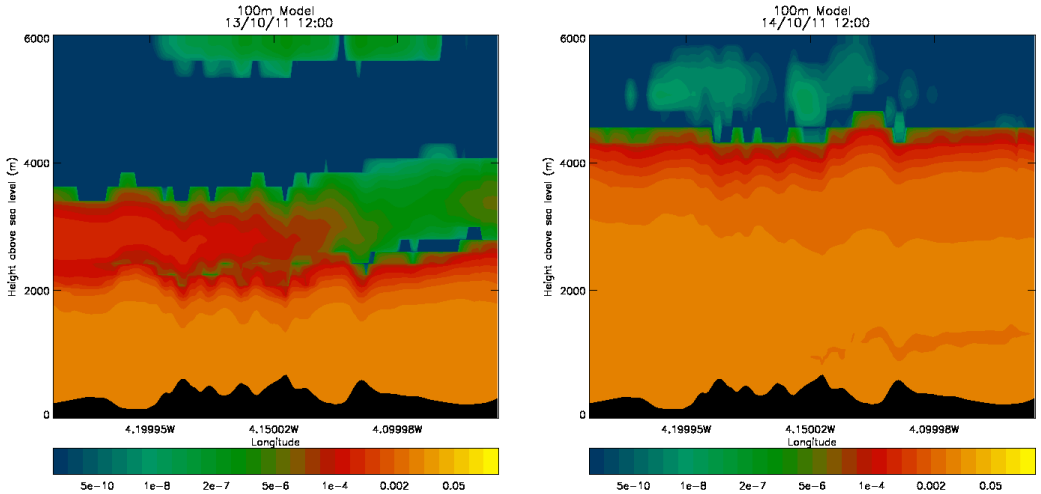


Figure 5-7. Cross section of relative humidity from the NWM Unified Model, running east to west along the Snowdon test site, with DOY 286 on the left and DOY 287 on the right (generated by Dr Stuart Webster at the Met Office).

The representation of ZTD at SNLB and SNSU for the 50 day test period with RMS of 11.7 mm and 10.4 mm respectively (Table 5-2), and ZHD represented with medians of -3.4 mm and -3.5 mm (Table 5-2), shows that the NWM dataset is a suitable independent quality control dataset for the assessment of tropospheric zenith delays from kinematic GNSS positions for the GNSS station on a moving platform (SNTR).

## 5.5. Summary

This chapter has presented the tropospheric comparators used for the SMR dataset. The decrease in ZWD with an increase in altitude has been demonstrated, with a mean ZWD difference of 50 mm between SNLB and SNSU. The variability in the ZWD lapse rate is also evident with the ZWD difference between SNLB and SNSU varying about the mean by up to 40 mm. Reference ZWD were established for the GNSS station on a moving platform (SNTR) from interpolation between the GNSS stations on stable platforms (SNLB and SNSU), with the potential error considered to be at the sub-centimetre level. The importance of measuring co-located pressure to derive accurate ZHD was highlighted, with the potential to introduce centimetre level error into ZWD estimates if extrapolating ZHD from ground-based pressure measurements.

The use of a NWM as an independent tropospheric delay comparator provides confidence in the observations collected at the two GNSS stations on stable platforms (SNLB and SNSU), with ZHD standard deviation agreement of up to 1.2 mm and a median bias of up to -3.5 mm, and ZTD standard deviation of up to 11.1 mm and a median bias of up to -4.0 mm. The performance of the NWM delay time series at the site extremities provides confidence in the NWM as an additional comparator for SNTR.

# 6. Benchmarking the ability of empirical tropospheric models to predict tropospheric delay at a range of altitudes

Empirical tropospheric models are widely used in kinematic GNSS relative positioning to try to mitigate the residual delay from the differenced solution. Tropospheric models attempt to represent an average atmosphere, and therefore cannot characterise the high temporal and spatial variations in the atmosphere. Previous studies (e.g. Shan *et al*. (2007); King (2009)) have shown height differences of 0.1 - 0.3 m can result in airborne GNSS positioning from modelling the tropospheric delay and not estimating it. This chapter will investigate the effectiveness of empirical tropospheric models at SMR by comparing to pressure and temperature observations, and to GNSS derived reference ZTD values at a range of altitudes. The effect of tropospheric modelling on the accuracy of kinematic GNSS positioning will also be further assessed in Chapter 8.

## 6.1. Empirical tropospheric models

A range of empirical tropospheric models are incorporated in many GNSS processing packages as outlined in this section. The models can vary from using global yearly nominal values for temperature, pressure and relative humidity, to latitudinal and temporal dependent sampling of the predicted values.

### 6.1.1. Saastamoinen

The Saastamoinen tropospheric model (Saastamoinen, 1972) calculates ZTD by the sum of the ZWD and ZHD, and can be outlined as:

$$ZWD = 0.0022768 \frac{1255\ \mathrm{e}}{((\mathrm{T} + 273) + 5 \times 10^{-2})\ \mathrm{g}} \tag{6-1}$$

$$ZHD = 0.0022768\ \frac{\mathrm{P}}{\mathrm{g}} \tag{6-2}$$

Where g is the local gravity acceleration at the station height:

$$\mathrm{g} = 1 - 0.00266 * \cos(2\varphi) - 0.00028\ H \tag{6-3}$$

Due to the model not relying on input from meteorological measurements, standard atmospheric equations and nominal values are used to predict pressure, temperature and water vapour pressure. The mean sea level pressure, temperature and relative humidity values, and the methods to reduce values with altitude are displayed in equations (6-4) to (6-6).

Pressure is calculated at a station's orthometric height using Berg (1948)'s approximation:

$$P = P_0 * (1 - 0.0000226 * H)^{5.26} \tag{6-4}$$

$$P_0 = 1013.25\ mbar$$

Temperature is obtained from

$$T = T_0 - 0.0065 * H \tag{6-5}$$

$$T_0 = 18^{\circ}\mathrm{C}$$

And the relative humidity ($rh_0$) and partial water vapour pressure (e) are given by

$$rh_0 = 50\%$$

$$\mathrm{e} = 6.11 * (\frac{T + 273}{273})^{-5.3} * exp^{(\frac{273}{T+273})25.2} * rh_0 \quad (6\text{-}6)$$

### 6.1.2. Saastamoinen with GPT input

The global pressure and temperature (GPT) model (Boehm *et al.*, 2007) is based on three years (Sept 1999 to Aug 2002) of a 15° × 15° global grid of monthly mean pressure and temperature profiles from the ECMWF (European Centre for Medium-Range Weather Forecasts) 40 year reanalysis data (ERA40). Pressure and temperature values and their associated annual amplitudes at each grid point are expanded into spherical harmonics up to degree and order nine. Annual variations for pressure and temperature are fitted as a cosine, with the zero phase defined at 28$^{th}$ January. The model exponentially interpolates pressure and linearly scales temperature from the Earth's surface to the required height. The temperature lapse rate is the same as used in the Saastamoinen model (equation (6-5)), while the pressure lapse rate is described by:

$$P = P_0 * (1 - \ 0.0000226 * H)^{5.225} \quad (6\text{-}7)$$

The GPT model accepts ellipsoidal rather than orthometric heights due to orthometric heights often not being available in GNSS processing. Ellipsoidal heights were transformed to orthometric heights in the model by expanding geoid-ellipsoid separations from the EGM96 model into spherical harmonics up to degree and order nine. Pressure and temperature estimates from the GPT model are then input into the Saastamoinen model to calculate ZHD and ZWD.

### 6.1.3. Saastamoinen with GPT2 input

GPT2 (Lagler *et al.*, 2013) is an updated version of GPT. Updates include higher spatial sampling, modelled rather than assumed temperature lapse rates, semi-annual (in addition to annual) temporal variations fitted, and the inclusion of modelled water vapour pressure. Mean monthly temperature, pressure and temperature lapse rate profiles from the ECMWF reanalysis ERA-interim dataset were sampled over a nine year period (2001 - 2010) on a 5° global grid. Annual and semi-annual variations in the atmosphere are fitted with a least squares adjustment at each grid point for each parameter. The reduction of pressure with altitude is calculated by using the virtual temperature and based on the assumption that a parcel of dry air will have the same pressure and density as a parcel of wet air.

$T_v$ is the virtual temperature and can be derived by using

$$T_v = T_0(1 + 0.6077 * Q) \tag{6-8}$$

and Q is the specific humidity (ratio of water vapour mass to the total parcel's mass ).

The reduced pressure can therefore be calculated by

$$p = p_0 \exp^{-\frac{\bar{h} * g * M}{R * T_v}} \tag{6-9}$$

where $\bar{h}$ is the difference in height between grid point and station height, g is gravity, M is the molar mass of dry air, and R is the universal gas constant.

Pressure, temperature, and water vapour pressure estimates from the GPT2 model are then input into the Saastamoinen model to predict ZHD and ZWD.

### 6.1.4. EGNOS

The European Geo-stationary Navigation Overlay System (EGNOS) tropospheric model (Collins and Langley, 1997) calculates ZTD dependent on height, latitude, and day of year. Meteorological parameters of pressure, temperature, water vapour pressure, temperature lapse rate and water vapour lapse rate were interpolated from yearly means derived from the COESA (1966) North American meteorological data set in 15° latitudinal bands. A sinusoidal function was fitted through the data to account for seasonal variations; an example of the equation for calculating temperature is shown in equation (6-10). The average and amplitude values for the meteorological parameters are included in Table 6-1 and Table 6-2.

$$T_{(\varphi,doy)} = T_0(\varphi) - \Delta T(\varphi) \cdot cos\left(\frac{2\pi(doy - 28)}{365.25}\right) \quad (6\text{-}10)$$

Table 6-1. Averages of pressure, temperature, water vapour pressure, temperature lapse rate (β), and water vapour pressure lapse rate (Λ) in the EGNOS tropospheric model.

| Average | | | | | |
|---|---|---|---|---|---|
| Latitude (deg) | Pressure (mbar) | Temperature (K) | Water vapour pressure (mbar) | B (K m$^{-1}$) | Λ (-) |
| ≤15 | 1013.25 | 299.65 | 26.31 | 0.00630 | 2.77 |
| 30 | 1017.25 | 294.15 | 21.79 | 0.00605 | 3.15 |
| 45 | 1015.75 | 283.15 | 11.66 | 0.00558 | 2.57 |
| 60 | 1011.75 | 272.15 | 6.78 | 0.00539 | 1.81 |
| ≥75 | 1013.00 | 263.65 | 4.11 | 0.00453 | 1.55 |

Table 6-2. Amplitudes of pressure, temperature, water vapour pressure, temperature lapse rate (β), and water vapour pressure lapse rate (Λ) in the EGNOS tropospheric model.

| | Amplitude | | | | |
|---|---|---|---|---|---|
| Latitude (deg) | Pressure (mbar) | Temperature (K) | Water vapour pressure (mbar) | β (K m$^{-1}$) | Λ (-) |
| ≤15 | 0.00 | 0.00 | 0.00 | 0.0000 | 0.00 |
| 30 | -3.75 | 7.00 | 8.85 | 0.0025 | 0.33 |
| 45 | -2.25 | 11.00 | 7.24 | 0.0032 | 0.046 |
| 60 | -1.75 | 15.00 | 5.36 | 0.0081 | 0.074 |
| ≥75 | -0.50 | 14.50 | 3.39 | 0.0062 | 0.30 |

The computed meteorological parameters are then used to compute ZWD and ZHD at sea level using equations (6-11) and (6-12)

$$ZHD_0 = \left(\frac{10^{-6} k_1 R_d P_0}{g_m}\right) \tag{6-11}$$

$$ZWD_0 = \frac{10^{-6} k_2 R_d}{g_m(\lambda + 1) - \beta R_d} \cdot \frac{e_0}{t_0} \tag{6-12}$$

Where $k_1$ and $k_2$ are 77.6 K mbar$^{-1}$ and 382000 K$^2$ mbar$^{-1}$, $R_d$ is 287.054 J kg $^{-1}$K$^{-1}$, and $g_m$ is 9.784 m s$^{-2}$.

The resulting ZWD and ZHD are scaled to the station height using equations (6-13) and (6-14). The EGNOS model also includes the Black and Eisner (1984) mapping function for both ZHD and ZWD.

$$ZHD = ZHD_0 \left[1 - \frac{\beta H_0}{T_0}\right]^{\frac{g}{R_d \beta}} \tag{6-13}$$

$$ZWD = ZWD_0 \left[1 - \frac{\beta H_0}{T_0}\right]^{\frac{(\lambda+1)g}{R_d\beta}-1} \quad (6\text{-}14)$$

Where g is 9.80665 m $s^{-2}$.

### 6.1.5. UNB3m

The University of New Brunswick 3 modified (UNB3m) tropospheric model (Leandro *et al.*, 2008) uses the same averaged dataset as the EGNOS model, except with relative humidity values instead of water vapour pressure. Relative humidity is used because of the water vapour pressure values in the EGNOS model result in a predicted relative humidity of greater than 100% at certain locations. The average and amplitude values for relative humidity as displayed in Table 6-3 were calculated from the COESA (1966) dataset and input into the model. The resulting relative humidity is then converted to water vapour pressure using the conventions outlined in McCarthy and Petit (2004).

Table 6-3. Average and annual amplitude of relative humidity used in UNB3m. All values are represented as a percentage.

| Latitude (deg) | Average | Amplitude |
|---|---|---|
| ≤15 | 75 | 0.0 |
| 30 | 80 | 0.0 |
| 45 | 76 | -1.0 |
| 60 | 77.5 | -2.5 |
| ≥75 | 82.5 | 2.5 |

UNB3m uses the same ZHD and ZWD equations as used in the EGNOS model. Apart from the different method to account for water vapour pressure the UNB3m model uses a $k_3$ value of 377600 $K^2$ $mbar^{-1}$, and uses the Niell mapping function (Niell, 1996) that maps the hydrostatic and wet part of the atmosphere separately.

The UNB3m model was validated against a six year (1990 - 1996) North American radiosonde ray-tracing data set for 223 stations. For the latitudinal band 45° to 60° north the mean and standard deviation of the ZWD estimation errors were -1 mm and 37 mm respectively. The mean ZWD estimation error for all latitudes was found to increase with height, with a mean difference of 1 mm at a height range of 0 - 500 m rising to -35 mm for sites between 1500 - 2000 m.

## 6.2. Empirical tropospheric models at SNLB and SNSU

The empirical tropospheric models listed in section 6.1 were initially tested at the GNSS stations on stable platforms (SNLB and SNSU) at the extremities of the trajectory of the GNSS station on a moving platform (SNTR), allowing direct comparisons of modelled delays to the reference values described in Chapter 5.

Pressure and temperature from the empirical tropospheric models (excluding EGNOS that does not directly provide prediction of meteorological parameters at a station's height) are displayed in Figure 6-1 for a one year period. The harmonic variation used to account for seasonal variations is apparent for the Saastamoinen with GPT and GPT2 input and UNB3m. The semi-annual harmonics used in the Saastamoinen with GPT2 are also apparent in the pressure time series for SNLB. If the largest variations in the pressure and temperature between the models are considered, ~9 mbar at SNSU and 27 K at SNLB around day of year 28, this results in differences in ZHD and ZWD (dependent on the model specific partial pressure of water vapour) of around ~20 mm and ~60 mm respectively.

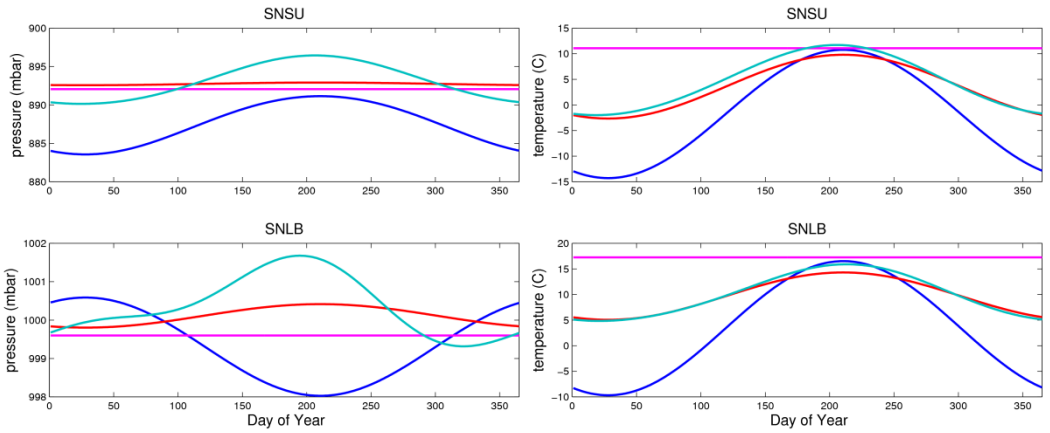


Figure 6-1. Pressure (left panes) and temperature (right panes) time series used in the empirical tropospheric models UNB3m (blue), Saastamoinen with GPT input (red), Saastamoinen with GPT2 input (turquoise), and Saastamoinen (magenta), shown for SNLB (lower panes) and SNSU (upper panes).

Estimated ZTDs from the empirical tropospheric models are displayed for an annual cycle in Figure 6-2. Apart from the differences in the mean values and amplitude variations between the models, the difference in day of year when the ZTD maximum occurs for Saastamoinen with GPT2 input is apparent, as the peak is later on in the annual cycle than the fixed phase (fixed to day of year 28) models of Saastamoinen with GPT input, EGNOS, and UNB3m.

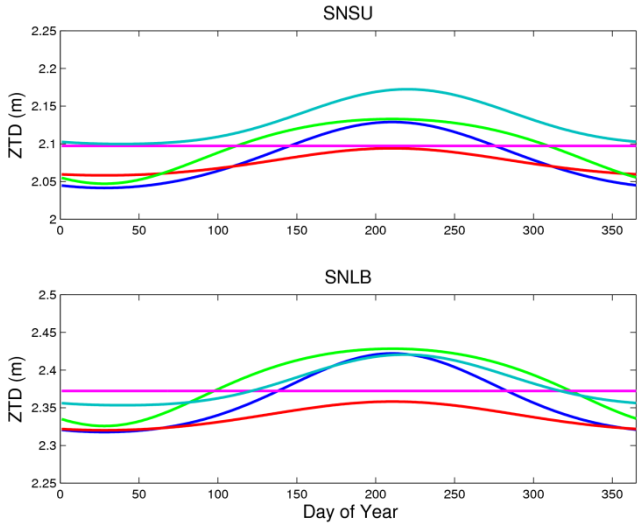


Figure 6-2. ZTD time series obtained from the empirical tropospheric models UNB3m (blue), Saastamoinen with GPT input (red), Saastamoinen with GPT2 input (turquoise), EGNOS (green), and Saastamoinen (magenta), for SNLB (lower pane) and SNSU (upper pane).

## 6.3. Validation of empirical tropospheric models at SNLB and SNSU

The SMR GNSS data set allows empirical tropospheric models used in airborne GNSS positioning to be assessed. The modelled pressure and temperature can be compared to meteorological data collected, while the generated ZWD, ZHD and ZTD can be validated against the reference values described in Chapter 5. Modelled values were initially at the GNSS stations on stable platforms (SNLB and SNSU) located at the extremities of the test site, and at an altitude difference of ~1000 m. Modelled delay values were generated at a 15 minute interval matching the epochs of the reference values for the 50 day test period. Pressure and temperature observed reference values were also linearly interpolated in time to the model-generated epoch time stamp. In the following section orthometric heights will be used with the model, with the Saastamoinen with GPT and GPT2 input models adjusted to accept orthometric rather than ellipsoidal heights.Pressure and ZHDs

Modelled pressure and ZHDs from the empirical tropospheric models are shown in Figure 6-3 together with reference values. The statistical differences of modelled pressure and ZHD from the reference values are given in Table 6-4 and Table 6-5 respectively. Due to hydrostatic elements of the atmosphere being temporally and spatially more stable than water vapour, ZHD can be modelled as a function of atmospheric pressure. All of the empirical modelled ZHD values are within 11 mm of each other at SNLB and SNSU over the 50 day period, and the mean ZHD difference for all the models does not exceed 4.9 mm. The empirical models capture the mean troposphere but can only represent seasonal behaviour, with the large RMS and standard deviations demonstrating the limitations of the empirical models over hourly and daily periods. Here, it should be considered that the location of the SMR dataset is in the same hemisphere and similar latitudes as the US meteorology dataset used in the EGNOS and UNB3m models. Jin *et al.* (2007) showed differences in the seasonal variability of ZTD between the hemispheres. The assumption that the southern hemisphere is a mirror of its northern counterpart could therefore lead to greater errors in the modelled delay values in the southern hemisphere. Lagler *et al.* (2013) highlighted the distribution of higher RMS differences values in the southern

hemisphere and low latitude regions (equatorial areas) in the Saastamoinen with GPT input model when compared to a global pressure observations network. Saastamoinen with GPT2 input offers an improvement on the poorly represented southern hemisphere in Saastamoinen with GPT input, which is attributed to the enhanced spatial resolution (5° compared to 15°) of the sampled ERA interim dataset.

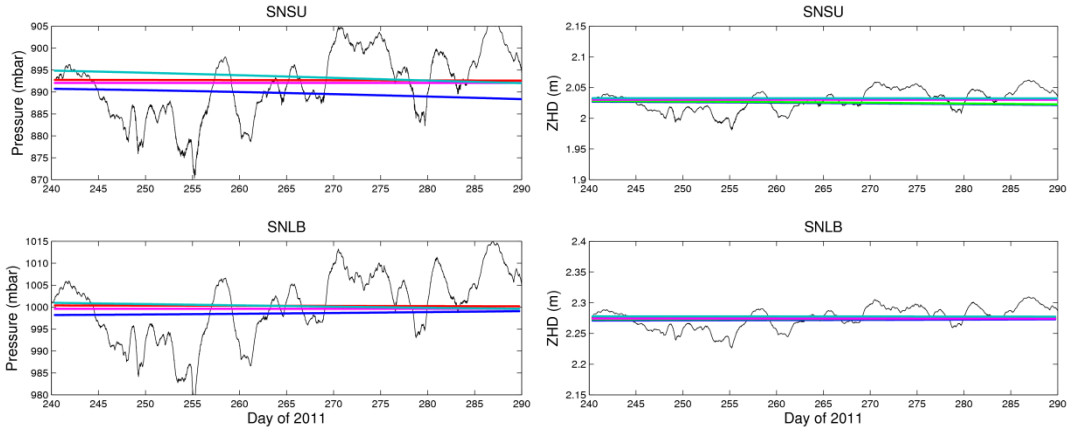


Figure 6-3. Pressure (left panes) and the resulting ZHD (right panes) time series from reference values ( black) and from the empirical tropospheric models UNB3m (blue), Saastamoinen with GPT input (red), Saastamoinen with GPT2 input (turquoise), and Saastamoinen (magenta), for SNLB (lower panes) and SNSU (upper panes) for DOY 240 - 289. ZHD from the EGNOS tropospheric model (green) is included in the right panes.

Table 6-4. RMS, standard deviation, median, and mean of the differences between modelled pressures from the UNB3m, Saastamoinen, Saastamoinen with GPT input, and Saastamoinen with GPT2 input empirical tropospheric models with respect to the reference values at SNLB and SNSU. All quantities are expressed in mbar.

| | SNLB | | | | SNSU | | | |
|---|---|---|---|---|---|---|---|---|
| | RMS | STD | Median | Mean | RMS | STD | Median | Mean |
| UNB3m | 7.7 | 7.6 | -2.6 | -1.5 | 8.3 | 8.1 | -2.7 | -2.1 |
| Saastamoinen | 7.8 | 7.7 | -1.7 | -0.5 | 7.6 | 7.3 | -0.4 | 0.3 |
| SAAST (GPT) | 7.8 | 7.8 | -0.7 | 0.6 | 7.8 | 7.7 | 0.6 | 1.2 |
| SAAST (GPT2) | 8.0 | 8.0 | -1.2 | 0.2 | 8.3 | 8.2 | 1.2 | 1.7 |

Table 6-5. RMS, standard deviation, median, and mean of the differences between modelled ZHD from the EGNOS, UNB3m, Saastamoinen, Saastamoinen with GPT input, and Saastamoinen with GPT2 input empirical tropospheric models with respect to reference values at SNLB and SNSU. All quantities are expressed in mm.

| | SNLB | | | | SNSU | | | |
|---|---|---|---|---|---|---|---|---|
| | RMS | STD | Median | Mean | RMS | STD | Median | Mean |
| EGNOS | 17.4 | 17.3 | -4.2 | -1.7 | 18.8 | 18.4 | -5.4 | -3.9 |
| UNB3m | 17.6 | 17.3 | -5.9 | -3.3 | 19.0 | 18.4 | -6.3 | -4.8 |
| Saastamoinen | 17.7 | 17.6 | -3.9 | -1.1 | 17.4 | 17.4 | -0.9 | 0.6 |
| SAAST(GPT) | 17.8 | 17.7 | -1.6 | 0.5 | 17.7 | 17.5 | 1.3 | 2.7 |
| SAAST(GPT2) | 18.3 | 18.2 | -0.9 | 2.2 | 19.2 | 18.6 | 3.7 | 4.9 |

### 6.3.2. Temperature and ZWDs

Modelled temperature and ZWDs from the tested tropospheric models are shown with reference values in Figure 6-4. The statistical differences of modelled temperature and ZWD from the reference values are displayed in Table 6-6 and Table 6-7 respectively. Even though the magnitude of ZWD is ~10% of ZHD it can be seen from the reference time series that the ZWD over the 50 day period can vary by up to 150 mm, with the variation in ZWD occurring in a short period as demonstrated by the fluctuations between day of year 275 and 280.

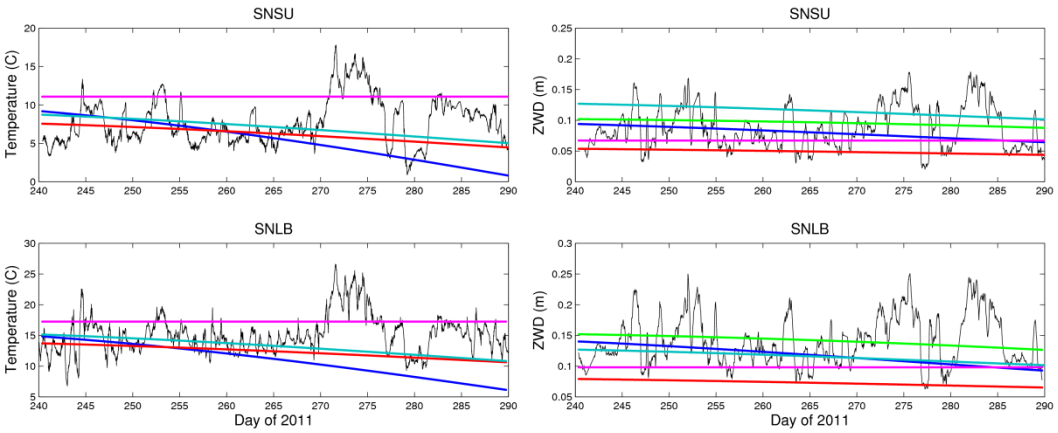


Figure 6-4. Temperature (left panes) and ZWD (right panes) time series reference values (black) and from the empirical tropospheric models UNB3m (blue), Saastamoinen with GPT input (red), Saastamoinen with GPT2 input (turquoise), and Saastamoinen (magenta), for SNLB (lower panes) and SNSU (upper panes) for DOY 240 - 289. ZWD from the EGNOS tropospheric model (green) is included in the right panes.

Table 6-6. RMS, standard deviation, median, and mean of the differences between modelled temperatures from the UNB3m, Saastamoinen, Saastamoinen with GPT input, and Saastamoinen with GPT2 input empirical tropospheric models with respect to the reference values at SNLB and SNSU. All quantities are expressed in Kelvin.

| | SNLB | | | | SNSU | | | |
|---|---|---|---|---|---|---|---|---|
| | RMS | STD | Median | Mean | RMS | STD | Median | Mean |
| UNB3m | 6.1 | 4.3 | -3.3 | -4.3 | 4.9 | 4.2 | -1.2 | -2.5 |
| Saastamoinen | 3.7 | 3.1 | 2.4 | 2.0 | 4.4 | 3.0 | 3.7 | 3.2 |
| SAAST(GPT) | 4.5 | 3.4 | -2.5 | -2.9 | 3.7 | 3.3 | -1.0 | -1.7 |
| SAAST(GPT2) | 4.1 | 3.6 | -1.5 | -2.1 | 3.5 | 3.4 | -0.2 | -0.9 |

Table 6-7. RMS, standard deviation, median, and mean of the differences between modelled ZWD from the EGNOS, UNB3m, Saastamoinen, Saastamoinen with GPT input, and Saastamoinen with GPT2 input empirical tropospheric models with respect to the reference values at the SNLB and SNSU. All quantities are expressed in mm.

| | SNLB | | | | SNSU | | | |
|---|---|---|---|---|---|---|---|---|
| | RMS | STD | Median | Mean | RMS | STD | Median | Mean |
| EGNOS | 41.6 | 41.6 | 11.0 | 0.1 | 36.2 | 35.3 | 16.0 | 7.9 |
| UNB3m | 49.9 | 43.9 | -13.3 | -23.7 | 37.4 | 36.4 | 1.4 | -8.3 |
| Saastamoinen | 58.8 | 40.1 | -35.1 | -43.0 | 40.7 | 34.8 | -15.2 | -21.1 |
| SAAST(GPT) | 79.6 | 40.8 | -58.7 | -68.4 | 52.6 | 35.1 | -31.7 | -39.1 |
| SAAST(GPT2) | 44.4 | 41.7 | -4.3 | -15.2 | 44.9 | 36.1 | 36.1 | -26.8 |

Saastamoinen with GPT input estimates the overall temperature better than UNB3m with smaller STD and median biases. The modelled ZWD from Saastamoinen with GPT input is poorer than the UNB3m model though, with a median ZWD bias of -58.7 mm and -31.7 mm compared to 11.0 mm and 16.0 mm for SNLB and SNSU respectively. The consequence of the poor ability to model the ZWD even though the overall temperature is estimated with a lower mean difference is due to the use of setting relative humidity to 50% in the Saastamoinen model. If relative humidity is set to 75%, a similar value used in UNB3m, then the mean difference in ZWD using GPT for SNLB and SNSU reduces from -68.4 mm and -39.2 mm to -31.6 mm and -12.6 mm respectively. The average relative humidity value for SNLB and SNSU from UNB3m is 76.2% and 74% respectively.

Saastamoinen with GPT2 input provides partial water vapour pressure from the sampled ERA40 interim model dependent on latitude, longitude and day of year. The average water vapour pressure from GPT2 is 12.5 mbar and 11.2 mbar for SNLB and SNSU respectively. If the water vapour pressure is converted to relativity humidity using the IERS Conventions (McCarthy and Petit, 2004) and following the method used in UNB3m the resulting relative humidity at SNLB and SNSU is 82.7% and 111.7% respectively (suggesting an overestimation of water vapour pressure from the GPT2 model). The median ZWD difference for SNLB and SNSU using GPT2 is -4.3 mm and 36.1 mm, with the larger error at SNSU corresponding to the over-estimation of water vapour pressure.

The estimated mean temperature at a station height also relies on the temperature lapse rate used. The large variability in the temperature lapse rate calculated between SNLB and SNSU can be seen in Figure 6-5 along with the temperature lapse rates from the models. The tropospheric models are within 1 K $km^{-1}$ of the average reference temperature lapse rate, but can differ by up to 6 K $km^{-1}$. The large variability in temperature, temperature lapse rate, and water vapour pressure accounts for difficulties in an empirical model to represent ZWD.

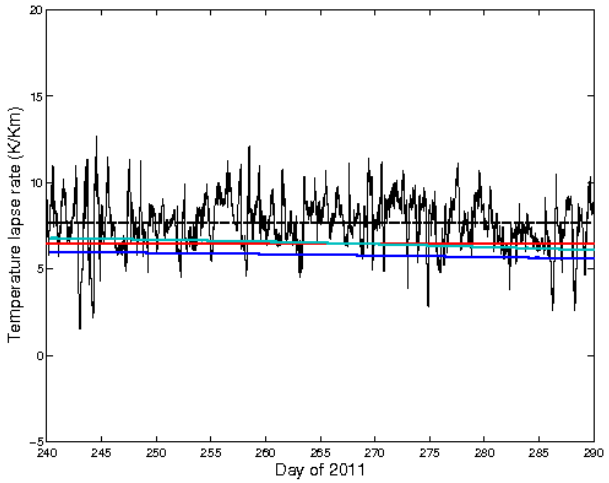


Figure 6-5. Temperature lapse rates from SNLB and SNSU (continuous black line), Mean temperature lapse rate from SNLB and SNSU (dashed black line), EGNOS temperature lapse rate (green), UNB3m temperature lapse rate (blue), GPT temperature lapse rate (red), and GPT2 temperature lapse rate (turquoise).

### 6.3.3. ZTDs

Modelled ZTDs from the empirical tropospheric models are shown with reference values in Figure 6-6. The statistical differences of modelled ZTDs from the reference values are displayed in Table 6-8. The error in ZTD is dominated by the error in the ZWD due to the high spatial and temporal variability of atmospheric water vapour (Mendes *et al.*, 1995). The higher variability of water vapour can be seen in the larger statistical differences of ZWD displayed in Table 6-7 compared to the smaller ZHD statistical differences in Table 6-5, with the EGNOS model at SNSU having an RMS of 36.2 mm for ZWD compared to an RMS of 18.8 mm for ZHD. The EGNOS model is the most representative of the mean ZTD for SNLB and SNSU. The maximum difference in ZTD between the optimal tropospheric models tested (EGNOS) and reference values is 133 mm and a standard deviation of 47 mm. The high maximum difference and standard deviation values for the optimal model highlight the limitations of empirical models to emulate the variations in ZTD. An error in the mitigation of ZTD can be considered to map into the error in height by a factor of three (Santerre, 1991), due to limitations in mapping the delay from the satellite elevation angle to the zenith.

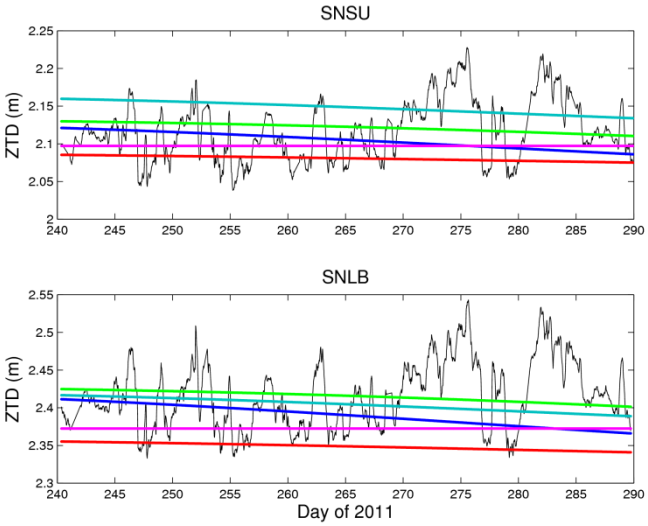


Figure 6-6. ZTD time series from reference values (black) and from the empirical tropospheric models UNB3m (blue), EGNOS (green), Saastamoinen with GPT input (red), Saastamoinen with GPT2 input (turquoise), and Saastamoinen (magenta), for SNLB (lower panes) and SNSU (upper panes) for DOY 240 - 289.

Table 6-8. RMS, standard deviation, median, and mean of the differences between modelled ZTD from the EGNOS, UNB3m, Saastamoinen, Saastamoinen with GPT, and Saastamoinen with GPT2 input empirical tropospheric models with respect to the reference values at SNLB and SNSU. All quantities are expressed in mm.

| | SNLB | | | | SNSU | | | |
|---|---|---|---|---|---|---|---|---|
| | RMS | STD | Median | Mean | RMS | STD | Median | Mean |
| EGNOS | 47.0 | 47.0 | 4.0 | -1.6 | 42.4 | 42.3 | 9.1 | 4.0 |
| UNB3m | 57.1 | 50.3 | -21.7 | -27.0 | 46.3 | 44.5 | -8.7 | -13.1 |
| Saastamoinen | 62.4 | 44.2 | -39.1 | -44.0 | 45.1 | 40.2 | -15.5 | -20.4 |
| SAAST(GPT) | 81.3 | 45.8 | -60.7 | -67.1 | 55.0 | 41.2 | -30.9 | -36.4 |
| SAAST(GPT2) | 49.7 | 48.0 | -7.3 | -13.0 | 54.2 | 44.0 | 36.5 | 31.7 |

### 6.3.4. Orthometric and ellipsoidal heights

It should be considered that many GNSS processing packages do not use orthometric heights in tropospheric models but use the more readily available ellipsoidal height. The ellipsoid at the SMR test set is ~55 m above mean sea level. The mean ZTD differences between the reference values and the empirical tropospheric models were compared when ellipsoidal and orthometric heights were input and can be seen in Figure 6-7. Due to the Saastamoinen with GPT and GPT2 input models calculating a

geoid correction of ~52 m for the SMR dataset the differences in ZTD between the inserted height values are less. For UNB3m, EGNOS, and the Saastamoinen model the mean ZTD difference is seen to increase by an average of 17.4 mm and 15.3 mm for SNLB and SNSU respectively if ellipsoidal height is used rather than orthometric.

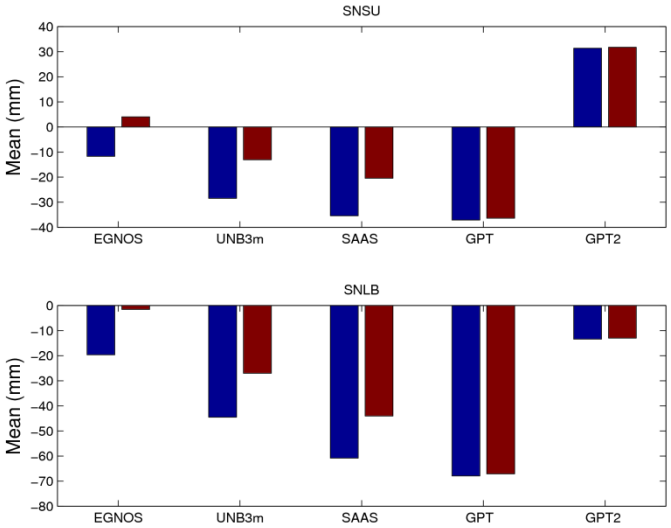


Figure 6-7. Mean ZTD differences for SNLB and SNSU for tropospheric models ENGOS, UNB3m, Saastamoinen, Saastamoinen with GPT input, Saastamoinen with GPT2 input, and Saastamoinen with ellipsoidal heights used (blue), and orthometric heights (red).

The consequence of using the incorrect height propagates mainly from the incorrect modelling of ZHD due to the magnitude of ZHD being a factor of 10 greater than the ZWD. For example the mean ZHD difference at SNLB and SNSU decreases by 14.7 mm and 12.2 mm respectively, while the mean ZWD differences increases by 2 mm and 1.1 mm respectively. If estimating a tropospheric delay in a GNSS solution and local pressure is not available, then an empirical tropospheric model will be used. Even when the ZWD is estimated, using an appropriate model for ZHD is important. Any residual slant delay in either the ZHD or ZWD is mapped by the incorrect mapping function and can result in a bias in the ZTD (Kleijer, 2001).

## 6.4. Validation of empirical tropospheric models at SNTR

To assess empirical tropospheric models for airborne GNSS positioning the tropospheric models outlined in section 6.1 were also tested for the GNSS station on

a moving platform (SNTR). Orthometric heights were used with the models to generate delay values. The differences between modelled ZTD and reference values are displayed in Table 6-9. The lowest mean and median ZTD difference at SNTR are for the UNB3m model, while the EGNOS model provides the smallest RMS. The optimal model is therefore different at SNTR than at SNLB and SNSU, which can be attributed to a difference in the temporal sampling. SNTR is sampled from 0600 to 1900 each day, and does not include day of year 270 and 280 where there is a peak in ZTD (evident in Figure 6-6).

Table 6-9. RMS, standard deviation, median, and mean of the differences between modelled ZTD from the EGNOS, UNB3m, Saastamoinen with relative humidity set to 50%, Saastamoinen with GPT input and relative humidity set to 50%, and Saastamoinen with GPT2 input empirical tropospheric models with respect to the reference values at SNTR between heights 167 - 1120 m. All quantities are expressed in mm.

| | SNTR | | | |
|---|---|---|---|---|
| | RMS | STD | Median | Mean |
| EGNOS | 36.6 | 34.7 | 14.5 | 11.7 |
| UNB3m | 38.3 | 37.4 | -3.7 | -8.3 |
| Saastamoinen | 52.7 | 33.1 | -38.2 | -40.9 |
| SAAST (GPT) | 55.8 | 34.5 | -40.9 | -43.8 |
| SAAST (GPT2) | 41.6 | 37.8 | 20.2 | 17.6 |

The distribution of the ZTD differences for the tropospheric models UNB3m and Saastamoinen at SNTR can be seen from the histograms in Figure 6-8. If the distribution of the ZTD difference for the UNB3m model is analysed 60% of ZTD differences are greater than ±15 mm, and 37% greater than ±30 mm. If the widely used Saastamoinen model is used, 83% of ZTD differences are greater than ±15 mm, and 62% greater than ±30 mm. Even though the tropospheric models such as UNB3m can represent the mean trends of ZTD reasonably well, they cannot represent the highly variable nature of the delay and this is seen in the high percentage of data that is greater than ±30 mm.

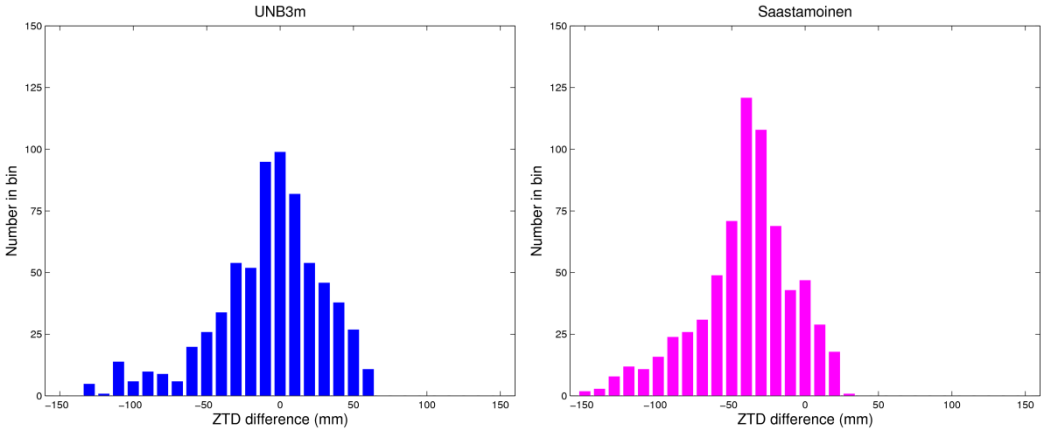


Figure 6-8. Histograms of differences in ZTDs at SNTR between modelled ZTD from the UNB3m (left) and Saastamoinen (right) empirical tropospheric models and reference values. Each bin size represents 10 mm of delay.

The performance of the estimated ZTD for SNTR over a range of altitudes is considered, with the RMS and median calculated in 100 m height bands and shown in Figure 6-9. UNB3m and EGNOS models continue to perform better over the 100 m height bands when compared to the Saastamoinen models using a standard relative humidity at sea level of 50%. The RMS for Saastamoinen with GPT2 input increases with height, an opposite trend to the other models, and supported by the ZTD difference RMS for SNLB and SNSU in Table 6-8.

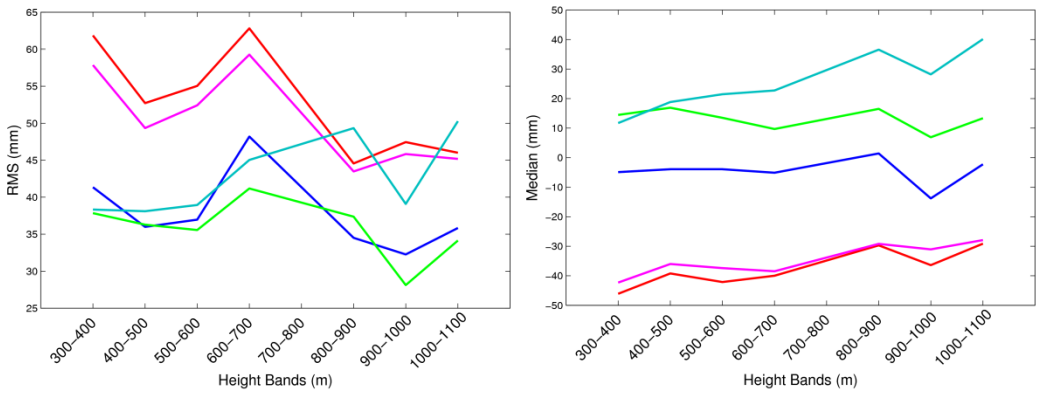


Figure 6-9. ZTD RMS and median differences at SNTR (in 100 m orthometric height bins) between the reference values and each empirical tropospheric model: Saastamoinen with GPT input and relative humidity set to 50% (red), Saastamoinen with GPT2 input (turquoise), UNB3m (blue), EGNOS (green), and Saastamoinen with relative humidity set to 50% (magenta).

Between day of year 270 and 285 the ZTD at SNLB and SNSU is seen to spike and have a greater variability. Therefore the mean ZTD differences for 5 day consecutive windows were calculated and displayed in Figure 6-10, along with ZTD at SNSU. It can be seen that when there is an increase in ZTD between day of year 280 and 285, the mean ZTD difference for each of the models increases. Unfortunately due to a logging fault, SNTR data was not collected between day of year 270 and 279 and therefore the mean ZTD differences are not displayed during this period. The mean ZTD difference from the models between day of year 280 and 285 varies between -79.4 mm and -138.1 mm, this is compared between day of year 285 and 290 with mean ZTD differences between -5.8 mm and -60.5 mm. This highlights the limitation with empirical tropospheric models when real tropospheric conditions vary from the expected tropospheric conditions, and demonstrates the potential magnitude of error that can arise.

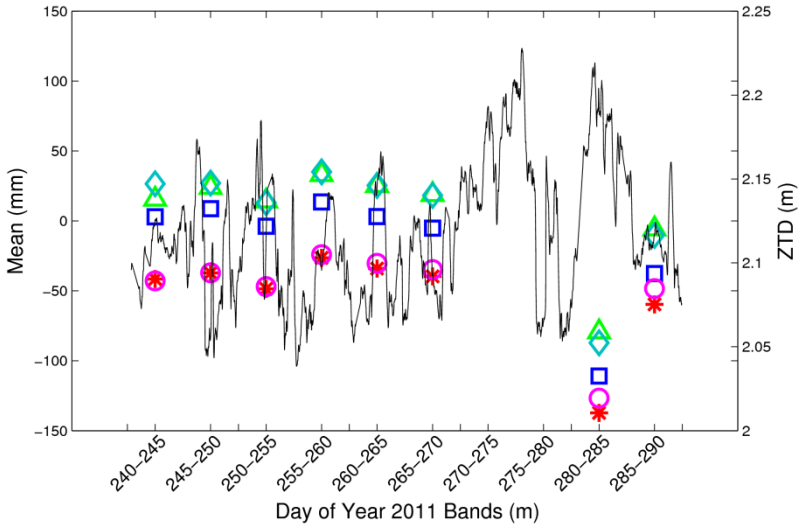


Figure 6-10. Mean ZTD differences for five day windows between the reference values and the following empirical tropospheric models: Saastamoinen with GPT input and relative humidity set to 50% (red asterisk), Saastamoinen with GPT2 input (turquoise diamond), UNB3m (blue square), EGNOS (green triangle), and Saastamoinen with relative humidity set to 50% (magenta circle). The reference values at SNSU are also included (black line, right-hand scale).

## 6.5. Conclusion

A range of empirical tropospheric delay models have been analysed, and their ability to mitigate tropospheric delay benchmarked. The use of GNSS stations on stable and moving platforms has allowed a range of empirical tropospheric models to be tested in a simulated airborne GNSS positioning scenario. The use of co-located pressure and temperature measurements and GPS-derived ZTD estimates as reference values has allowed the models' ability to estimate meteorological parameters and the hydrostatic and wet components of tropospheric delay to be benchmarked.

Without parameterising residual ZTD in absolute GNSS positioning solutions, the unmitigated delay will propagate directly into the height component. The effect of unmitigated delay for relative GNSS positioning in certain scenarios, for example short baselines and small height difference between receivers, is minimal due to the similar observations cancelling errors (including tropospheric delay) in the differencing process (Shan *et al.*, 2007). For airborne GNSS positioning, however, the tropospheric conditions experienced between receivers can be quite different due to a difference

in altitude and the spatial variability of water vapour, therefore the delays will not cancel each other out and the delays must be modelled (Mendes *et al.*, 1995; Collins and Langley, 1997).

The empirical tropospheric models were shown to represent the overall trend of pressure and temperature and therefore ZTD, with models representing the delay with a median range between -3.7 mm and -40.9 mm at the GNSS station on a moving platform (SNTR). However, the variability of the delay has to be considered, with the models unable to emulate the high frequency temporal changes in atmospheric conditions. The median bias of estimated ZHD compared to the pressure derived reference varies between 0.5 mm and 4.9 mm for the models tested at the GNSS station on stable platforms (SNLB and SNSU). The largest maximum ZHD difference at SNLB and SNSU is from the Saastamoinen with GPT2 input model with a magnitude of 55.1 mm, while the UNB3m model has the smallest maximum ZHD difference of 45.2 mm. The larger contribution to the error in ZTD is from the more variable ZWD, even though the magnitude of ZWD is much smaller than the ZHD. The Saastamoinen with GPT input model had the largest maximum ZWD difference of -181.0 mm at SNLB, while the EGNOS model provided the smallest maximum ZWD difference was of 87.7 mm at SNSU.

The UNB3m model was found to provide ZTD time series for SNTR with the smallest mean and median bias, while the EGNOS model provides the smallest RMS. If the range of ZTD differences from UNB3m is examined, the weakness in the models is highlighted, with only 40% of ZTD estimates within ±15 mm of the reference values. The UNB3m model has a maximum ZTD difference of 134.1 mm; this can lead to an error three times this value in the height component of a relative solution (Santerre, 1991). The propagation of errors from the modelled ZTD into kinematic GNSS relative positioning and the consequence of estimating the residual tropospheric delay into the accuracy of the height will be assessed further in Chapter 8.

# 7. Validation of ZWD estimation from kinematic GNSS at a range of altitudes

The provision of measurements of atmospheric water vapour is a key requirement in meteorology and climate studies, with the highly variable spatial and temporal distribution of water vapour directly impacting precipitation patterns and energy transfer in the atmosphere. To improve the ability of NWM to forecast precipitation, accurate atmospheric water vapour measurements are required for assimilation, particularly in otherwise data-sparse areas where NWM precipitation performance is limited, such as deserts, mountains and oceans. Previous studies (Baker *et al.*, 2001; Smith *et al.*, 2007; Karabatić *et al.*, 2011) have suggested that a PWV measurement accuracy approaching 1 - 2 mm is desirable for improving NWMs. This chapter assesses the potential of kinematic GNSS over a range of altitudes to measure PWV, by comparing estimates of ZWD to the tropospheric comparators outlined in Chapter 5.

A recent development in kinematic PPP has been the inclusion of GLONASS as well as GPS observations. The use of a combined system solution is beneficial due to increased redundancy and the increased chance of good satellite geometry, especially in high latitude areas and those with an obstructed sky view, and can also reduce solution convergence times (Cai and Gao, 2013). The use of a multi-system kinematic GNSS solution to retrieve ZTD has been examined over a 24 hour period in Martin (2013) using two GNSS stations on stable platforms with contrasting ZWD daily variations. However, to date there has not been a comprehensive assessment of ZWD retrieval from a multi-system kinematic GNSS solution using a GNSS station on a moving platform. The purpose of this chapter is therefore to assess the retrieval of ZWD using an extensive kinematic GNSS data set, collected over a range of altitudes as experienced in airborne GNSS, rather than at sea level only as used in previous publications based on shipborne experiments.

# 7. Validation of ZWD estimation from kinematic GNSS at a range of altitudes

To allow a rigorous assessment to be undertaken, GNSS data has been collected from a GNSS station on a moving platform (SNTR), with a repeatable trajectory, over a 50 day period, during which a range of meteorological conditions were experienced as described in Chapter 4. The use of interpolated ZWD from two GNSS stations on stable platforms at the extremities of the trajectory and the use of a high resolution NWM, both detailed in Chapter 5, should enable quality control of the ZWD estimates from the kinematic GNSS solutions. In this respect, the use of both absolute GNSS, with multiple GNSS (combined GPS and GLONASS observations) and GPS-only solutions is examined, together with results from relative GNSS.

## 7.1. GNSS processing strategy

Three kinematic GNSS solutions, two PPP and the other double-difference, are compared to the reference ZWD values for SNTR outlined in Chapter 5. Section 7.1 first describes these kinematic GNSS solutions and their ZWD estimation methods, including the tuning of process noise values used in the solutions.

### 7.1.1. Kinematic PPP

Dual GNSS (GPS+GLONASS) and GPS-only data was processed using the PPP software PPPNCL developed in-house (Martin, 2013), which uses an extended Kalman filter to process a time-ordered stream of carrier phase and code pseudorange observations and satellite data, estimating receiver positions, receiver clocks and ZWD as time-varying random-walk parameters, and real-valued carrier phase biases and the GPS+GLONASS system time offset as constant parameters. The ionosphere-free observations were processed at a 1 second interval with ESA final orbits and clocks held fixed, a positional process noise of 1 m $s^{-0.5}$ and a ZWD process noise of 0.1 mm $s^{-0.5}$. The tropospheric and positional process noise values used in the study were first optimised by tuning a 7 day subset of the ZWD estimates for SNTR from PPPNCL against the GIPSY-based interpolated reference ZWDs. The RMS, standard deviation and median of ZWD differences from the tropospheric noise values tested between

day of year 253 - 259 are displayed in Table 7-1. Due to the similar RMS, standard deviation and median of ZWD differences using atmospheric process noise values 0.1 mm $s^{-0.5}$ and 0.2 mm $s^{-0.5}$, solutions were analysed over the entire dataset for these values. The resulting RMS, standard deviation and median differences listed in Table 7-2 indicate that the optimal ZWD process noise for the dataset is 0.1 mm $s^{-0.5}$.

Table 7-1. RMS, standard deviation and median of the differences between ZWDs estimated from kinematic GPS+GLONASS PPP using PPPNCL with a range of tropospheric process noise and the interpolated GIPSY-derived reference values for SNTR for DOY 253 - 259 2011. All quantities are expressed in mm (solutions were computed with the IGS 05 antenna files).

| | SNTR | | |
|---|---|---|---|
| | RMS | STD | Median |
| Tropo. Pro. noise 0.05$mm\ s^{-0.5}$ | 12.8 | 12.8 | 0.4 |
| Tropo. Pro. noise 0.1 $mm\ s^{-0.5}$ | 10.6 | 10.7 | 1.6 |
| Tropo. Pro. noise 0.2$mm\ s^{-0.5}$ | 10.6 | 10.6 | 1.6 |
| Tropo. Pro. noise 0.4$mm\ s^{-0.5}$ | 13.3 | 13.3 | 1.3 |

Table 7-2. RMS, standard deviation and median of the differences between ZWDs estimated from kinematic GPS+GLONASS PPP using PPPNCL with a range of tropospheric process noise and the interpolated GIPSY-derived reference values for SNTR for DOY 240 - 289 2011. All quantities are expressed in mm (solutions were computed with IGS 05 antenna files, therefore results differ from Table 7-5 which used IGS08 antenna files).

| | SNTR | | |
|---|---|---|---|
| | RMS | STD | Median |
| Tropo. Pro. noise 0.1 $mm\ s^{-0.5}$ | 12.1 | 12.1 | 1.9 |
| Tropo. Pro. noise 0.2 $mm\ s^{-0.5}$ | 14.1 | 14.0 | 2.9 |

The Global Mapping Function (GMF) (Boehm *et al.*, 2006a) was used to map slant tropospheric delays to the zenith, with an elevation cut off angle of 7°. The results were post-processed with back-smoothing, that was implemented into the PPPNCL software following the method outlined in Hofmann-Wellenhof *et al.* (2007). A pseudo real-time approach could not be implemented because the railway track is

bordered by trees for a small section near SNLB causing loss of lock, and so a forward-only solution does not converge for the majority of each trajectory.

### 7.1.2. Kinematic double differencing

A double-difference solution was also obtained at a 1 second interval from MIT's GAMIT/GLOBK module Track, version 1.24 (Chen, 1998; Herring *et al.*, 2010). ESA final orbits were held fixed, and coordinates and ZWD estimated using GMF with a cut off angle of $7^{o}$ (the default value of relative humidity in the GMF was altered from 0 to 0.5, similar to an update available in Track version 1.27), and elevation angle dependent observation weighting used. A position process noise of 4 m $s^{-0.5}$ was applied, and a ZWD process noise of 0.01 mm $s^{-0.5}$ plus 0.23 mm $s^{-0.5}$ per m $s^{-1}$ of vertical speed. As with the PPP solution, a back-smoother was applied and the applied process noise values were tuned from a 7 day subset of the reference ZWD estimates for SNTR. The range of tested tropospheric process noise values are included in Table 7-3. A levered troposphere approach was used, with co-located pressure derived reference ZHD and GIPSY-derived reference ZWD values at the fixed end of the baseline being fed into the solution. To do this, Track was modified to accept separate ZHD and ZWD values, and to use the hydrostatic and wet GMF respectively with these input delays. Because Track does not process GLONASS data, only the GPS (L1 and L2 carrier phase, and C/A and P2 pseudoranges) observables were used. The L1 and L2 carrier phase signals were combined linearly to mitigate $1^{st}$ order ionospheric effects, and double-difference carrier phase ambiguities were resolved to integer values using a wide-lane linear combination.

Table 7-3. RMS, standard deviation and median of the differences between ZWDs estimated from kinematic GPS-only double differencing using Track with a range of tropospheric process noise and the interpolated GIPSY-derived reference values for SNTR for DOY 253 - 259 2011. All quantities are expressed in mm.

| | SNTR | | |
|---|---|---|---|
| | RMS | STD | Median |
| Tropo. Pro. noise 0.001 $mm\ s^{-0.5}$ | 16.0 | 16.1 | 0.7 |
| Tropo. Pro. noise 0.01 $mm\ s^{-0.5}$ | 15.8 | 15.9 | 0.7 |
| Tropo. Pro. noise 0.05 $mm\ s^{-0.5}$ | 21.4 | 21.5 | 1.7 |

## 7.2. Performance of kinematic GNSS at SNLB and SNSU

Estimated ZWDs from each of the three kinematic GNSS solutions (GPS+GLONASS PPP, GPS-only PPP, GPS-only double differencing) were compared to the GIPSY-derived reference values at 15 minute intervals for the 50 day data span at the two GNSS stations on stable platforms (SNLB and SNSU). ZWD derived from a high-resolution NWM, the Met Office Unified Model, was also compared which is completely independent of the Snowdon GNSS data. For each technique tested, ZWD difference values greater than five times the mean absolute deviation were considered outliers and excluded from the analysis, with the proportion of outliers not exceeding 0.7%, except for the long baseline GPS-only double differencing solution (described in section 7.3) for which it was up to 2.2%. The PPP solutions were obtained as if for a moving platform, using the process settings outlined in section 7.1.1. For the GPS-only double differencing solution SNLB and SNSU were processed relative to each other, with the station of interest being processed as if on a moving platform and the alternate station being held fixed as per a stable platform. The use of SNLB and SNSU should allow benchmarking of the optimal performance of the methods at the vertical extremities of the experimental domain, but in an idealised situation lacking vehicle dynamics (and less multipath than that experienced by SNTR). The quality of each of the methods is illustrated as differences in estimated ZWD from the reference values over the entire data set (in Figure 7-1), and for a sample 5 day period that experiences a large variation in ZWD (in Figure 7-2). The RMS, standard deviations, and median

differences of the estimates, with respect to the reference values, are also displayed in Table 7-4.

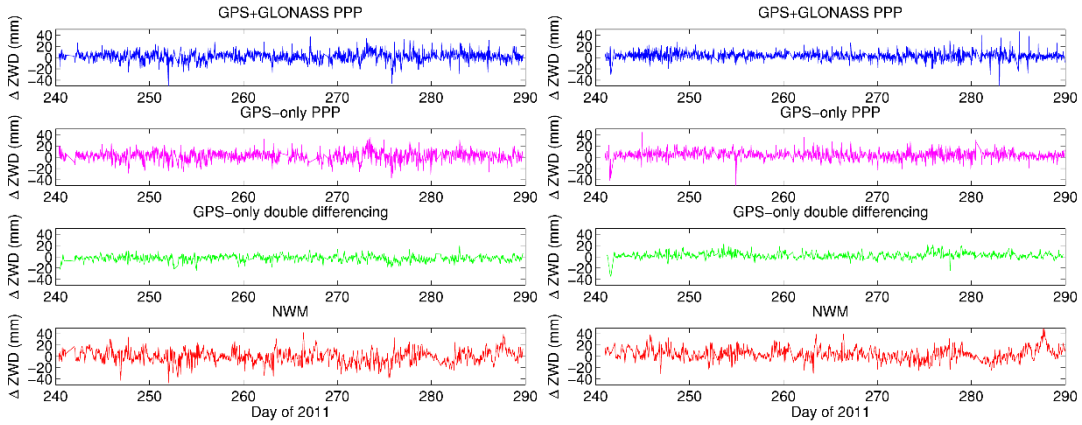


Figure 7-1. ZWD differences between the estimations from kinematic GPS+GLONASS PPP, kinematic GPS-only PPP, kinematic GPS-only double differencing, and Unified Model, and the GIPSY-derived reference values for SNLB (left pane) and SNSU (right pane).

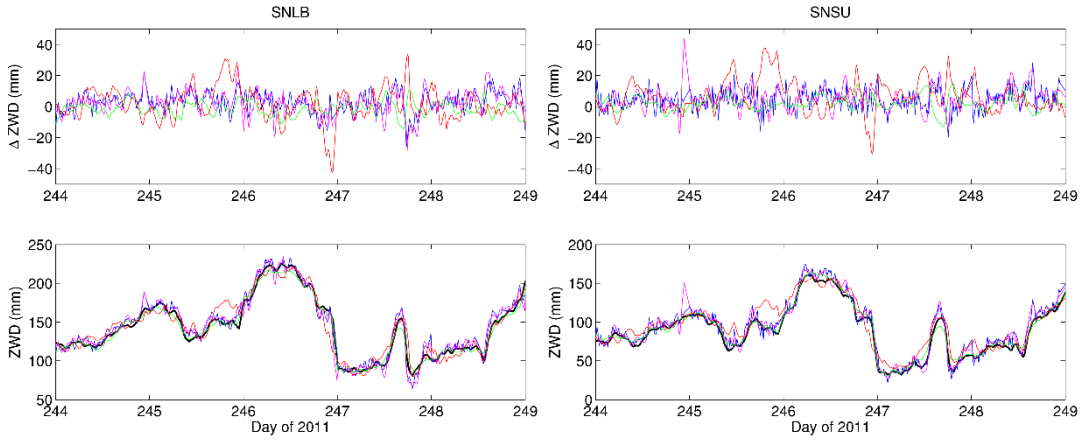


Figure 7-2. ZWD differences between the estimations from kinematic GPS+GLONASS PPP (blue), kinematic GPS-only PPP (magenta), kinematic GPS-only double differencing (green), and Unified Model (red), and the GIPSY-derived reference values for the SNLB and SNSU on DOY 244 - 248 of 2011 (upper panes). Lower panes show the ZWD time series for each estimation method and the reference values (black).

Table 7-4. RMS, standard deviation and median of the differences between ZWDs estimated from kinematic GPS+GLONASS PPP, kinematic GPS-only PPP, kinematic GPS-only double differencing (DD), and Unified Model with respect to the GIPSY-derived reference values, at SNLB and SNSU. All quantities are expressed in mm.

| | SNLB | | | SNSU | | |
|---|---|---|---|---|---|---|
| | RMS | STD | Median | RMS | STD | Median |
| Kinematic GPS+GLONASS PPP | 7.7 | 7.4 | 2.1 | 6.4 | 5.4 | 3.4 |
| Kinematic GPS-only PPP | 8.4 | 8.2 | 2.5 | 7.5 | 6.3 | 3.8 |
| Kinematic GPS-only DD | 5.3 | 4.7 | -2.2 | 5.3 | 4.6 | 2.3 |
| Unified Model | 11.0 | 11.0 | -0.5 | 11.0 | 10.2 | 3.5 |

The ZWD differences for kinematic GPS+GLONASS PPP show standard deviations and RMS values between 5.4 and 7.7 mm, and biases between 2.1 and 3.4 mm, when estimated at a GNSS station on a stable platform; this is an improvement on the 12 - 18 mm ZWD RMS agreements of previous low-dynamic shipborne studies (Rocken *et al.*, 1995; Boniface *et al.*, 2012). In fact, the kinematic PPP solutions have an RMS, standard deviation and bias almost commensurate with those from static PPP solutions, even though some degradation might be expected, due to the weakened geometry caused by unknown receiver dynamics. Furthermore, the RMS values are very similar (within 2 - 3 mm, or 0.5 mm PWV) to those for kinematic GPS-only double differencing, suggesting that the absolute GNSS solutions are comparable to the relative GNSS solution with a moderately short (~6 km) baseline. NWM differences of 11.0 mm RMS are commensurate with previous studies (Skone *et al.*, 2006; Boniface *et al.*, 2012), and demonstrate the ability of the NWM to be used as a quality control for the kinematic GNSS estimates of ZWD along the trajectory. However, these differences are larger than those for the PPP and double-difference estimates, which suggest that even this high-resolution model (the driving UK4 model) could benefit from the assimilation of GNSS-based ZWD.

## 7.3. Performance of kinematic GNSS at SNTR

Estimated ZWDs from each of the three kinematic GNSS solutions (GPS+GLONASS PPP, GPS-only PPP, and GPS-only double-difference) and from the Unified Model were

compared to the GIPSY-derived reference values at 15 minute intervals at the GNSS station on a moving platform (SNTR). Due to equipment difficulties, no SNTR data was collected between day of year 270 - 280. The RMS, standard deviations and medians of the differences in ZWD with respect to the reference values are listed in Table 7-5. Differences were only included in the statistical analysis if they were recorded under truly kinematic conditions, i.e. when SNTR was moving when outside of the Llanberis and Snowdon summit railway termini at which it made lengthy stops (occasional brief pauses at intermediate stations were neglected). Estimated ZWD for SNTR and the interpolated reference values, and their differences, are shown for a sample day (day of year 264) in Figure 7-3. The correlations between the estimates and the reference values can also be seen in Figure 7-4.

Table 7-5. RMS, standard deviation and median of the differences between ZWDs estimated from kinematic GPS+GLONASS PPP, kinematic GPS-only PPP, kinematic GPS-only double differencing, the Unified Model and the interpolated GIPSY-derived reference values for SNTR. All quantities are expressed in mm.

| | SNTR | | |
|---|---|---|---|
| | RMS | STD | Median |
| Kinematic GPS+GLONASS PPP | 11.6 | 11.6 | 1.8 |
| Kinematic GPS-only PPP | 16.2 | 15.3 | 4.9 |
| Kinematic GPS-only DD | 12.1 | 11.8 | 2.6 |
| Unified Model | 10.8 | 9.4 | 4.8 |

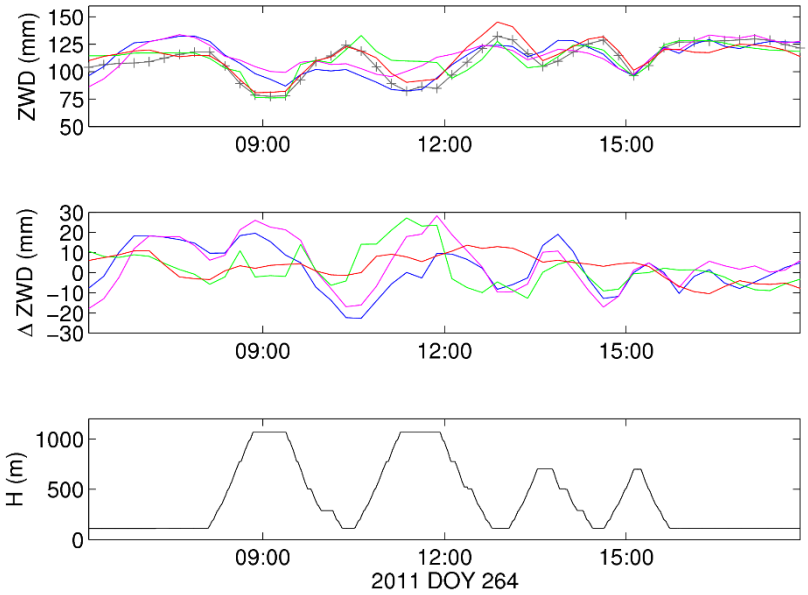


Figure 7-3. Top: ZWD time series on sample 2011 DOY 264 obtained from kinematic GPS+GLONASS PPP (blue), kinematic GPS-only PPP (magenta), kinematic GPS-only double differencing (green), and Unified Model (red) for SNTR, and the GIPSY-derived interpolated reference ZWD values (grey with crosses at comparison epochs). Middle: differences between each estimation method and the reference ZWD. Bottom: height of SNTR above mean sea level.

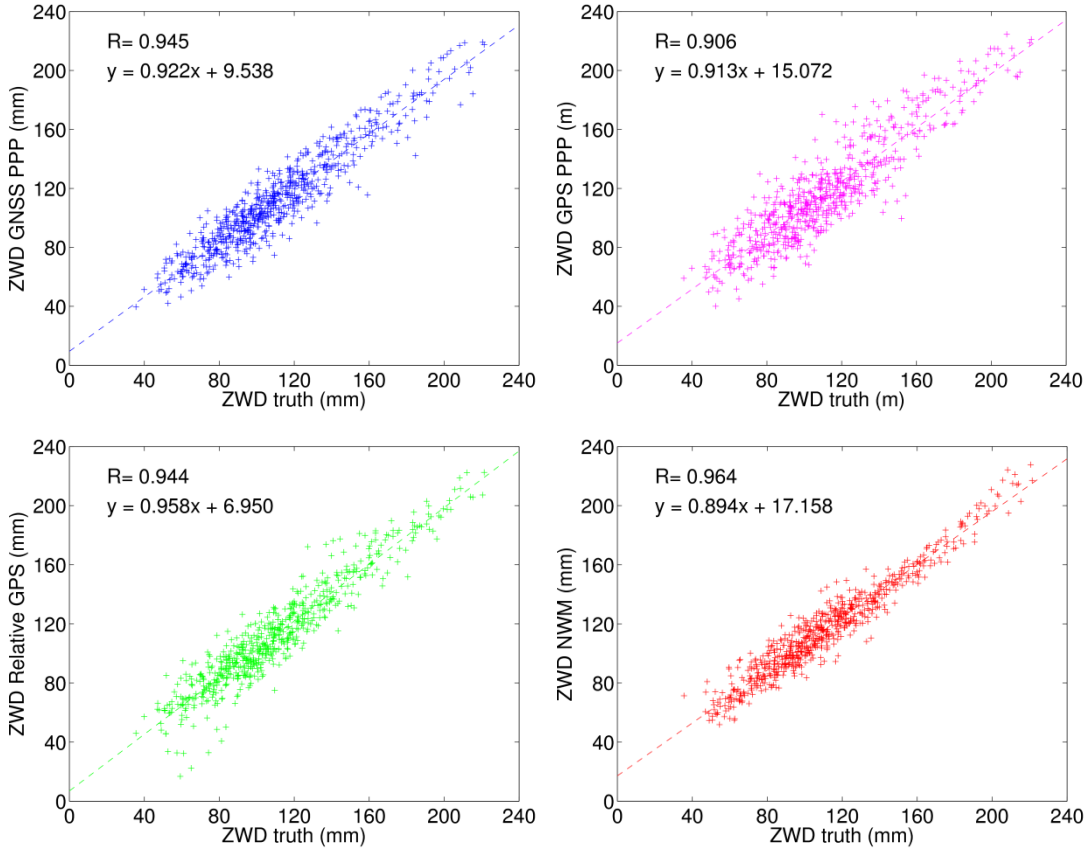


Figure 7-4. Correlation between ZWD estimated by each method and the interpolated reference values. Upper left: kinematic GPS+GLONASS PPP; Upper right: Kinematic GPS-only PPP; Lower left: kinematic GPS-only double differencing; Lower right: Unified Model.

The ZWD difference for kinematic GPS+GLONASS PPP have an RMS of 11.6 mm (correlation coefficient of 0.945), which is at least commensurate with previous shipborne studies. Kinematic GPS-only double differencing provides similar accuracy to kinematic GPS+GLONASS PPP, with an RMS agreement of 12.1 mm, but it is important to note that this is an optimal setup for relative GNSS: with a maximum baseline length of 6.1 km such as is not routinely available for airborne GNSS. When the same comparison was made for a kinematic GPS-only double-difference solution relative to the nearest Ordnance Survey CGNSS station ASAP (situated at a height above sea level of 50 m, similar to SNLB, but 45 km away), there was a reduction in the RMS agreement to 23 mm. Processing relative to multiple OS CGNSS stations (ASAP and ADAR) yielded an RMS difference of 19.2 mm, an improvement over a single long baseline but still not as good as PPP. The RMS between the NWM and the interpolated GIPSY-derived reference values is 11.2 mm, commensurate with the SNLB

and SNSU validations. This gives further confidence in the quality of the interpolated reference values. It can also be noted that if there is no estimation of the tropospheric delay from the GNSS solution, the empirical tropospheric model of Saastamoinen with GPT input only provides an RMS, standard deviation, and median of 95.7 mm, 36.3 mm, and -85.4 mm respectively, which are significantly worse than any of the estimates of ZWD.

To assess any variation in the performance of the different ZWD estimation methods with height, the ZWD difference statistics were computed in 100 m height bins, and the RMS differences are shown in Figure 7-5. There is no obvious degradation with height for any of the three methods. This provides further validation of the NWM as a control in the experiment, and indicates the potential for using kinematic GNSS estimates of ZWD not just from ships and ground-based vehicles but also aircraft.

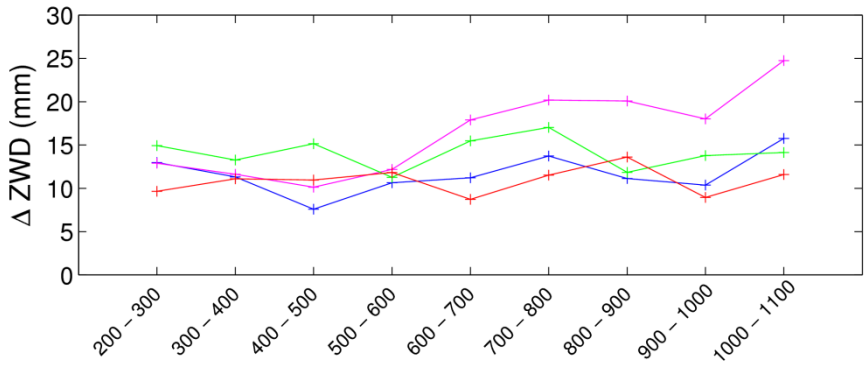


Figure 7-5. ZWD RMS differences (in 100 m ellipsoidal height bins) between the GIPSY-derived reference ZWD and each of the estimation methods: kinematic GPS+GLONASS PPP (blue), Kinematic GPS-only PPP (magenta), kinematic GPS-only double differencing (green), Unified Model (red).

As all previous shipborne studies of kinematic PPP estimates of ZWD used GPS-only, the difference between kinematic GPS-only and combined GPS+GLONASS PPP solutions is now considered. At SNLB and SNSU, neither solution provided a notable improvement over the other, with RMS and median agreements between kinematic GPS-only and GPS+GLONASS PPP solutions of up to 1.1 mm and 0.4 mm respectively. However, it is important to note that these GNSS stations are at 'clean' sites, with clear

sky views, and so the improved satellite geometry of a GPS+GLONASS solution is expected to have less impact.

The RMS, standard deviation and median ZWD differences from the interpolated SNTR reference values, for kinematic GPS-only and GPS+GLONASS PPP are displayed in Figure 7-6 for each day of the complete 50 day dataset. As was shown in Table 7-5, kinematic GPS-only PPP has a total RMS, standard deviation, and median difference of 16.2 mm, 15.3 mm, 4.9 mm respectively and a correlation coefficient of 0.906 with respect to the interpolated reference. In this respect, the kinematic GPS-only PPP solution collected over a range of heights is closely comparable to previous shipborne studies such as Boniface *et al.* (2012) and Rocken *et al.* (2005). The inclusion of GLONASS offers appreciable improvement, with a correlation coefficient of 0.945 and an RMS, standard deviation, and median difference of 11.6 mm, 11.6 mm, and 1.8 mm; equating to an RMS PWV agreement of around 2 mm. Such an improvement is likely due to the higher number of visible satellites, coupled with a better distribution of these satellites, resulting in more redundancy in the solution. This suggests that a combined GPS+GLONASS solution should be adopted for the optimal kinematic GNSS estimation of ZWD.

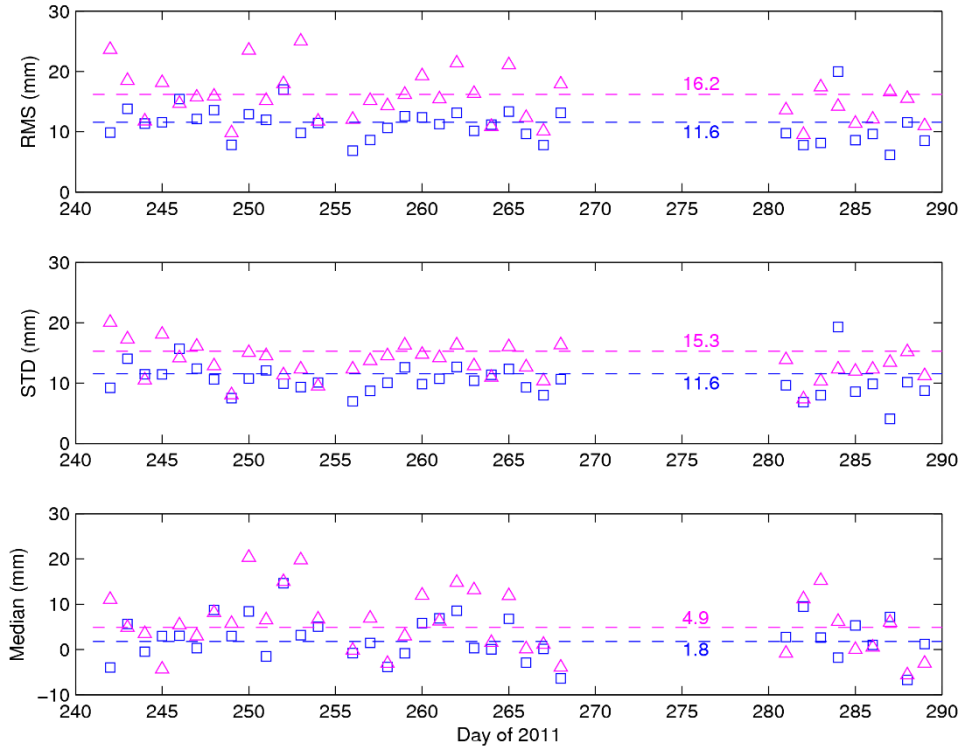


Figure 7-6. Daily RMS, standard deviation, and median of the differences between the interpolated reference ZWD at SNTR, and estimates from a kinematic GPS+GLONASS PPP solution (blue squares) and a kinematic GPS-only PPP solution (magenta triangles). RMS, standard deviation and median values for the entire dataset are represented by dashed lines (GPS+GLONASS, blue; GPS-only, magenta).

To bring further confidence to the statement that a GPS+GLONASS solution should be adopted in kinematic GNSS for ZWD estimation the multi GNSS compatible MagicGNSS kinematic PPP software ZWD estimations were compared to the GIPSY-derived reference values. The web version of MagicGNSS was used with the default process noise and atmospheric settings for the aeronautical mode. GPS+GLONASS, and GPS-only 1 Hz PPP solutions were computed for SNTR for the period day of year 253 - 259. The RMS, standard deviation, and median of ZWD differences for the MagicGNSS kinematic PPP solutions, as well as for PPPNCL solutions over the same period are displayed in Table 7-6.

Table 7-6. RMS, standard deviation and median of the differences between ZWDs estimated from PPPNCL kinematic GPS+GLONASS PPP, PPPNCL kinematic GPS-only PPP, MagicGNSS kinematic GPS+GLONASS PPP (with default atmospheric noise), MagicGNSS kinematic GPS-only PPP (with default atmospheric noise) and the interpolated GIPSY-derived reference values for SNTR for DOY 253 - 259 2011. All quantities are expressed in mm.

| | SNTR | | |
|---|---|---|---|
| | RMS | STD | Median |
| PPPNCL kinematic GPS+GLONASS PPP | 10.6 | 10.7 | 0.8 |
| PPPNCL kinematic GPS-only PPP | 16.1 | 15.1 | 4.6 |
| MagicGNSS kinematic GPS+GLONASS PPP | 14.2 | 13.6 | -3.6 |
| MagicGNSS kinematic GPS-only PPP | 18.4 | 17.4 | -4.9 |

The MagicGNSS kinematic GPS+GLONASS PPP solutions show an improvement over the GPS-only PPP solution from the same software, with smaller RMS, standard deviation and median values seen. The extent of the improvement in the RMS of 4.2 mm is similar to the improvement seen in the PPPNCL solutions of 5.5 mm over the same 6 day period. Due to the lack of processing options available to set in MagicGNSS, the PPP solutions could not be tuned, as they can for PPPNCL. Therefore comparisons between these softwares were not further investigated but an improvement from a kinematic GPS+GLONASS PPP solution over a kinematic GPS-only PPP solution was clearly demonstrated and confirmed in separate software packages.

## 7.4. Conclusion

Over a 50-day period, multiple ZWD estimation techniques using kinematic GNSS on a moving platform undergoing nearly 1 km of height change per trajectory were compared and validated using an interpolated reference ZWD derived from static GPS, and a high resolution NWM. The RMS ZWD difference between the NWM and the GIPSY-derived reference ZWD is 10.8 mm, demonstrating the high quality of the high resolution Unified Model, and its value as a control in the experiment. Improvements in kinematic GNSS have also been shown, with the kinematic GPS+GLONASS PPP solution showing an RMS agreement in ZWD of 11.6 mm compared to 16.2 mm for the kinematic GPS-only PPP solution, with respect to the reference ZWD values.

Kinematic GPS+GLONASS PPP estimates of ZWD also show similar RMS agreements to short-baseline GPS-only double differencing, with respect to the reference ZWD (within 2.5 mm PWV, 11.6 - 12.1 mm ZWD). Furthermore, when baseline lengths of 40 - 50 km were tested that are more representative of kinematic GNSS for sea and airborne vehicles, the PWV agreement worsened by around 1.0 - 1.5 mm. This clearly illustrates the high quality of absolute GNSS which has other advantages in being applicable globally, without the need for GNSS stations on stable platforms, suggesting that a kinematic GPS+GLONASS PPP solution is a very viable option for collecting PWV data from moving platforms.

A major use of a PWV product derived from kinematic GNSS would be to constrain NWMs. The NWM used in this experiment offered good agreement to the kinematic GNSS solutions and the reference values, but it should be noted that the model is operating in an area with dense meteorological measurements and in a post-processed setting. The impact of assimilating GNSS-derived estimates into NWMs is an ongoing field of study (Gutman *et al.*, 2004; Poli *et al.*, 2007; Macpherson *et al.*, 2008; Bennitt and Jupp, 2012) but has shown the potential to improve weather forecasting. The timeliness requirements for assimilation into operational NWMs would require predicted orbit and clock products to be used as opposed to final products. Comparisons of near real-time ZTD observations to post-processed ZTDs using final orbit and clock products show some degradation in ZTD accuracy (Dousa and Bennitt, 2013), therefore further study is required to assess the quality of ZWD estimates using kinematic GNSS with predicted orbits and clocks. Even so, the availability of PWV measurements based on kinematic GNSS at an accuracy of 2 mm or better could be used to improve predictions from NWM and in the calibration of satellite microwave instruments, with particular advantages in sparsely populated areas that serve as major air/sea transport routes and for very high resolution NWMs in the vicinity of major airports.

The effect of estimating the tropospheric delay on a GNSS solution's height will now be investigated in Chapter 8.

# 8. Effect of tropospheric mitigation strategies on height estimation in kinematic GNSS positioning

Kinematic GNSS positioning allows the geo-referencing of sensors used in airborne mapping and monitoring. The use of LIDAR and photogrammetry in applications such as high resolution terrain modelling for flood modelling, coastal monitoring, glacier/ice sheet profiling and high-way levelling require sub-decimetre height accuracy (Middleton *et al.*, 2013), a similar accuracy to LIDAR range measurements (Liu, 2008). To provide the required accuracies for geo-referencing purposes either double-difference positioning or PPP can be used.

For short baselines (< 10 - 20 km) the double-difference positioning approach can be considered to mitigate the same errors experienced at the two GNSS stations. For airborne platforms that operate at a range of heights, this results in a difference in atmospheric conditions (variation in pressure, temperature, and humidity) with height, and therefore a difference in tropospheric delay at each station. Due to this difference in tropospheric delay experienced at the airborne moving platform, empirical tropospheric models such as those tested in Chapter 6, or parameterisation of the tropospheric delay as shown in Chapter 7, are required so that variations in delay may be mitigated to minimise error in height. For kinematic PPP any error in the prediction of the tropospheric delay will propagate directly into the positional error; its mitigation is therefore crucial to achieve the highest accuracy.

The SMR GNSS data set outlined in Chapter 4 allows tropospheric delay mitigation strategies such as empirical models and tropospheric estimation used in relative and absolute airborne GNSS to be assessed. The numerous repeated trajectories experiencing a range of tropospheric conditions over an altitude range of ~1 km make the experimental design suitable for testing different tropospheric mitigation strategies for kinematic GNSS positioning. Previous studies have lacked a reliable reference trajectory to test height accuracy from a truly kinematic dataset over a

range of heights. The effectiveness of mitigating tropospheric delay will be determined by comparing GNSS positioning solution heights to the reference trajectory as outlined in Chapter 4.

This chapter investigates the height accuracy for relative GNSS positioning using kinematic double-difference positioning with empirical models to mitigate tropospheric delay in section 8.1 and 8.2, and estimating the tropospheric delay in section 8.3. The consequence of empirically modelling and estimating the tropospheric delay on height accuracy in absolute GNSS positioning using kinematic PPP is addressed in section 8.4. The use of GPS-only compared to GPS+GLONASS observations in kinematic PPP are analysed in section 8.5. Finally a comparison between the kinematic GNSS techniques of PPP and double-difference positioning is undertaken in section 8.6.

## 8.1. Kinematic double-difference positioning height accuracy using empirical tropospheric models

Commercial kinematic GNSS positioning software packages capable of supporting airborne GNSS positioning such as Leica Geomatics Office, and Trimble Total Control, do not parameterise tropospheric delay. Instead, they rely on double differencing and empirical models which are functions of latitude, height, and (in more modern models) day of year. The models therefore cannot predict the changes in delay due to the highly variable nature of the troposphere, as was demonstrated in Chapter 6.

Previous studies (e.g. Tiemeyer *et al.,* 1994; Shi and Cannon, 1995) have demonstrated that the bias in height is correlated with the difference in height between GNSS stations in double-difference positioning solutions. The magnitude of the height bias from the use of empirical tropospheric models has also been investigated over a range of heights (e.g. Shan *et al.* (2007), King (2009), Zhao *et al. (*2009)). Shan *et al.* (2007) computed 11 kinematic double-difference positioning solutions relative to 11 different reference stations situated over a 1.4 km altitude range for a ~4 hour flight

in South California and found a 20 cm deviation in height between solutions. The bias in the solution's height (bias computed against the mean trajectory from the 11 solutions) was shown to be linearly correlated to the altitude of the reference stations. A GPS height bias of 0.1 - 0.3 m in mountainous areas (UK and the European Alps) for GNSS stations on stable platforms processed in a kinematic mode was demonstrated by King (2009).

In this thesis a number of empirical tropospheric models, including EGNOS (Collins and Langley, 1997), UNB3m (Leandro *et al.*, 2008), Saastamoinen (Saastamoinen, 1972), and Modified Saastamoinen (i.e. Saastamoinen but inputting pressure and temperature from GPT (Boehm *et al.*, 2007) and GPT2 (Lagler *et al.*, 2013)), were tested. The global mapping function (Boehm *et al.*, 2007) was used with each model (including EGNOS and UNB3m which have their own mapping function); therefore the ability of the models to account for the zenith delay can be assessed, resulting from their ability to account for the meteorological parameters of temperature, pressure, and relative humidity. The empirical tropospheric models were described and tested against reference pressure, temperature, and delay values at the GNSS stations on stable and moving platforms for the SMR site in Chapter 6. The models were chosen due to their use in commercial kinematic GNSS processing software aimed at airborne GNSS positioning. Relative GPS solutions were computed with Track, version 1.24, at a one second interval, for each of the empirical tropospheric models. IGS final orbits were held fixed and a positional process noise of 4 m $s^{-0.5}$ was applied. The kinematic double-difference positioning solutions were processed with respect to SNLB rather than SNSU to create a scenario similar to airborne GNSS positioning whereby the reference station is at a lower altitude than the airborne GNSS receiver. The Track software was modified to include the EGNOS, UNB3m, and GPT2 models, with orthometric heights (rather than ellipsoidal) used with each model. The empirical models that do not predict the separation between the geoid and ellipsoidal heights corrected the ellipsoidal height input by manually applying an offset of ~55 m. The default value of relative humidity in the GMF was altered from 0 to 0.5, similar to an update available in Track version 1.27. The assessment of each model during a range

of tropospheric conditions was enabled by the dataset including samples over a 50 day period.

The tropospheric delay is most prevalent in the height component, with the delay amplifying by up to a factor of three into the height error (Santerre, 1991). The height component will therefore be the focus in determining the extent of the tropospheric mitigation. The RMS, standard deviation, median, and mean of the height differences between the reference trajectory and the relative GPS solutions using a range of empirical tropospheric models are displayed in Table 8-1. Values are compared between the heights of 255 - 1120 m to exclude occasions when SNTR is stationary at the summit station, and to exclude sections through the wooded section of railway around the Llanberis station where the accuracy of the solutions' and the reference trajectory are degraded. The performance of the tropospheric models in the height component of SNTR corresponds to the performance of the models in predicting the ZTD as shown in Chapter 6. The EGNOS model has the smallest RMS in the differences in ZTD and height, followed by UNB3m in both cases.

Table 8-1. RMS, standard deviation and median of the differences in height between kinematic GPS-only double-difference positioning solutions using a variety of empirical tropospheric delay models and the spline generated reference trajectory for SNTR between the ellipsoidal heights 255 - 1120m. All quantities expressed in millimetres.

| | SNTR | | | |
|---|---|---|---|---|
| | RMS | STD | Median | Mean |
| EGNOS | 61 | 61 | -1 | -4 |
| UNB3m | 71 | 68 | -12 | -21 |
| Saastamoinen | 79 | 71 | -26 | -36 |
| SAAST(GPT) | 89 | 76 | -37 | -48 |
| SAAST(GPT2) | 133 | 107 | -60 | -79 |

Due to the error in height being correlated with the difference in height between two GNSS stations, the height differences from the empirical models were analysed in 100 m height bins. It can be seen in Figure 8-1 that the mean and median biases

increase with height for each model. The extent that the error increases for each model is not consistent though, with the Saastamoinen with GPT input model having a mean height accuracy of -35 mm at 300 - 400 m and -72 mm at 1000 - 1100 m, compared to -15 mm and 5 mm using the EGNOS model respectively. The increase in error with height from the Saastamoinen with GPT input model compared to the EGNOS model is a consequence of misrepresenting the lapse rates of temperature and pressure fields in the GPT model.

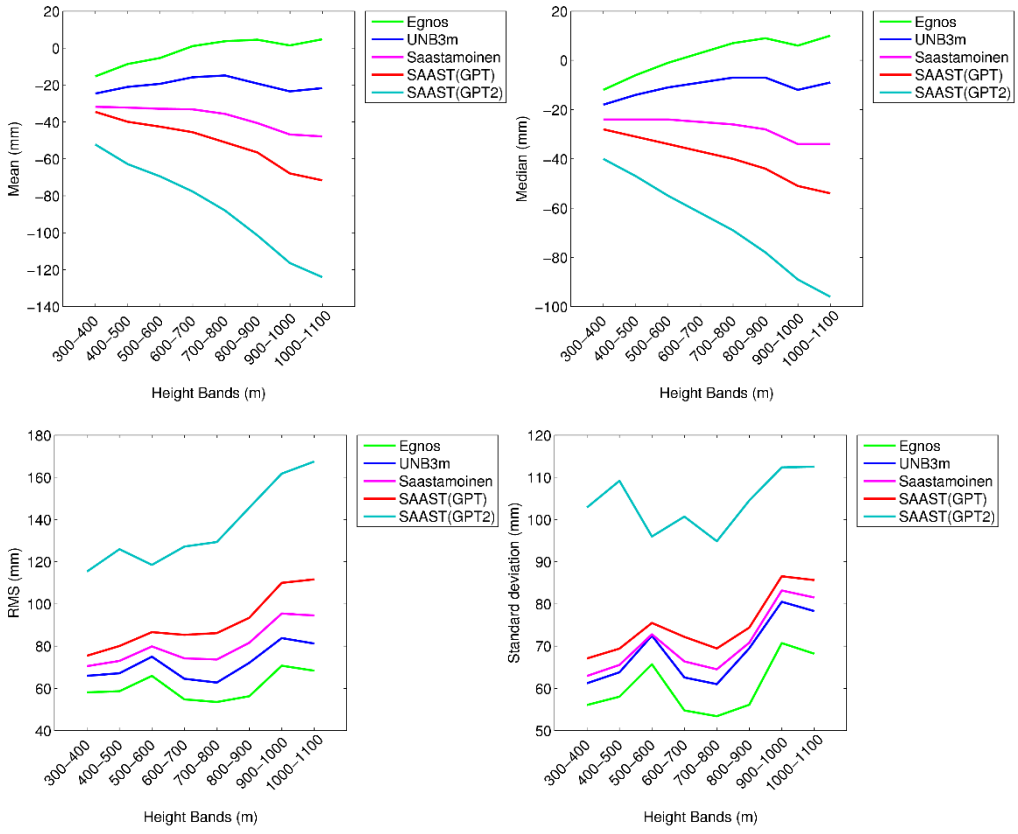


Figure 8-1. Mean (upper left pane), median (upper right pane), RMS (lower left pane), and standard deviation (lower right pane) of height accuracy (in 100 m ellipsoidal height bins) between the reference trajectory and kinematic GPS-only double-difference positioning solutions using a range of standard empirical tropospheric models for SNTR.

In Chapter 6 the UNB3m model was seen to have the smallest median bias compared to the reference tropospheric delay values. Here, the EGNOS model is shown to provide the best height accuracy with the smallest median bias. The difference

between the optimal model for representing the tropospheric delay and coordinate accuracy is a consequence of double differencing over such a short baseline. The double differencing results in the lapse rate of the model being the defining feature. The median ZTD difference between SNLB and SNTR from the GIPSY-derived reference values and from the empirical tropospheric models are displayed in Figure 8-2, with the median ZTD differences over the height range showing the same trend as the median height accuracy in Figure 8-1.

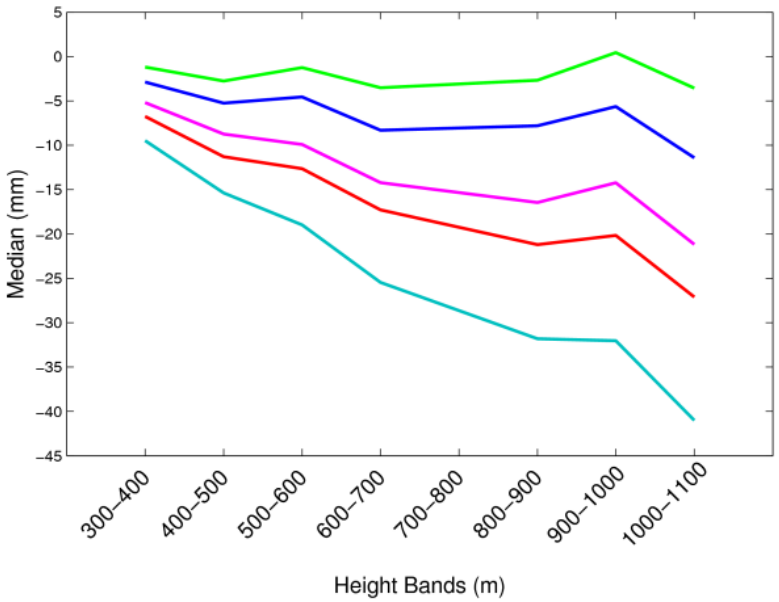


Figure 8-2 ZTD median differences at SNTR between the GIPSY-derived reference values and the EGNOS (green), UNB3m (blue), Saastamoinen (magneta), Saastamoinen with GPT input (red), Saastamoinen with GPT2 input (turquoise) empirical tropospheric models in 100 m height bands.

The baseline between SNLB and SNTR does not exceed 6 km, whereas in most airborne GNSS positioning scenarios the baseline length will be greater than this. SNTR was therefore processed relative to ASAP, the nearest OS CGNSS station to the SMR with a baseline of ~45 km (the locations and distances of the nearest sites are detailed in Chapter 4 and can be considered typical for the UK). SNTR was processed relative to ASAP with the UNB3m tropospheric model and using the same settings and process noise values as used for the solutions relative to SNLB. For the longer baseline solution, the RMS and standard deviation for height accuracy are 233 mm and 232 mm respectively over height differences of 255 – 1120 m, around three times higher than

the solution with UNB3m model over a short baseline. The effect on height over a longer baseline compared to a shorter baseline is evident in the mean, median, RMS, and standard deviations of the height accuracy in 100 m height bands as displayed in Figure 8-3.

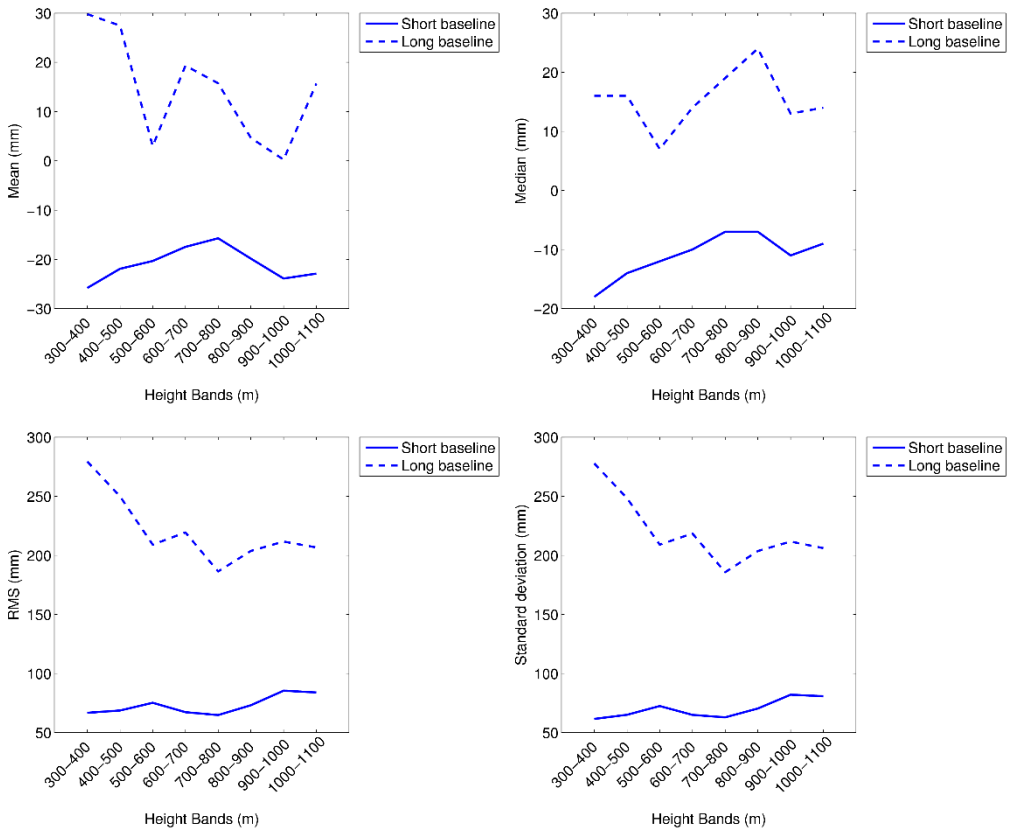


Figure 8-3. Mean (upper left pane), median (upper right pane), RMS (lower left pane), and standard deviation (lower right pane) of height accuracy (in 100 m ellipsoidal height bins) between the reference trajectory and kinematic GPS-only double-difference positioning solutions using the UNB3m empirical tropospheric model for a short and long baseline to SNTR.

## 8.2. Relationship between ZWD lapse rate and height accuracy

The effect of the difference in ZWD between a GNSS station on a stable platform (in this case SNLB) and another GNSS station on a stable platform (SNSU) using empirical tropospheric models was investigated following on from Section 6.4, where variations in the ZWD lapse rate were seen to affect the performance of the models. To establish whether the effect of a change in tropospheric conditions between one station and

another could be detected, a kinematic double-difference positioning solution using the Saastamoinen tropospheric model with input temperature and pressure from GPT (using the same Track settings used in Section 8.1) was computed for SNSU relative to SNLB. The processed baseline offers the largest height difference over the test site, meaning the residual signal should be at a maximum, and the use of GNSS stations on stable platforms means that the solution should be less noisy. The resulting height estimates from Track were compared with the GIPSY-derived coordinates for SNSU, with 15 min samples of differences plotted in Figure 8-4. The ZWD difference between SNLB and SNSU are also shown, with a smoothed line of best fit from using the Matlab 'rloess' smoother function (a local regression weighted 2$^{nd}$ degree polynomial model, with data outside six mean absolute deviations given a zero weighting) fitted through the height differences. It can be seen that the smoothed fit through the height differences corresponds to the trend of the ZWD difference, with an increase in the height difference around day of year 252 (corresponding to the larger ZWD difference) and a decrease in the height difference around day of year 280, when the smallest lapse rate between SNLB and SNSU occurs.

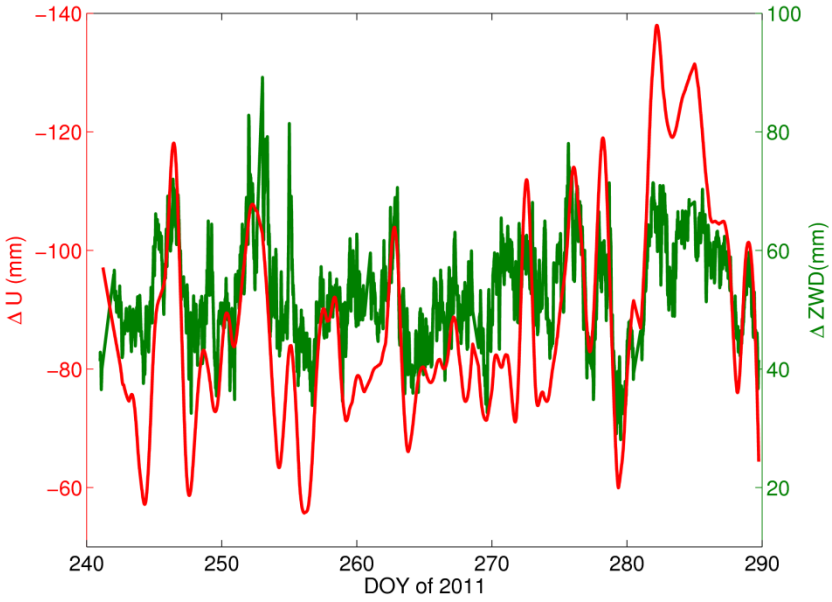


Figure 8-4. Smoothed height accuracy (inverted left axis) from a kinematic GPS-only double-difference positioning solution using the Saastamoinen with GPT input model and GMF mapping function (red). The GIPSY-derived reference ZWD difference between SNLB and SNSU is included (green).

8. Effect of tropospheric mitigation strategies on height estimation in kinematic GNSS positioning

To investigate the effect of variations in the ZWD lapse rate on SNTR the median height accuracy (biases) per trajectory (between ellipsoidal heights 250m - 1120 m) for the atmospheric models UNB3m and Saastamoinen with GPT for day of year 250 to 255 were examined, and are shown in Figure 8-5. The difference in the GIPSY-derived reference ZWD values between the SNLB and SNSU are also included due to unmitigated tropospheric delay mapping three fold into a height error. The difference in height (left) axis has been inverted to highlight the effect that a change in tropospheric conditions can have on the height accuracy (an underestimation of the amount of delay will result in a negative bias). The span day of year 250 - 255 was chosen due to the largest difference in ZWD between SNLB and SNSU occurring during this 5 day period.

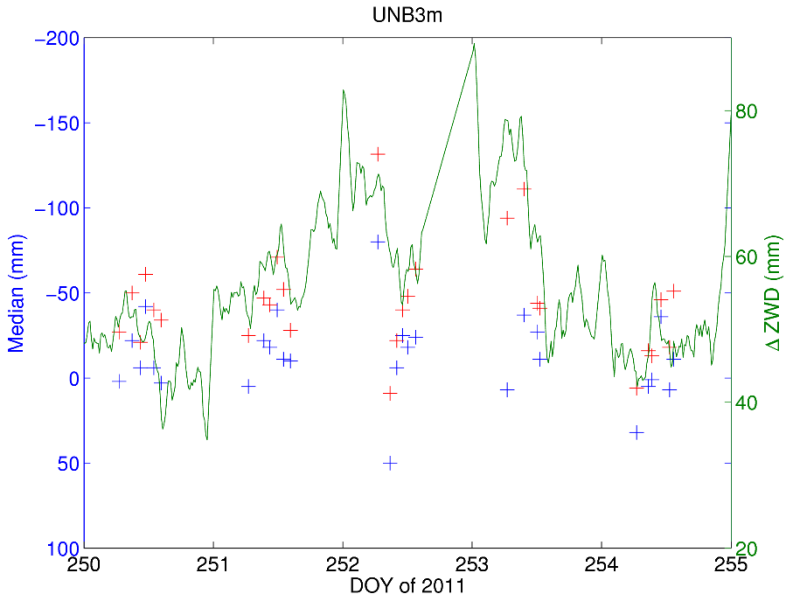


Figure 8-5. Median height accuracy between reference trajectory and kinematic GPS-only double-difference positioning solutions using the UNB3m tropospheric model (blue), and Saastamoinen with GPT input model (red). The GIPSY-derived differences in ZWD between SNLB and SNSU are included in green.

To highlight the effect of the variation of the ZWD lapse rate on height quality the mean height accuracies were plotted against ZWD differences (SNLB - SNSU) for different height bands. To demonstrate the effect only the highest 100 m height band of 1000 - 1100 m from SNLB, where the residual delay is at its maximum, is shown in Figure 8-6.

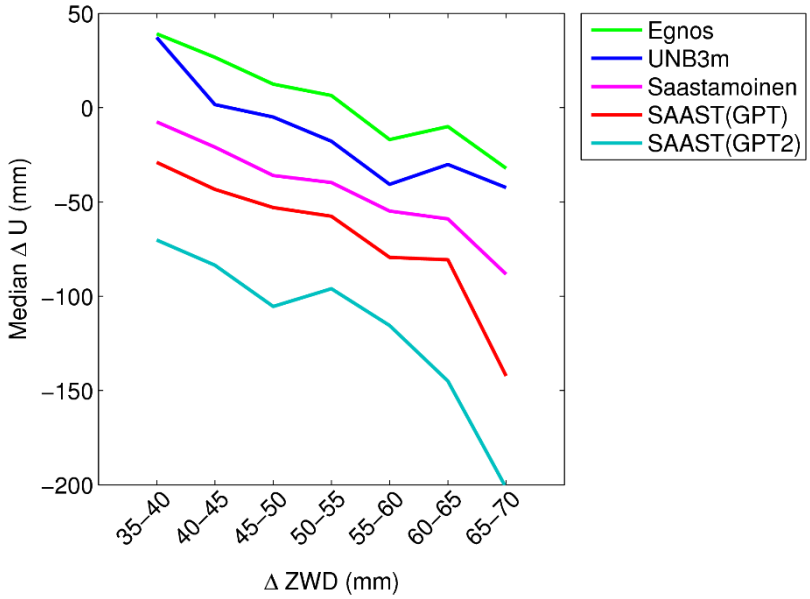


Figure 8-6. Median height accuracies (in 5 mm ZWD bins) between the reference trajectory and kinematic GPS-only double-difference positioning solutions using a range of empirical tropospheric models for SNTR when between ellipsoidal heights of 1000 - 1100 m.

At the height band of 1000 - 1100 m a negative trend is seen for each model, and the greater the difference in ZWD between SNLB and SNSU, the greater the error in height. There is more than a 50 mm variation in the height difference between ZWD differences at 35 - 40 mm compared to 65 - 70 mm for each model. The increasing negative trend would suggest that the lapse rate used in each model under represents the mean lapse rate of 53 mm/950 m for the tropospheric conditions experienced during the data collection.

## 8.3. Effect of parameterising tropospheric delay on kinematic double-difference positioning height accuracy

In the previous sections (8.1 and 8.2) the limitations of empirical models to predict high temporal variations of ZTD were highlighted. To mitigate the error in height caused by residual tropospheric delay in airborne GNSS positioning there are two options, to use multiple base stations to interpolate or extrapolate the delay, or to parameterise the residual delay and estimate its magnitude. The method outlined in Shan *et al.* (2007) uses the external calibration technique, involving calibrating the

expected zenith delay and its lapse rate from the analysis of ground-based GNSS stations on stable platforms over a range of heights. A limitation of the external calibration technique is that it relies on the presence of suitable topography, and the availability of such GNSS stations at a range of heights. A more practical and applicable solution for airborne GNSS positioning is the direct estimation of delay parameters as part of the solution, similar to the approach used in static GNSS positioning (e.g. Dodson *et al.,* 1996).

To initially test the effect of parameterising the ZWD, kinematic double-difference positioning solutions were computed for SNSU relative to SNLB first using an empirical tropospheric model (Saastamoinen with GPT input) and secondly estimating the tropospheric delay. The resulting coordinates from estimating the tropospheric delay, and modelling the tropospheric delay with the Saastamoinen with GPT input model, were subtracted from the GIPSY-derived coordinates for SNSU, and the differences in height are displayed in Figure 8-7. The resulting RMS, standard deviation, median and mean of the differences are shown in Table 8-2. It is evident that parameterising the ZWD improves the solution, with the RMS of the height difference reducing from 97 mm to 28 mm, and the median height bias from misrepresenting the delay reducing from -87 mm to -7 mm. The standard deviation of the height difference has also reduced, suggesting that the short term variations in the ZWD are better represented with parameterisation.

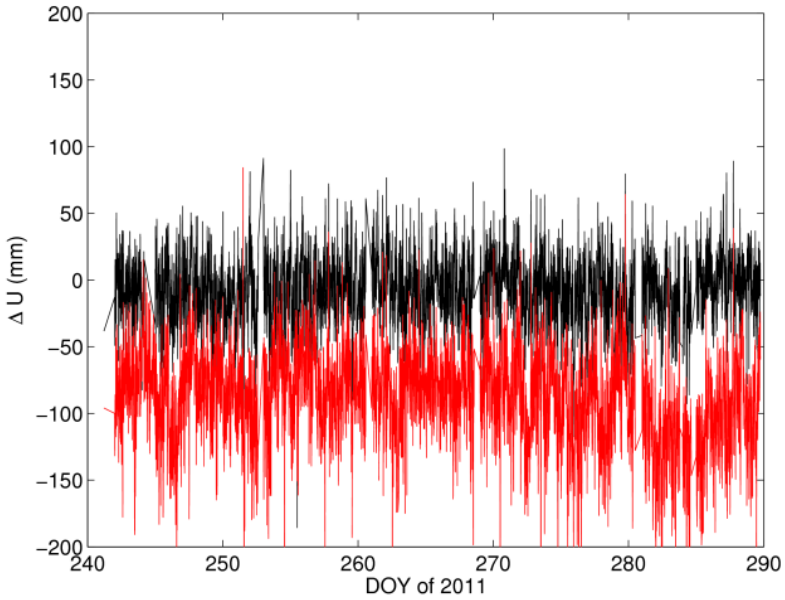


Figure 8-7. Differences in height at SNSU (1065 m above mean sea level) between GIPSY-derived reference coordinates and kinematic GPS-only double-difference positioning solutions relative to SNLB (115 m above mean sea level) using the Saastamoinen with GPT input model and GMF mapping function (red), and using the same model but with estimating the residual delay (black), sampled at 15 minute interval.

Table 8-2. RMS, standard deviation, median, and mean of differences in height for SNSU between GIPSY-derived reference coordinates and kinematic GPS-only double-difference positioning solutions (against SNLB) using the Saastamoinen with GPT input model, and using the same model but with estimation of the residual delay. All quantities expressed in millimetres.

| | SNSU | | | |
|---|---|---|---|---|
| | RMS | STD | Median | Mean |
| SAAST(GPT) | 97 | 37 | -87 | -5 |
| SAAST(GPT) with est. | 28 | 27 | -7 | -8 |

To further investigate the effect of parameterising the ZWD a smoother was fitted through the 15 minute sampled data using the Matlab 'rloess' smoother function ; and is shown in Figure 8-8 alongside the difference in ZWD between SNSU and SNLB. It can be seen that the parameterised ZWD solution magnitude is smaller, and the trend in the difference does not match the ZWD difference between SNSU and SNLB as is the case when only the tropospheric model is used.

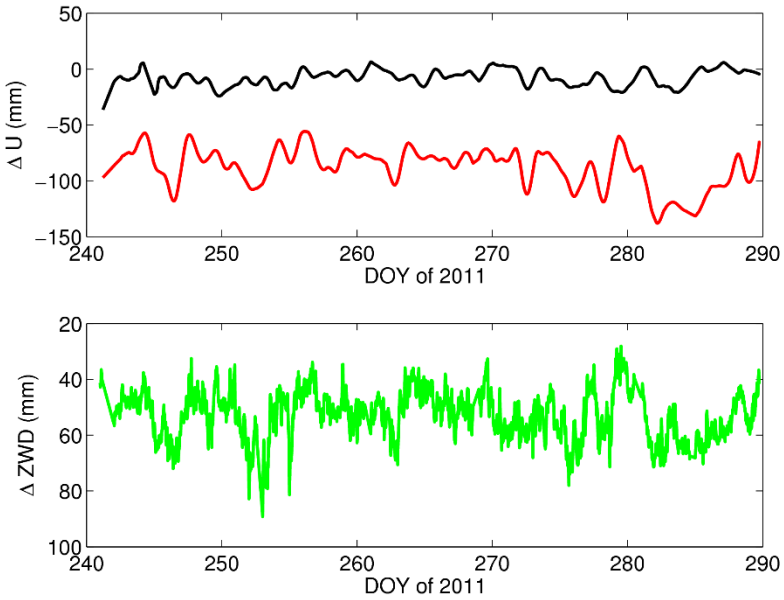


Figure 8-8. Smoothed height differences (top pane) at SNSU from kinematic GPS-only double-difference positioning solutions using the Saastamoinen with GPT input model (red), and using the same model but with estimating the residual delay (black), compared to the GIPSY-derived reference coordinates. The difference in ZWD between SNLB and SNSU are included in the lower pane (inverted left axis).

The parameterised ZWD solutions were tested on SNTR using the same method as in Chapter 8.1, with the results between heights of 255 - 1120 m displayed in Table 8-3. There is an improvement from the solution parameterising ZWD when compared to using only an empirical tropospheric model, with a median bias of -5 mm compared to -37 mm.

Table 8-3. RMS, standard deviation, median, and mean of the differences in height between kinematic GPS-only double-difference positioning solutions (with respect to SNLB) using the Saastamoinen with GPT input model and using the same model but estimating the residual delay, and the spline generated reference trajectory for SNTR between the ellipsoidal height 255 - 1120 m. All quantitities expressed in millimetres.

| | SNTR | | | |
|---|---|---|---|---|
| | RMS | STD | Median | Mean |
| SAAST(GPT) | 89 | 76 | -37 | -48 |
| SAAST(GPT) with est. | 72 | 71 | -5 | -4 |

8. Effect of tropospheric mitigation strategies on height estimation in kinematic GNSS positioning

In the kinematic GPS-only double-difference positioning solutions without parameterising the ZWD, as the difference in height between the two GNSS stations increases so does the error in height, a consequence of different conditions at each site and therefore unmitigated residual delay in the double-difference solution. The mean height accuracy for 100 m height sections were plotted (Figure 8-9) between 300 and 1100 m for the solution estimating ZWD, and for a solution only using the Saastamoinen with GPT input model. The solution estimating ZWD does not degrade with height, but the solutions with Saastamoinen with GPT input model does. Histograms of the difference in height between the height bands 1000 - 1100 m are included in Figure 8-10 and demonstrate the bias that is introduced with the increase in height separation.

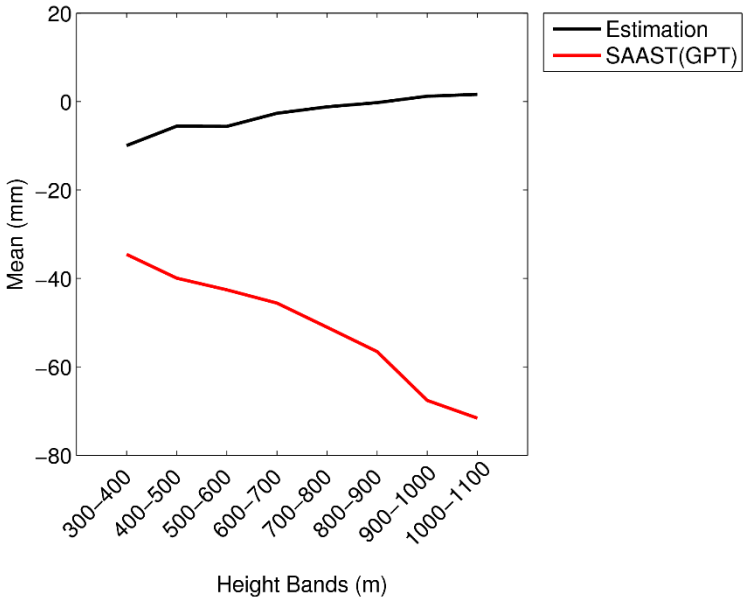


Figure 8-9. Mean height accuracy (in 100 m ellipsoidal height bins) between the reference trajectory and the kinematic GPS-only double-difference positioning solutions estimating the residual tropospheric delay (black) and using the Saastamoinen with GPT input model (red) for SNTR.

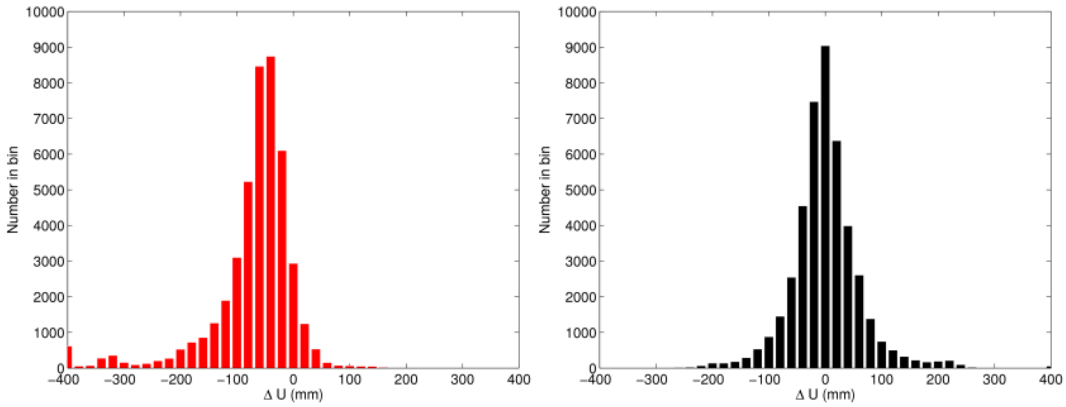


Figure 8-10. Histograms of height accuracy at SNTR for a height range of 1000 - 1100 m between the reference trajectory and kinematic GPS-only double-difference positioning solutions using the empirical tropospheric models of Saastamoinen with GPT input (left pane), and estimating the residual tropospheric delay (right pane). Each bin size represents 20 mm of height difference.

The increase in the height error with the increase of the ZWD lapse rate experienced by each of the empirical tropospheric models, as demonstrated in Figure 8-6, is overcome by parameterising the tropospheric delay. Figure 8-11 shows the median error in height plotted against the ZWD difference between SNLB and SNSU for the height range 1000 - 1100 m for the Saastamoinen model with GPT input, with and without parameterisation. When there is a larger variation in conditions between the two GNSS stations the error increases, whereas parameterising the delay mitigates the error for a variety of atmospheric conditions.

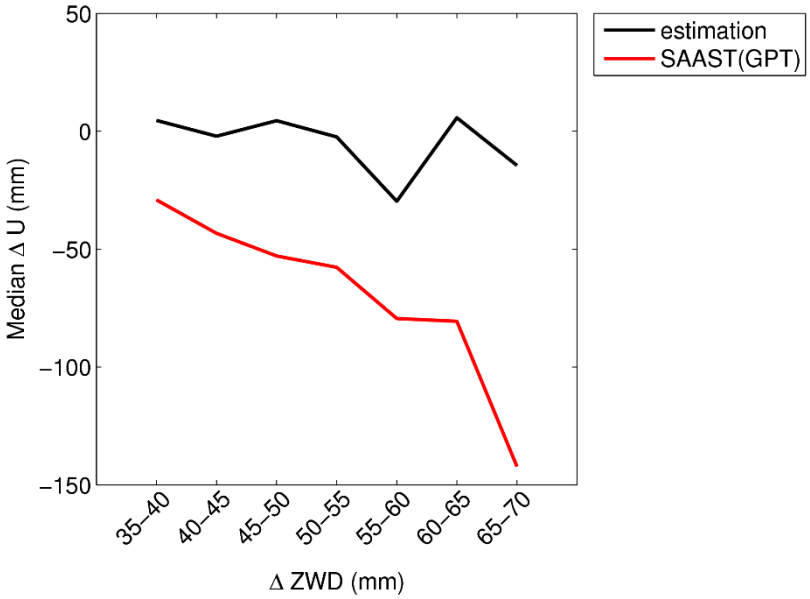


Figure 8-11. Median height accuracy (in 5 mm ZWD difference bins between SNLB and SNSU) between the reference trajectory and kinematic GPS-only double-difference positioning solutions estimating the residual tropospheric delay (black) and using the Saastamoinen with GPT input model (red) for SNTR when between ellipsoidal heights of 1000 - 1100 m.

## 8.4. Effect of parameterising tropospheric delay on kinematic PPP height accuracy

Kinematic PPP operates independently of a reference station, so observations cannot be differenced to remove error sources, which therefore must be modelled or parameterised. Any error in the mitigation of the tropospheric delay therefore maps directly into a height error. The performance of estimating the tropospheric delay compared to mitigating the tropospheric delay with an empirical tropospheric model is first assessed at the GNSS stations on stable platforms (SNLB and SNSU). The PPPNCL kinematic PPP software was used with GPS+GLONASS observations and the same process noise and configuration settings as used in Chapter 7 for the solution estimating the tropospheric delay, with the same settings also used for the empirical tropospheric model solution, except the tropospheric process noise was set to zero leaving only the Saastamoinen with GPT input model to mitigate the tropospheric delay. The differences in height between the PPPNCL kinematic GPS+GLONASS PPP solutions and the GIPSY-derived reference coordinates for SNLB and SNSU are displayed in Figure 8-12.

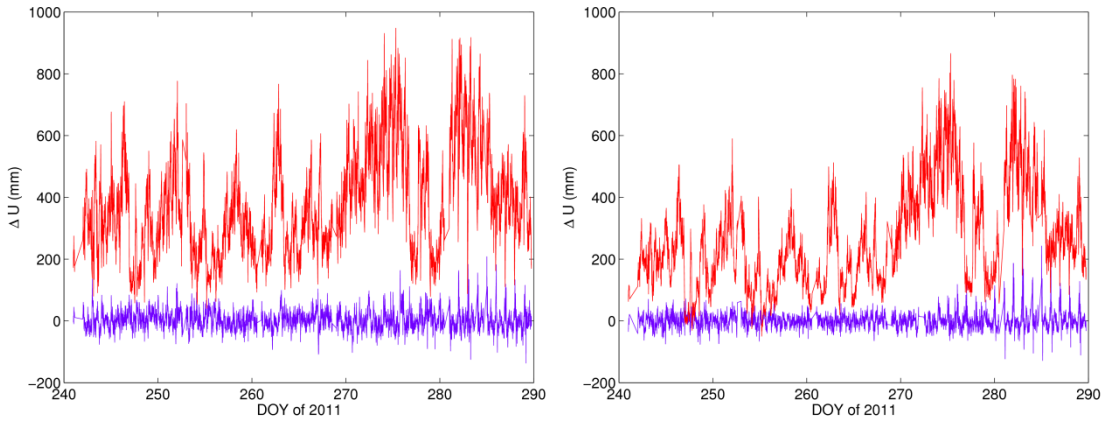


Figure 8-12. Height difference at SNLB (left pane) and SNSU (right pane) for a kinematic GPS+GLONASS PPP solution when using the Saastamoinen tropospheric model with GPT input and GMF mapping function (red), and using the same model but with estimating the residual tropospheric delay (purple), sampled at 15 minute interval.

The improvement in estimating the residual tropospheric delay compared with only using an empirical tropospheric model is clear, as an obvious bias arises when using the empirical tropospheric model resulting in up to 0.8 m variation of the error in height. The magnitude of the error is greater at SNLB compared with SNSU as can be seen in the RMS, standard deviation, median and mean differences detailed in Table 8-4. The larger bias at SNLB is due to the lower altitude of the site and the greater amount of tropospheric delay experienced at the site.

Table 8-4. RMS, standard deviation and median of the differences in, Easting, Northing and height between a kinematic GPS+GLONASS PPP solution using the Saastamoinen with GPT input model, and estimation of residual tropospheric delay, compared to the GIPSY-derived reference height for SNLB and SNSU. All quantitities expressed in millimetres.

| | SNLB | | | | SNSU | | | |
|---|---|---|---|---|---|---|---|---|
| | RMS | STD | Median | Mean | RMS | STD | Median | Mean |
| model E | 46 | 45 | 8 | 9 | 33 | 33 | 2 | 4 |
| estimated E | 16 | 15 | -4 | -6 | 15 | 14 | -4 | -5 |
| model N | 52 | 52 | -2 | 0 | 37 | 37 | -2 | 0 |
| estimated N | 13 | 13 | 3 | 2 | 14 | 14 | 1 | 2 |
| model U | 412 | 164 | 354 | 378 | 304 | 158 | 228 | 259 |
| estimated U | 34 | 34 | 0 | 1 | 30 | 30 | -1 | 0 |

The coordinate accuracy of the kinematic GPS+GLONASS PPP solutions were then tested at SNTR through comparison to the reference trajectory. The RMS, standard deviation, median, and mean differences in height over a height range of 255 - 1120 m are displayed in Table 8-5. The height errors with respect to the reference trajectory are larger from the GNSS station on a moving platform, compared to the GNSS stations on stable platforms when estimating the residual tropospheric delay, a result of the increase in noise introduced from the dynamics experienced by the receiver. Whereas, the RMS, standard deviation, median and mean height accuracies from the empirical model solution for SNTR are of a similar magnitude to the values experienced at SNLB and SNSU. The limitation of mitigating the tropospheric delay with only an empirical model over a range of heights is evident in Figure 8-13, with any change in the statistics due to the receivers' height negligible compared to the magnitude of the statistics.

Table 8-5. RMS, standard deviation and median of the differences in height between kinematic GPS+GLONASS PPP solutions using the Saastamoinen with GPT input model and estimating residual tropospheric delay, with respect to the reference trajectory for SNTR between the ellipsoidal height 255 - 1120 m. All quantitities expressed in millimetres.

| | SNTR | | | |
|---|---|---|---|---|
| | RMS | STD | Median | Mean |
| PPPNCL model only | 331 | 157 | 261 | 291 |
| PPPNCL model + est | 78 | 72 | 24 | 29 |

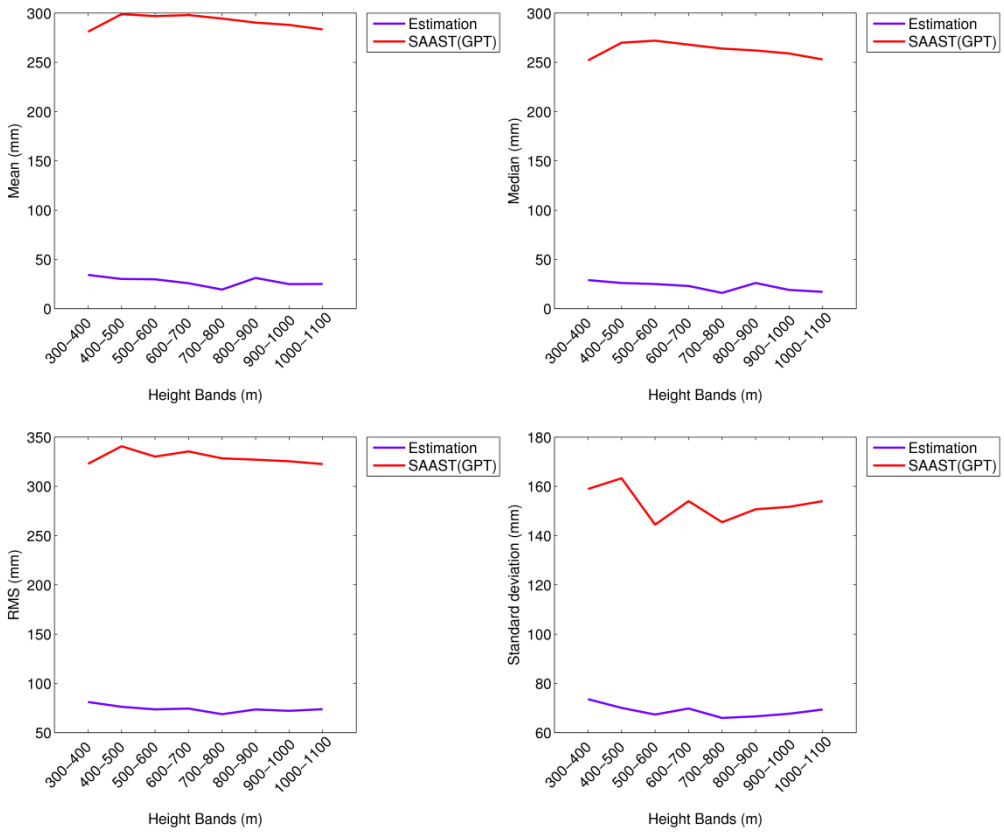


Figure 8-13. Mean (upper left pane), median (upper right pane), RMS (lower left pane), and standard deviation (lower right pane) of height accuracy (in 100 m ellipsoidal height bins) between the reference trajectory and kinematic GPS+GLONASS PPP solutions using the Saastamoinen GPT input model and with parameterisation of tropospheric delay for SNTR.

The error in height is correlated with the increase in ZWD for the solution using only the empirical tropospheric model, as can be seen from Figure 8-14. The median error between the heights of 1000 - 1100m increases from 0.137 m when the ZWD is between 20 - 40 mm, to 0.517 m when between 160 - 180 mm. When the tropospheric

delay is parameterised in the kinematic GPS+GLONASS PPP solution the variation in the error with height over a range of ZWD conditions is between 3 mm at 20 - 40mm ZWD to 20 mm between 160 - 180 mm ZWD.

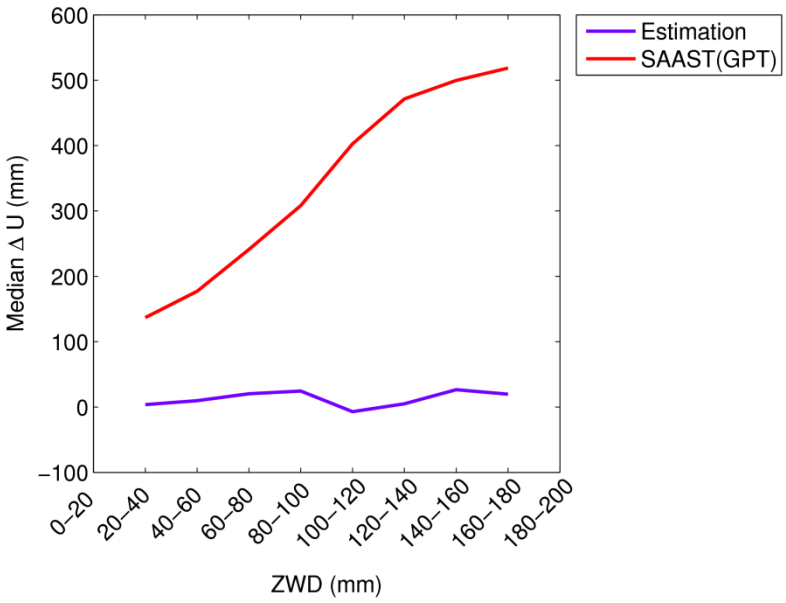


Figure 8-14. Median height accuracy (in 20 mm ZWD bins) between the reference trajectory and kinematic GPS+GLONASS PPP solutions estimating the atmospheric delay (purple), and using the Saastamoinen with GPT input model (red) for SNTR when between ellipsoidal heights of 1000 - 1100 m.

## 8.5. Effect of multiple GNSS on kinematic PPP height accuracy

The use of multiple GNSS (GPS+GLONASS) and GPS-only observations in kinematic PPP is assessed in terms of height accuracy in this section, following on from the comparison for estimating tropospheric delay in Chapter 7. The use of multiple GNSSs increases the availability of observations, and provides the potential to improve positional accuracy. Previous studies (Martin, 2013) did not see a significant improvement with the inclusion of GLONASS for converged solutions, though these were tested at IGS stations with near-ideal open sky views. Cai and Gao (2013) found an improvement in kinematic GNSS solutions tested at GNSS stations on stable platforms with the inclusion of GLONASS observations, when the geometry of the GPS distribution is poor and when the number of visible GPS satellites is low. A 25% improvement in the accuracy of height component has also been demonstrated by

Choy *et al.* (2013) from a kinematic GPS+GLONASS solution compared to a GPS-only solution for an aircraft dataset when compared to a kinematic double-difference positioning solution, with the improvement increasing to 49% with limited satellite availability (by increasing the elevation cut off angle from 5 °to 15°).

The kinematic PPP solutions were initially tested at SNLB and SNSU and compared with the reference coordinates generated from GIPSY as described in Chapter 4, with the resulting statistics displayed in Table 8-6. The kinematic GPS+GLONASS PPP solution has a smaller average RMS and standard deviation at the two stations of 32 mm compared to the kinematic GPS-only PPP solution average RMS and standard deviation of 38 mm. The average mean and median differences for SNLB and SNSU are greater for the kinematic GPS-only PPP solution: -6 and -5 mm compared to -1 and 1 mm respectively. The performance of kinematic PPP at these GNSS stations on stable platforms provides a benchmark of the available accuracy. A standard deviation of 3 cm to 4 cm for the precision of height for a kinematic PPP solution is of similar in magnitude to previous work (Martin, 2013) with PPPNCL, and alternative PPP software packages such as NRCan as tested in Choy *et al.* (2013).

Table 8-6. RMS, standard deviation, median, and mean of the differences in height between PPPNCL kinematic GPS-only and GPS+GLONASS PPP solutions, and GIPSY-derived reference height for SNLB and SNSU. All quantitities expressed in millimetres.

| | SNLB | | | | SNSU | | | |
|---|---|---|---|---|---|---|---|---|
| | RMS | STD | Median | Mean | RMS | STD | Median | Mean |
| GPS+GLONASS | 34 | 34 | 0 | 1 | 30 | 30 | -1 | 0 |
| GPS-only | 42 | 42 | -4 | -3 | 34 | 34 | -7 | -6 |

To further test the performance of kinematic GPS+GLONASS and GPS-only PPP, solutions were computed for the GNSS station on a moving platform (SNTR), and assessed against the reference trajectory. The RMS, standard deviation, median, and mean differences in height over a height range of 255 - 1120 m from the kinematic GPS+GLONASS and GPS-only PPP solutions are displayed in Table 8-7. Over the ellipsoidal height range of 255 - 1120 m the kinematic GPS+GLONASS PPP solution

provides an RMS of 78 mm, an improvement of 51 mm on the kinematic GPS-only PPP solution. The median and mean differences are smaller for the kinematic GPS-only PPP solution over the 865 m height range. When the accuracies for the two solutions are compared over a range of heights, as displayed in Figure 8-15 a height dependence is evident in the mean and median of the 100 m height bands from the kinematic GPS-only PPP solution. The mean from the kinematic GPS-only PPP solution varies by 45 mm, from 7 mm at 300 - 400 m to -38 mm at 1000 - 1100 m. The mean and median differences in height from the GPS+GLONASS solution vary less over the height range.

Table 8-7. RMS, standard deviation and median of the differences in height between PPPNCL kinematic PPP solutions using GPS+GLONASS and GPS-only and the reference trajectory for SNTR between the ellipsoidal heights of 255 - 1120 m. All quantitities expressed in millimetres.

| | SNTR | | | |
|---|---|---|---|---|
| | RMS | STD | Median | Mean |
| GPS-only | 129 | 128 | -10 | -13 |
| GPS+GLONASS | 78 | 72 | 24 | 29 |

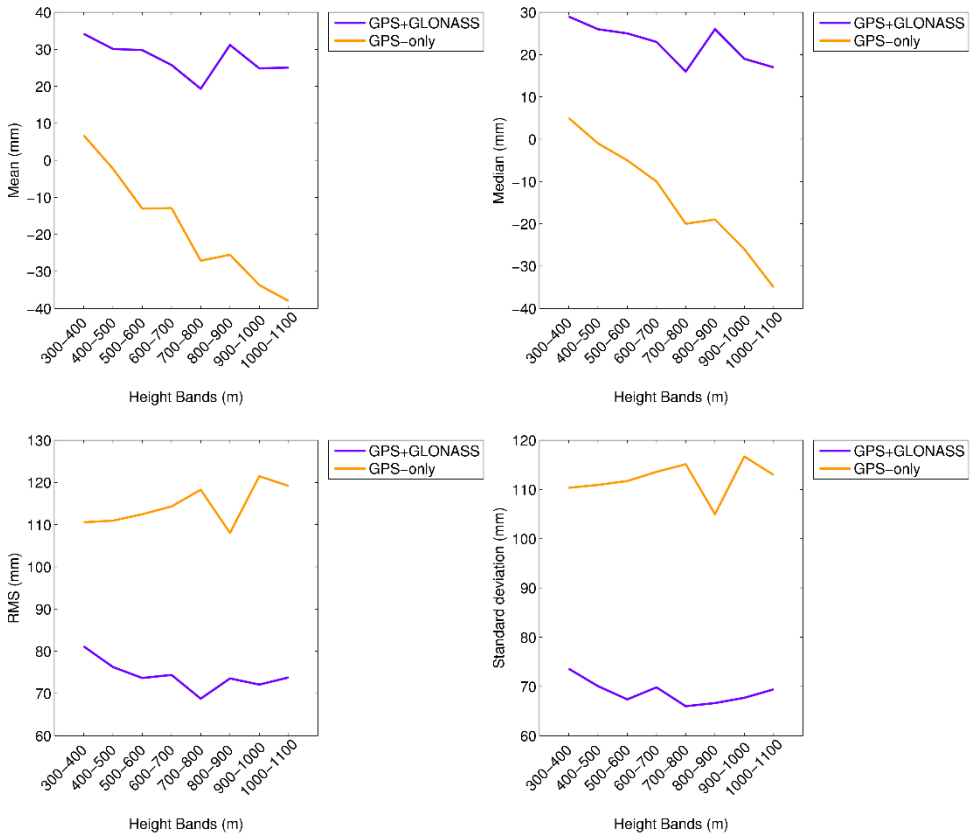


Figure 8-15. Mean (upper left pane), median (upper right pane), RMS (lower left pane), and standard deviation (lower right pane) of height accuracy (in 100 m ellipsoidal height bins) between the reference trajectory and PPPNCL kinematic PPP solutions using GPS+GLONASS and GPS-only for SNTR.

The distribution of the height accuracy from the PPPNCL kinematic GPS+GLONASS and GPS-only solutions for heights of 300 - 400 m and 1000 - 1100m are shown in the histograms of Figure 8-16 and Figure 8-17. It is evident that the kinematic GPS+GLONASS PPP solution provides a higher precision than a kinematic GPS-only PPP solution, with a reduction of 56% in the standard deviation. The kinematic GPS+GLONASS PPP solution provides a more consistent mean height accuracy of ~30 mm, while there is a height dependent bias in the kinematic GPS-only PPP solution.

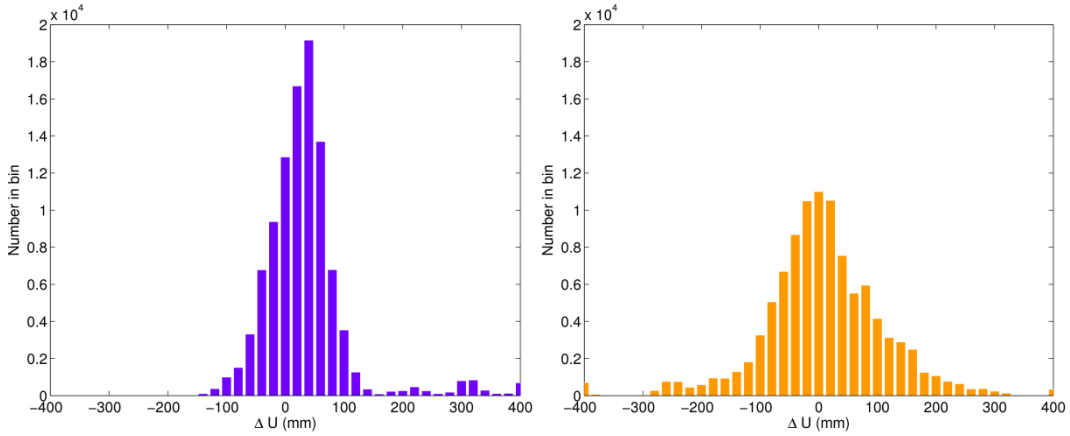


Figure 8-16. Histograms of height accuracy at SNTR between a height range of 300 - 400 m from PPPNCL kinematic GPS+GLONASS (left) and GPS-only (right) PPP solutions and the reference trajectory. Each bin size represents 20 mm of height difference.

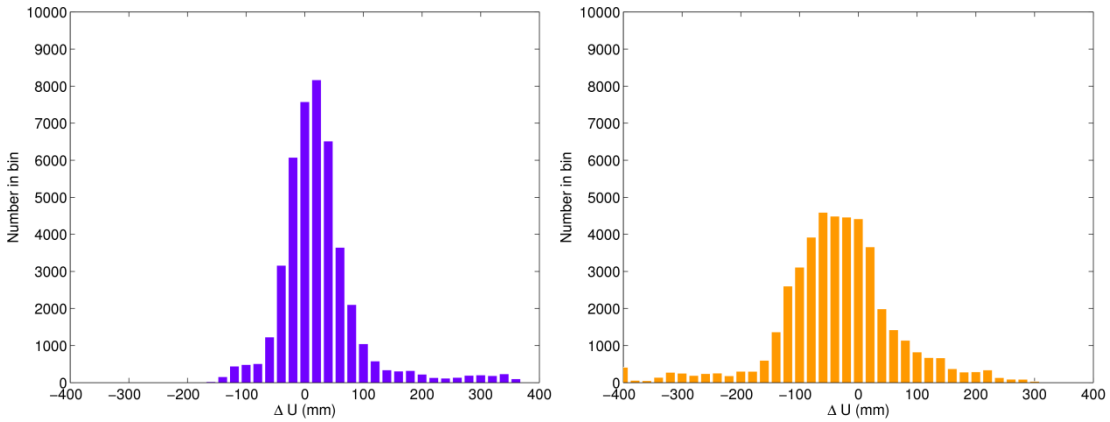


Figure 8-17. Histograms of height accuracy at SNTR between a height range of 1000 - 1100 m from PPPNCL kinematic GPS+GLONASS (left) and GPS-only (right) PPP solutions and the reference trajectory. Each bin size represents 20 mm of height difference.

To investigate where the improvements from the inclusion of GLONASS observations in a PPP solution occur, the height accuracy from PPPNCL compared with the number of GPS satellites used in a solution were analysed. The number of satellites used in the kinematic GPS-only PPP solution was defined by the number of phase observables per epoch. The epochs of the observations for each GPS satellite number were used to group the kinematic GPS+GLONASS PPP solution height differences. The mean, median, RMS and standard deviation of the height differences per satellite number between an ellipsoid height of 255 - 1120 m are displayed in Figure 8-18. The results

for when there are 12 GPS satellites observed are included in the graph, but there are only 87 epochs out of the 468383 observations where this occurred so the statistics are not as robust as the larger sample sizes from the other groups of satellite numbers. For the kinematic GPS-only PPP solution the mean, median, RMS and standard deviation of the height differences decrease as the number of satellites increase from 4 to 10. However, the kinematic GPS+GLONASS PPP solution provides a more consistent height accuracy with mean height differences of 29 mm and 33 mm with 4 and 10 satellites compared to mean height differences for the kinematic GPS-only PPP solution of -152 mm and 18 mm with 4 and 10 satellites. The precision of the kinematic GPS+GLONASS PPP solutions shows an improvement with the increase of GPS satellites with the standard deviation reducing from 128 mm to 57 mm for 4 to 10 satellites, though the RMS and standard deviation was smaller for each satellite number from 4 to 10 than the GPS-only solution. The largest improvement from the inclusion of GLONASS occurs at the lower satellite numbers. The mean absolute values of height difference are smaller for the kinematic GPS+GLONASS PPP solutions between satellite numbers 4 to 7, with the magnitude of the improvement decreasing with the increase in satellite number between 4 and 7. When there are eight or more satellites the kinematic GPS-only PPP solution has a smaller bias, but not a smaller standard deviation suggesting that there is less noise in the kinematic GPS+GLONASS PPP solution. The height dependent mean and median bias in the kinematic GPS-only PPP solution could be a consequence of a reduction in the percentage of positions with observations over 8 satellites, as demonstrated in Figure 8-19.

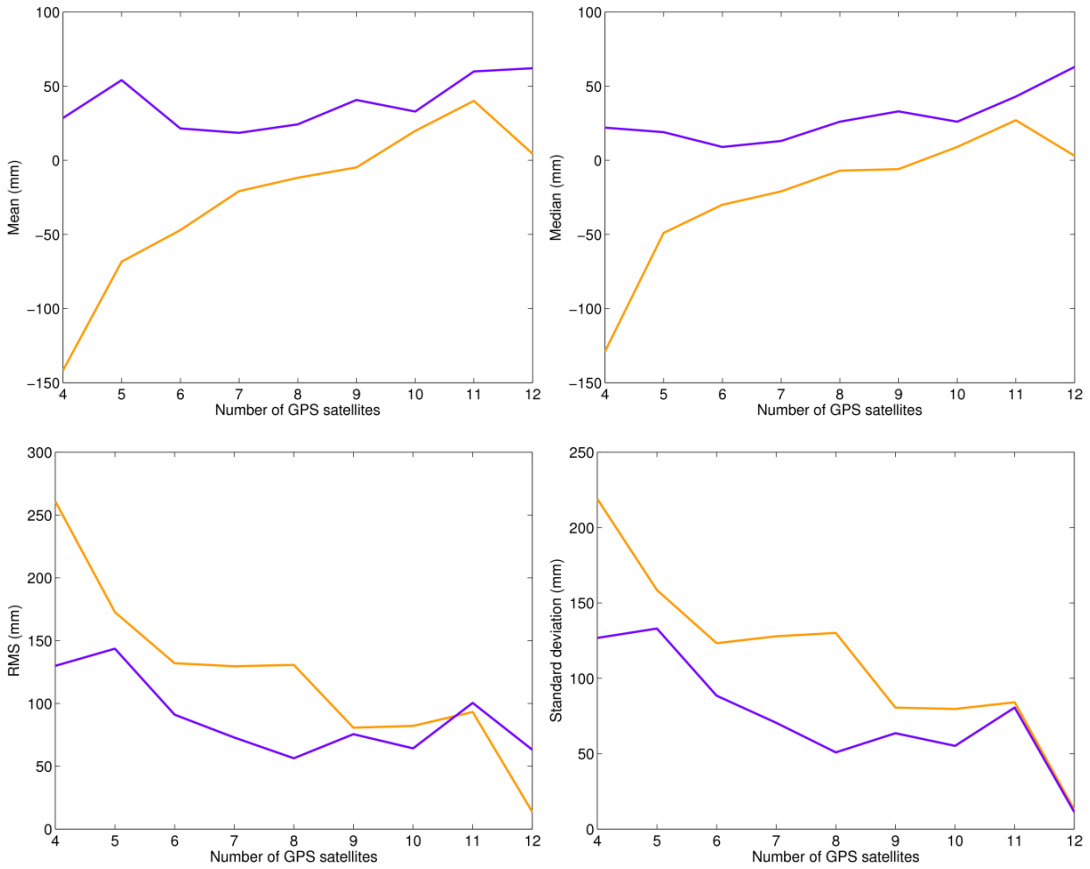


Figure 8-18. Mean (upper left pane), median (upper right pane), RMS (lower left pane), and standard deviation (lower right pane) of height accuracy at SNTR compared to the reference trajectory, as a function of number of GPS satellites used, for kinematic PPP solutions using GPS+GLONASS (purple) and GPS-only (orange).

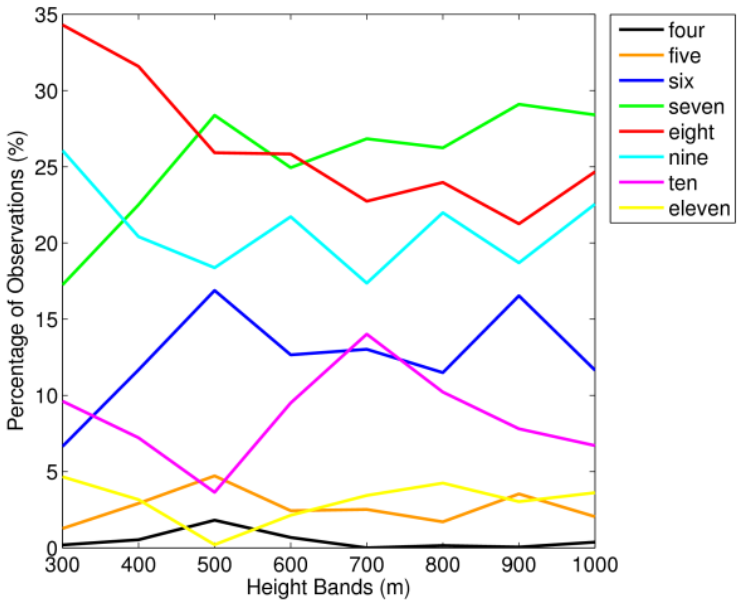


Figure 8-19 Percentage of observation for the number of satellites used in the kinematic GPS-only PPP positions (in 100 m ellipsoidal height bins).

## 8.6. Absolute compared with relative kinematic GNSS positioning

In the previous sections of this chapter the optimal tropospheric mitigation strategies for relative and absolute kinematic GNSS positioning have been assessed and benchmarked. The optimal configurations of the two techniques will now be compared to assess performance and technique specific benefits. ESA orbits were used for the Track kinematic double-difference positioning solution and PPPNCL kinematic PPP solution, with the same process noise values and configuration settings used in Chapter 7. The RMS, standard deviation, median, and mean differences for the relative and absolute heights validated against the GIPSY-derived reference coordinates are displayed in Table 8-8.

Table 8-8. RMS, standard deviation, median, and mean of the differences in height between kinematic GPS+GLONASS PPP solutions and kinematic GPS-only double-difference positioning solutions with GIPSY-derived reference height for SNLB and SNSU. All quantitities expressed in millimetres.

| | SNLB | | | | SNSU | | | |
|---|---|---|---|---|---|---|---|---|
| | RMS | STD | Median | Mean | RMS | STD | Median | Mean |
| Absolute | 34 | 34 | 0 | 1 | 30 | 30 | -1 | 0 |
| Relative | 28 | 27 | 8 | 9 | 28 | 27 | -7 | -8 |

The baseline between SNTR and SNLB never exceeds ~6 km, but for most airborne GNSS positioning scenarios, a ground-based known station is unlikely to be situated to provide such a short baseline. SNTR was therefore processed relative to the closest OS CGNSS station ASAP, providing a maximum baseline of 45.3 km. A cycle slip was evident on day of year 250 at 10:00:05 with a positional error of ~3 - 4 m until 10:19:45 when SNTR loses lock through the wooded section of railway and the ambiguities are re-initialised. The mean, median, RMS and standard deviation of the height differences at SNTR for a kinematic GPS-only double-difference positioning solution relative to ASAP, a kinematic GPS-only double-difference positioning solution relative to SNLB, and a kinematic GPS+GLONASS PPP solution are displayed in Figure 8-20. The standard deviation and RMS of the height differences for the long baseline kinematic GPS-only double-difference positioning solution over the 100 m height bands are

three times greater than the values for the shorter baseline kinematic GPS-only double-difference positioning solution relative to SNLB and the kinematic GPS+GLONASS PPP solution. The different conditions experienced at ASAP and SNTR due to the ~45 km separation results in the double differencing procedure not being as effective.

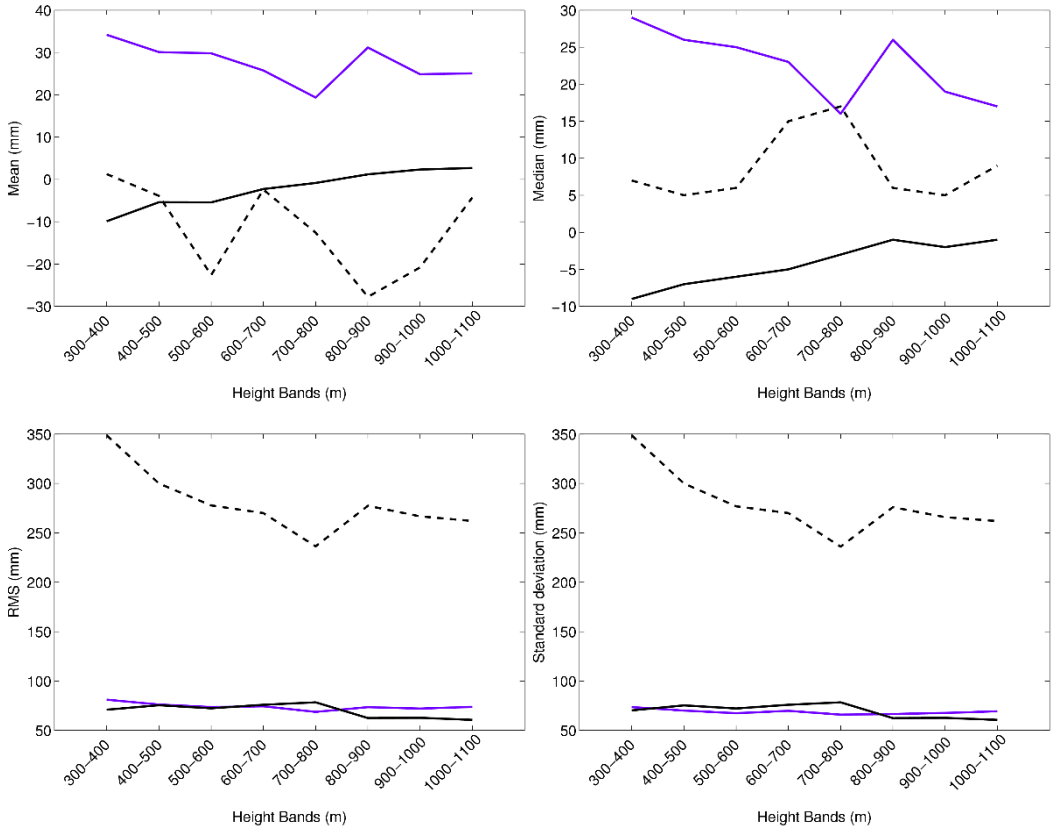


Figure 8-20. Mean (upper left pane), median (upper right pane), RMS (lower left pane), and standard deviation (lower right pane) of height accuracy (in 100 m ellipsoidal height bins) between the reference trajectory and a kinematic GPS+GLONASS PPP solution (continuous purple), and a short baseline (continuous black) and long baseline (dashed black) kinematic GPS-only double-difference positioning solutions for SNTR.

The parameterisation of the tropospheric delay has been shown earlier in this chapter to remove the height dependent bias in the mitigation of the tropospheric delay. The standard deviation of the height differences for the short baseline kinematic GPS-only double-difference positioning solution and the kinematic GPS+GLONASS PPP solution are 71 mm and 72 mm respectively, with the kinematic GPS-only double-difference positioning solution having a smaller bias of -5 mm compared to 24 mm. Histograms

of the height differences over the height range of 255 - 1120 m are displayed in Figure 8-21. The 5th and 95th centiles of the height difference for the short baseline kinematic GPS-only double-difference positioning solution are -99 mm and 94 mm respectively compared to -60 mm and 121 mm for the kinematic GPS+GLONASS PPP solution. The kinematic GPS+GLONASS PPP solution performs to a similar precision to the short baseline kinematic GPS-only double-difference positioning solution over a range of heights, although there is an evident bias in the kinematic GPS+GLONASS PPP solution. The bias appears to be a result of sensitivity to the tropospheric process noise value applied. Dependent on the subset of the dataset used alters the optimal tropospheric process noise, and highlights the importance of using a representative value.

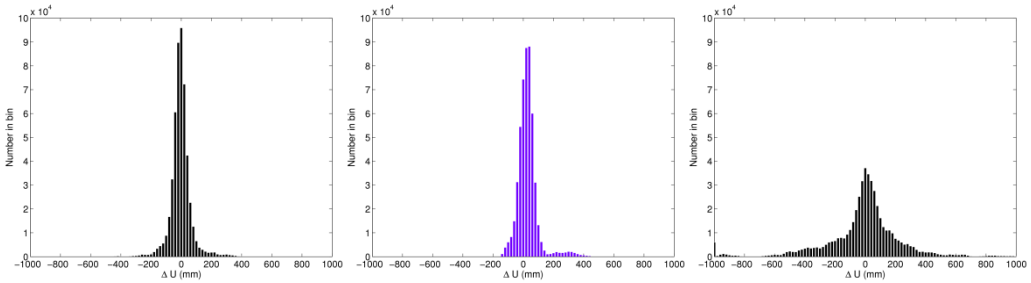


Figure 8-21. Histograms at SNTR (between an ellipsoidal height range of 255 - 1120 m) of height accuracy from a Track kinematic GPS-only double-difference positioning solution relative to SNLB (left), a PPPNCL kinematic GPS+GLONASS PPP solution (middle), and a Track kinematic GPS-only double-difference positioning solution relative to ASAP (right) and the reference trajectory. Each bin size represents 20 mm of height difference.

## 8.7. Conclusion

Tropospheric mitigation using empirical modelling, and by estimation, have been tested for both relative and absolute kinematic GNSS positioning techniques. Solutions were computed for SNTR, a GNSS station installed on a moving platform, i.e. the SMR carriage, undergoing ~950 m vertical height change. Kinematic double-difference positioning solutions were processed against reference GNSS station on a stable platform (SNLB) to simulate a short baseline and against an OS GNSS station (ASAP) to simulate a more realistic baseline length for airborne GNSSS positioning. The solutions' and the mitigation methods' effectiveness in mitigating the

tropospheric delay were assessed by comparison with a reference trajectory (an average of ~200 trajectories collected over a 50 day period computed using kinematic double-difference positioning relative to SNLB and SNSU at the extremities of railway). Due to errors in the mitigation of the tropospheric delay being most prominent in the height component, the height accuracy determined between the solutions and a GIPSY-derived reference height were analysed and used to assess the performance of the solutions. The empirical tropospheric models and estimation of the delay for the solution types were assessed per trajectory, over a range of heights, and a range of ZWD conditions.

Of the empirical tropospheric models tested for the kinematic GPS-only double-difference positioning solution, the EGNOS model was found to perform best with the smallest median bias and standard deviation, over the 255 - 1120 m height range tested, of -1 mm and 61 mm respectively. With each empirical tropospheric model tested the difference in height between the kinematic GNSS positioning solution and the reference trajectory increased as the difference in height between SNTR and SNLB increased. The rate of error in height with change in height is smallest for the EGNOS model with a difference in the median bias of 22 mm between height bands 300 - 400 m and 1000 - 1100 m, compared to a difference of -56 mm for the Saastamoinen with GPT2 input model. The UNB3m model also has the smallest median biases when height differences are assessed with respect to the ZWD lapse rate experienced across the site (in 5 mm of ZWD bands).

All the empirical tropospheric models were tested with the same mapping function (GMF). Therefore the models' performance is likely to alter if not using the commonly associated mapping function. For example the EGNOS model uses the Black and Eisner mapping function (Black and Eisner, 1984) which does not differentiate between the hydrostatic and non-hydrostatic components, and does not consider spatial and seasonal variability in atmospheric conditions.

8. Effect of tropospheric mitigation strategies on height estimation in kinematic GNSS positioning

If the tropospheric delay is estimated as a parameter in a GNSS solution, rather than being purely modelled, then the magnitude and variability of delay can be mitigated more accurately. When the ZWD is parameterised in the kinematic double-difference positioning solution the median bias over the height range of 255 - 1120m for SNTR is -5 mm, and the decrease in the height accuracy with altitude seen with the models has been removed. It has also been demonstrated that estimating ZWD can represent the short term temporal variability in the ZWD and variations in the ZWD lapse rate allowing a height accuracy of 72 mm (RMS) to be achieved. Where the empirical tropospheric models can mitigate the tropospheric delay to a similar extent as estimating the delay this relies on the nominal coefficients used in the model matching the actual conditions experienced at the site. The mean height accuracy was analysed dependent on the difference in ZWD between SNLB and SNTR over the height range 1000 - 1100 m. The kinematic GNSS positioning solution estimating the delay had a maximum and minimum median height accuracy of -1 mm and -9 mm respectively, compared to -28 mm and -54 mm from the Saastamoinen with GPT input model highlighting, that estimating the ZWD is paramount to achieving the highest height accuracy.

It is clearly beneficial to estimate a ZWD correction in kinematic double-difference positioning and PPP solutions for airborne GNSS positioning, and this should be considered in commercial software packages as it is in the Track scientific software. The maximum difference in height between SNLB and SNTR is ~950 m, therefore for airborne GNSS applications that operate at greater heights the error from unmitigated delay will be larger, and the parameterisation of the ZWD becomes even more important. For kinematic PPP, due to not differencing observations to a known station, unmitigated tropospheric delay propagates directly into the height component and if not estimated could be the largest error source (0.3 m) in a kinematic PPP solution, as has been demonstrated in this chapter.

The benefit of using GPS+GLONASS compared to using only GPS in a kinematic PPP solution has been demonstrated, with the multi-GNSS solution providing RMS and

standard deviations of the height differences between the height range of 255 - 1120 m of 78 mm and 72 mm compared to 129 mm and 128 mm. The improvement that the inclusion of GLONASS observations provide to the solution is most pronounced for scenarios when there a low number of GPS satellites used in the solution. This provides confidence in the results presented in Chapter 7, where an improvement is evident for a multi-GNSS solution compared to a GPS-only solution for estimating the ZWD from a kinematic receiver.

When considering the implications of using a certain solution for kinematic GNSS positioning over an altitude range the kinematic double-difference positioning solution estimating the tropospheric delay over a short baseline provides the optimal solution with average median and mean height accuracy for the 100 m height bands of -4 mm and -2 mm respectively, compared to 23 mm and 28 mm for the kinematic GPS+GLONASS PPP solution, While both solutions have an RMS and standard deviation of ~70 mm. When the kinematic double-difference positioning solution is computed over a longer baseline (45 km) the kinematic PPP solution provides a better height accuracy, evident in the smaller standard deviations of 72 mm compared to 272 mm.

# 9. Conclusions

The research presented in this thesis has focused on the impact of tropospheric delay on kinematic GNSS positioning over a range of altitudes. The acquisition of the unique SMR dataset has allowed the retrieval of tropospheric delay values, and the height accuracy from kinematic GNSS positioning undergoing a change in altitude to be assessed. This chapter will summarise the research undertaken and the conclusions drawn that are included in the thesis.

## 9.1. Summary of work

The effect of atmospheric water vapour on climatic and meteorological events and GNSS positioning were introduced in Chapters 2 and 3. The case for why water vapour content in the atmosphere has to be monitored and its impact for GNSS positioning were established, with the current limitations highlighted. The aims and objectives of the research were developed to try to address the current limitations, such as to increase observations of water vapour in currently data sparse areas, and to validate a kinematic GNSS dataset in a variety of tropospheric conditions and over an altitude range.

The suitability of the SMR to fulfil the aims and objectives of the project was outlined in Chapter 4, along with a detailed description of the collected observation dataset and the establishing of a reference datasets to validate kinematic GNSS positioning. Chapter 5 described the tropospheric comparators used to validate tropospheric delay values.

Chapters 6 and 7 validated tropospheric delay values from empirical tropospheric models and from parameterising the delay in relative and absolute kinematic GNSS positioning. The height accuracy from relative and absolute kinematic GNSS

positioning was validated in Chapter 8 with a variety of tropospheric mitigation strategies, and the height accuracy benchmarked for each scenario.

To enable the work to be carried out a number of software amendments were implemented in both Track and PPPNCL. The EGNOS and UNB3m empirical tropospheric models, and the GPT2 input into the Saastamoinen model were included into the Track software. Furthermore, amendments to the default relative humidity values used in the wet GMF, and use of the hydrostatic and wet GMF with the separately input ZHD and ZWD were implemented into the double differencing software. Back-smoothing was introduced into the PPPNCL software to allow the software to provide a post-processed solution.

## 9.2. Final conclusions

A suitable test platform was identified and used to acquire a unique dataset that allowed the assessment of height accuracy and tropospheric delay estimation from kinematic GNSS positioning over an altitude range. The ~950 m variation in height experienced by the receiver, the ability to install GNSS stations on stable platforms at the extremities of the trajectory, and the repeatable trajectory undertaken by the GNSS station on a moving platform allowed a robust reference trajectory and tropospheric delay profiles to be established.

The SMR allowed a range of empirical tropospheric models currently used in kinematic GNSS positioning to be validated against reference tropospheric delay values for the GNSS stations on both stable and moving platforms, with the models' ability to represent the ZHD, ZWD and ZTD assessed. The optimal models tested were the UNB3m and EGNOS model with median biases from the reference ZWD values of -3.7 mm and 14.5 mm and RMS values of 38.3 mm and 36.6 mm respectively, highlighting the limitation of empirical tropospheric models in representing the high temporal variations in the tropospheric delay.

The retrieval of ZWD estimates from a kinematic GPS+GLONASS PPP solution and a short baseline kinematic GPS-only double differencing solution provided a similar accuracy with an RMS agreement for both solutions of ~12 mm over the tropospheric profile offered by SNTR. When baselines lengths for the kinematic GPS-only double differencing solution were increased to 40 - 50 km the ZWD agreement worsened by 7 - 11 mm. The improvement in kinematic PPP solutions when using GPS+GLONASS as opposed to GPS-only was demonstrated, with the GPS-only solution providing a ZWD RMS agreement of 16 mm. Due to the decrease in ZWD accuracy with the increase in baseline length, and therefore the constraint of a known station to achieve high accuracy ZWD estimates in kinematic double differencing, the kinematic GPS+GLONASS PPP solution offers the preferred option for collecting tropospheric delay values in a variety of scenarios.

The positional accuracies from kinematic GNSS positioning solutions were validated for multiple (~200) trajectories experiencing a variation in height of up to 950 m over a 50 day period. Due to errors in mitigating the tropospheric error predominantly propagating into height, the accuracy in this component was used to assess the solution types and tropospheric mitigation strategies. The empirical tropospheric models validated in Chapter 6 were assessed in terms of the height accuracy available when implemented in to a kinematic GPS-only double-difference positioning solution. The EGNOS model was found to be the optimal empirical model with a median bias between -12 mm and 10 mm for 100 m height bins between 300 and 1100 mm. The empirical tropospheric models are able to represent the nominal delay; when the tropospheric conditions vary from this nominal delay, the median variation can increase to 39 mm for the EGNOS model. When the tropospheric delay is parameterised in the relative solution a height accuracy of median bias -5 mm and a standard deviation of 71 mm is achieved, with the accuracy unaffected by the variations in the ZWD lapse rate. Following on from the validation of relative GNSS positioning solutions the positional accuracy from a kinematic PPP solution was assessed, along with the impact of including GLONASS with GPS observations. The kinematic GPS+GLONASS PPP solution provided a standard deviation of 72 mm over

the height range 255 - 1120 m, a similar value from the kinematic GPS-only double-difference positioning solution. The kinematic GPS+GLONASS PPP solution also provided an improvement compared to the kinematic GPS-only PPP solution, which had a standard deviation of 128 mm between the height range 255 - 1120 m. The improved height accuracy and tropospheric delay estimates from the kinematic GPS+GLONASS PPP solution compared to the height GPS-only PPP solution demonstrates that a multi-system GNSS solution should be utilised in kinematic GNSS positioning for ZWD and height estimation.

## 9.3. Further work

The potential of tropospheric estimation and mitigation using kinematic GNSS positioning over a range of altitudes has been established in the research presented. The potential of absolute GNSS positioning solutions offer advantages to relative GNSS positioning solutions due to not being constrained by distance to a ground-based known station. Therefore a number of suggestions are made for future work related to the collection of atmospheric water vapour data and mitigation of tropospheric delay from kinematic PPP, leading on from the research presented in this thesis:

- Assessing the effect of GPS and GLONASS integer ambiguity resolution on kinematic PPP, and its impact on estimating the tropospheric delay.

- Testing real-time kinematic PPP solutions, using real-time satellite orbit and clock products.

- Further examination of how to choose an appropriate tropospheric process noise value on a daily basis when a reference truth is not available for tuning purposes.

- Investigation of the assimilation of kinematic PPP estimates of ZWD/ZTD into NWMs, and the impact of these estimates in forecasting.

- Assessing the effect of including other GNSS signals such as observations from the European Galileo and Chinese BeiDou.

- Implement VMF1 mapping function into Track and PPPNCL for post-processed solutions.

The use of aircraft to collect temperature, pressure, relative humidity and freezing information are currently collected from a select range of research and commercial aircrafts (Moninger *et al.*, 2003). Meteorological data collected on aircraft by Aircraft Communications Addressing and Report System (ACARS) and Aircraft Meteorological Data Relay (AMDAR) demonstrate that the infrastructure and successful acquisition of real-time data from commercial aircraft and the assimilation into numerical weather models is already in place. Dual frequency GNSS receivers have also been installed on aircrafts and utilized for RO experiments (instead of from a low Earth orbiting satellite) to allow the collection of atmospheric meteorological data above an altitude of 4 km, with the aim of being assimilated into NWM (Haase *et al.*, 2014). These examples highlight the potential for kinematic PPP being used on airborne platforms for the estimation of ZWD and contribution to NWMs as another operational water vapour data source.

.

# References

Agnew, D.C. (1997) 'NLOADF: A program for computing ocean-tide loading', *Journal of Geophysical Research*, 102(B3), pp. 5109-5110.

Anquela, A.B., Martin, A., Berne, J.L. and Padin, J. (2013) 'GPS and GLONASS static and kinematic ppp results', *Journal of Surveying Engineering-Asce*, 139(1), pp. 47-58.

Baker, T.F. (1984). 'Tidal deformations of the Earth', Science Progress, 69, pp. 197-233.

Baker, H.C., Dodson, A.H., Penna, N.T., Higgins, M. and Offiler, D. (2001) 'Ground-based GPS water vapour estimation: Potential for meteorological forecasting', *Journal of Atmospheric and Solar-Terrestrial Physics*, 63(12), pp. 1305-1314.

Bedka, S., Knuteson, R., Revercomb, H., Tobin, D. and Turner, D. (2010) 'An assessment of the absolute accuracy of the Atmospheric Infrared Sounder v5 precipitable water vapor product at tropical, midlatitude, and arctic ground-truth sites: September 2002 through August 2008', *Journal of Geophysical Research-Atmospheres*, 115, D17310.

Bender, M., Dick, G., Wickert, J., Schmidt, T., Song, S., Gendt, G., Ge, M. and Rothacher, M. (2008) 'Validation of GPS slant delays using water vapour radiometers and weather models', *Meteorologische Zeitschrift*, 17(6), pp. 807-812.

Bennitt, G.V. and Jupp, A. (2012) 'Operational assimilation of GPS zenith total delay observations into the Met Office numerical weather prediction models', *Monthly Weather Review*, 140(8), pp. 2706-2719.

Berg, H. (1948) *Allgemeine Meteorologie*. Dummler, Bonn.

Berg, P., Moseley, C. and Haerter, J.O. (2013) 'Strong increase in convective precipitation in response to higher temperatures', *Nature Geoscience*, 6(3), pp. 181-185.

Bertiger, W., S. D. Desai, B. Haines, N. Harvey, A. W. Moore, S. Owen, and J. P. Weiss (2010), 'Single receiver phase ambiguity resolution with GPS data', *Journal of Geodesy*, 84(5), 327-337.

Best, M.J., Pryor, M., Clark, D.B., Rooney, G.G., Essery, R.L.H., Menard, C.B., Edwards, J.M., Hendry, M.A., Porson, A., Gedney, N., Mercado, L.M., Sitch, S., Blyth, E., Boucher, O., Cox, P.M., Grimmond, C.S.B. and Harding, R.J. (2011) 'The Joint UK Land Environment Simulator (JULES), model description - Part 1: Energy and water fluxes', *Geoscientific Model Development*, 4(3), pp. 677-699.

Betaille, D. (2003) 'Testing methodology for GPS phase multipath mitigation techniques', *Proceedings of the 16th International Technical Meeting of the Satellite Division of The Institute of Navigation*. Portland, Oregon, September 2003. pp. 2151-2162.

Bevis, M., Businger, S., Herring, T.A., Rocken, C., Anthes, R.A. and Ware, R.H. (1992) 'GPS meteorology: Remote sensing of atmospheric water vapor using the Global Positioning System', *Journal of Geophysical Research*, 97(D14), pp. 15787 -15801.

Bilich, A. and Larson, K.M. (2007) 'Mapping the GPS multipath environment using the signal-to-noise ratio (SNR)', *Radio Science*, 42, RS6003.

Black, H.D. and Eisner, A. (1984) 'Correcting satellite doppler data for tropospheric effects', *Journal of Geophysical Research-Atmospheres*, 89(2), pp. 2616-2626.

Bisnath, S. and Gao, Y. (2009) 'Current State of Precise Point Positioning and Future Prospects and Limitations', in Sideris, M. (ed.) *Observing our Changing Earth*. Springer Berlin Heidelberg, pp. 615-623.

Bock, O., Tarniewicz, J., Thom, C., Pelon, J. and Kasser, M. (2001) 'Study of external path delay correction techniques for high accuracy height determination with GPS', *Physics and Chemistry of the Earth Part a-Solid Earth and Geodesy*, 26(3), pp. 165-171.

Boehm, J., Heinkelmann, R. and Schuh, H. (2007) 'Short Note: A global model of pressure and temperature for geodetic applications', *Journal of Geodesy*, 81(10), pp. 679-683.

Boehm, J., Niell, A., Tregoning, P. and Schuh, H. (2006a) 'Global Mapping Function (GMF): A new empirical mapping function based on numerical weather model data', *Geophysical Reasearch letters*, 33, L07304.

Boehm, J., Werl, B. and Schuh, H. (2006b) 'Troposphere mapping functions for GPS and very long baseline interferometry from European Centre for Medium-Range Weather Forecasts operational analysis data', *Journal of Geophysical Research-Solid Earth*, 111, B02406.

Bokoye, A.I., Royer, A., Cliche, P. and O'Neill, N. (2007) 'Calibration of sun radiometer-based atmospheric water vapor retrievals using GPS meteorology', *Journal of Atmospheric and Oceanic Technology*, 24(6), pp. 964-979.

Boniface, K., Champollion, C., Chery, J., Ducrocq, V., Rocken, C., Doerflinger, E. and Collard, P. (2012) 'Potential of shipborne GPS atmospheric delay data for prediction of Mediterranean intense weather events', *Atmospheric Science Letters*, 13(4), pp. 250-256.

Bruegge, C.J., Conel, J.E., Green, R.O., Margolis, J.S., Holm, R.G. and Toon, G. (1992) 'Water-vapor column abundance retrievals during fife', *Journal of Geophysical Research-Atmospheres*, 97(D17), pp. 18759-18768.

Byram, S., Hackman, C. and Tracey, J. (2011) 'Computation of a high-precision GPS-based troposphere product by the USNO', *Proceedings of the 24th International Technical Meeting of the Satellite Division of the Institute of Navigation (ION GNSS 2011)*, pp. 572-578.

Byun, S.H. and Bar-Sever, Y.E. (2009) 'A new type of troposphere zenith path delay product of the international GNSS service', *Journal of Geodesy*, 83(3-4), pp. 367-373.

Byun, S.H., Hajj, G.A. and Young, L.E. (2002) 'Development and application of GPS signal multipath simulator', *Radio Science*, 37(6), 1098.

Cadeddu, M.P., Liljegren, J.C. and Turner, D.D. (2013) 'The Atmospheric radiation measurement (ARM) program network of microwave radiometers: instrumentation, data, and retrievals', *Atmospheric Measurement Techniques*, 6(9), pp. 2359-2372.

Cai, C. and Gao, Y. (2013) 'Modeling and assessment of combined GPS/GLONASS precise point positioning', *GPS Solutions*, 17(2), pp. 223-236.

Chadwell, C.D. and Bock, Y. (2001) 'Direct estimation of absolute precipitable water in oceanic regions by GPS tracking of a coastal buoy', *Geophysical Research Letters*, 28(19), pp. 3701-3704.

Chen, G. (1998) *GPS kinematic positioning for the airborne laser altimetry at Long Valley, California*. Ph.D thesis. Department of Earth, Atmospheric, and Planetary Sciences, Massachusetts Institute of Technology, Cambridge, MA.

Chen, Q., Song, S., Heise, S., Liou, Y.-A., Zhu, W. and Zhao, J. (2011) 'Assessment of ZTD derived from ECMWF/NCEP data with GPS ZTD over China', *GPS Solutions*, 15(4), pp. 415-425.

Chen, S.-H., Zhao, Z., Haase, J.S., Chen, A. and Vandenberghe, F. (2008) 'A study of the characteristics and assimilation of retrieved MODIS total precipitable water data in severe weather simulations', *Monthly Weather Review*, 136(9), pp. 3608-3628.

Choy, S., Zhang, S., Lahaye, F. and Héroux, P. (2013) 'A comparison between GPS-only and combined GPS+GLONASS precise point positioning', *Journal of Spatial Science*, 58(2), pp. 169-190.

COESA (1966) 'U.S. Standard Atmosphere Supplements, 1966'. U.S. Committee on Extension to the Standard Atmosphere. Superintendent of Documents, U.S. Government Printing Office, Washington, D.C.

Collins, J.P. and Langley, R. (1997) 'A tropospheric delay model for the user of the Wide Area Augmentation System', *Final Contract Report Prepared for Nav Canada, Department of Geodesy and Geomatics Engineering Technical Report No. 187*.

Colombo, O., Sutter, A.W. and Evans, A.G. (2004) 'Evaluation of precise kinematic GPS point positioning', *Proceedings of the 17th International Technical Meeting of the Satellite Division of the Institute of Navigation, ION GNSS 2004*. Long Beach, CA. pp. 1423 - 1430.

Colombo, O.L. (1986) 'Ephemeris errors of GPS satellites', *Bulletin Géodésique*, 60(1), pp. 64-84.

Cretaux, J.F., Calmant, S., Romanovski, V., Perosanz, F., Tashbaeva, S., Bonnefond, P., Moreira, D., Shum, C.K., Nino, F., Berge-Nguyen, M., Fleury, S., Gegout, P., Abarca Del Rio, R. and Maisongrande, P. (2011) 'Absolute calibration of Jason radar altimeters from GPS kinematic campaigns over Lake Issykkul', *Marine Geodesy*, 34(3-4), pp. 291-318.

Davies, T., Cullen, M.J.P., Malcolm, A.J., Mawson, M.H., Staniforth, A., White, A.A. and Wood, N. (2005) 'A new dynamical core for the Met Office's global and regional modelling of the atmosphere', *Quarterly Journal of the Royal Meteorological Society*, 131(608), pp. 1759-1782.

Davis, J.L., Herring, T.A., Shapiro, II, Rogers, A.E.E. and Elgered, G. (1985) 'Geodesy by radio interferometry - effects of atmospheric modeling errors on estimates of baseline length', *Radio Science*, 20(6), pp. 1593-1607.

Deblonde, G. and Wagneur, N. (1997) 'Evaluation of global numerical weather prediction analyses and forecasts using DMSP special sensor microwave imager retrievals .1. Satellite retrieval algorithm intercomparison study', *Journal of Geophysical Research-Atmospheres*, 102(D2), pp. 1833-1850.

Deeter, M.N. (2007) 'A new satellite retrieval method for precipitable water vapor over land and ocean', *Geophysical Research Letters*, 34, L02815.

Diedrich, H., Preusker, R., Lindstrot, R. and Fischer, J. (2013) 'Quantification of uncertainties of water vapour column retrievals using future instruments', *Atmospheric Measurement Techniques*, 6(2), pp. 359-370.

Dixon, T.H. and Wolf, S.K. (1990) 'Some tests of wet tropospheric calibration for the CASA Uno global positioning system experiment', *Geophysical Research Letters*, 17(3), pp. 203-206.

Dodson, A.H., Chen, W., Penna, N.T. and Baker, H.C. (2001) 'GPS estimation of atmospheric water vapour from a moving platform', *Journal of Atmospheric and Solar-Terrestrial Physics*, 63(12), pp. 1331-1341.

Dodson, A.H., Shardlow, P.J., Hubbard, L.C.M., Elgered, G. and Jarlemark, P.O.J. (1996) 'Wet tropospheric effects on precise relative GPS height determination', *Journal of Geodesy*, 70, pp. 188-202.

Dousa, J. (2001) 'Towards an operational near real-time precipitable water vapor estimation', *Physics and Chemistry of the Earth Part a-Solid Earth and Geodesy*, 26(3), pp. 189-194.

Dousa, J. (2010) 'The impact of errors in predicted GPS orbits on zenith troposphere delay estimation', *GPS Solutions*, 14(3), pp. 229-239.

Dousa, J. and Bennitt, G.V. (2013) 'Estimation and evaluation of hourly updated global GPS Zenith Total Delays over ten months', *GPS Solutions*, 17(4), pp. 453-464.

Dousa, J. and Vaclavovic, P. (2014) 'Real-time zenith tropospheric delays in support of numerical weather prediction applications', *Advances in Space Research*, 53(9), pp. 1347-1358.

Dow, J.M., Neilan, R.E. and Rizos, C. (2009) 'The International GNSS Service in a changing landscape of Global Navigation Satellite Systems', *Journal of Geodesy*, 83(3-4), pp. 191-198.

Durre, I., Vose, R.S. and Wuertz, D.B. (2006) 'Overview of the Integrated Global Radiosonde Archive', *Journal of Climate*, 19(1), pp. 53-68.

Edwards, S.J., Clarke, P.J., Penna, N.T. and Goebell, S. (2010) 'An examination of network RTK GPS services in Great Britain', *Survey Review*, 42(316), pp. 107-121.

Elgered, G., Haas, R., Wahlborn, J. and Ning, T. (2012) 'Assessing the quality of water vapor radiometer data from Onsala during the CONT11 geodetic VLBI campaign', *IVS 2012 general meeting proceedings*. Madrid, Spain, March 4-9, 2012. pp. 410-414.

Emardson, T.R., Elgered, G. and Johansson, J.M. (1999) 'External atmospheric corrections in geodetic very-long-baseline interferometry', *Journal of Geodesy*, 73(7), pp. 375-383.

Estey, L.H. and C.M. Meertens (1999) 'TEQC: The multi-purpose toolkit for GPS/GLONASS data, *GPS Solutions*, 3(1), pp. 42-49.

Fairhurst, P. (2007) *Towards a Real-Time Tightly Coupled GPS/INS Positioning System*. Ph.D thesis. School of Civil Engineering and Geosciences, Newcastle University.

Ferrare, R.A., Melfi, S.H., Whiteman, D.N., Evans, K.D., Schmidlin, F.J. and Starr, D.O. (1995) 'A comparison of water-vapor measurements made by raman lidar and radiosondes', *Journal of Atmospheric and Oceanic Technology*, 12(6), pp. 1177-1195.

Fujita, M., Kimura, F., Yoneyama, K. and Yoshizaki, M. (2008) 'Verification of precipitable water vapor estimated from shipborne GPS measurements', *Geophysical Research Letters*, 35(13), L13803.

Gao, Y. and Shen, X. (2004) 'Performance analysis of precise point positioning using real-time orbit and clock products', *Journal of Global Positioning Systems*, 3(1-2), pp. 95-100.

Ge, M.R., Calais, E. and Haase, J. (2002) 'Sensitivity of zenith total delay accuracy to GPS orbit errors and implications for near-real-time GPS meteorology', *Journal of Geophysical Research-Atmospheres*, 107(D16), 4315.

Gerber, D., Balin, I., Feist, D.G., Kampfer, N., Simeonov, V., Calpini, B. and van den Bergh, H. (2004) 'Ground-based water vapour soundings by microwave radiometry and Raman lidar on Jungfraujoch (Swiss Alps)', *Atmospheric Chemistry and Physics*, 4, pp. 2171-2179.

Glowacki, T.J., Penna, N.T. and Bourke, W.P. (2006) 'Validation of GPS-based estimates of integrated water vapour for the Australian region and identification of diurnal variability', *Australian Meteorological Magazine*, 55(2), pp. 131-148.

Goode, M., de Jong, K., Liu, X., Guo, J., Wang, J. and Levilly, S. (2013) 'Initial BeiDou and Galileo PPP results', *GNSS precise point positioning workshop: reaching full potential*. Ottawa, Canada, 12-14 June.

Gorres, B., Campbell, J., Becker, M. and Siemes, M. (2006) 'Absolute calibration of GPS antennas: laboratory results and comparison with field and robot techniques', *GPS Solutions*, 10(2), pp. 136-145.

Groves, P.D. (2013) *Principles of GNSS, inertial, and multisensor integrated navigation systems.* 2nd edn. Artech House Publishers

Groves, P.D., Jiang, Z., Skelton, B., Cross, P.A., Lau, L., Adane, Y. and Kale, I. (2010) 'Novel multipath mitigation methods using a dual-polarization antenna', *23rd International Technical Meeting of the Satellite Division of the Institute of Navigation 2010, ION GNSS 2010*. pp. 140-151.

Gutman, S.I., Sahm, S.R., Benjamin, S.G., Schwartz, B.E., Holub, K.L., Stewart, J.Q. and Smith, T.L. (2004) 'Rapid retrieval and assimilation of ground based GPS precipitable water observations at the NOAA forecast systems laboratory: Impact on weather forecasts', *Journal of the Meteorological Society of Japan*, 82(1B), pp. 351-360.

Haan, S. de. and Jones, J. (2013) 'Guidelines on operational use and data exchange protocols for GNSS water vapour' WMO - Commission for instruments and methods of observation. Geneva, Switzerland, 4-7 March 2013.

Haas, R., Ning, T., Elgered, G. and Ieee (2010) 'Observation of long term trends in the amount of atmospheric water vapor by space geodesy and remote sensing techniques', *2010 Ieee International Geoscience and Remote Sensing Symposium*, pp. 2944-2947.

Haase, J.S., Murphy, B.J., Muradyan, P., Nievinski, F.G., Larson, K.M., Garrison, J.L. and Wang, K.N. (2014) 'First results from an airborne GPS radio occultation system for atmospheric profiling', *Geophysical Research Letters*, 41(5), pp. 1759-1765.

Hadas, T. and Bosy, J. (2014) 'IGS RTS precise orbits and clocks verification and quality degradation over time', *GPS Solutions*, pp. 1-13.

Halthore, R.N., Eck, T.F., Holben, B.N. and Markham, B.L. (1997) 'Sun photometric measurements of atmospheric water vapor column abundance in the 940-nm band', *Journal of Geophysical Research-Atmospheres*, 102(D4), pp. 4343-4352.

Han, S. and Rizos, C. (2000) 'Airborne GPS kinematic positioning and its application to oceanographic mapping', *Earth, Planets and Space*, 52(10), pp. 819-824.

Heise, S., Dick, G., Gendt, G., Schmidt, T. and Wickert, J. (2009) 'Integrated water vapor from IGS ground-based GPS observations: initial results from a global 5-min data set', *Annales Geophysicae*, 27(7), pp. 2851-2859.

Herring, T.A., Davis, J.L. and Shapiro, II (1990) 'Geodesy by radio interferometry - the application of kalman filtering to the analysis of very long base-line interferometry data', *Journal of Geophysical Research-Solid Earth and Planets*, 95(B8), pp. 12561-12581.

Herring, T.A., King, R.W. and McClusky, S.C. (2010) *GAMIT Reference Manual: GPS analysis at MIT. Release 10.4*.

Hesselbarth, A. and Wanninger, L. (2008) 'Short-term stability of GNSS satellite clocks and its effects on precise point positioning', *21st International Technical Meeting of the Satellite Division of the Institute of Navigation, ION GNSS 2008*. pp. 1631-1639.

Hofmann-Wellenhof, B., Lichtenegger, H. and Wasle, E. (2007) *GNSS – Global Navigation Satellite Systems: GPS, GLONASS, Galileo, and more*.

Holben, B.N., Eck, T.F., Slutsker, I., Tanre, D., Buis, J.P., Setzer, A., Vermote, E., Reagan, J.A., Kaufman, Y.J., Nakajima, T., Lavenu, F., Jankowiak, I. and Smirnov, A. (1998) 'AERONET - A federated instrument network and data archive for aerosol characterization', *Remote Sensing of Environment*, 66(1), pp. 1-16.

Hopfield, H.S. (1971) 'Tropospheric effect on electromagnetically measured range - prediction from surface weather data', *Radio Science*, 6(3), pp. 357-367.

Huang, C.-Y., Teng, W.-H., Ho, S.-P. and Kuo, Y.-H. (2013) 'Global variation of COSMIC precipitable water over land: Comparisons with ground-based GPS measurements and NCEP reanalyses', *Geophysical Research Letters*, 40(19), pp. 5327-5331.

Jakobsen, J. and Pedersen, S.M. (2009) 'Design of a GNSS kinematic slotcar test track', *13th IAIN World Congrss*. Stockholm, October 27-29 2009. Nordic Institute of Navigation.

Jin, S., Luo, O.F. and Cho, J. (2009) 'Systematic errors between VLBI and GPS precipitable water vapor estimations from 5-year co-located measurements', *Journal of Atmospheric and Solar-Terrestrial Physics*, 71(2), pp. 264-272.

Jin, S.G., Park, J.U., Cho, J.H. and Park, P.H. (2007) 'Seasonal variability of GPS-derived zenith tropospheric delay (1994-2006) and climate implications', *Journal of Geophysical Research-Atmospheres*, 112, D09110.

Karabatić, A., Weber, R. and Haiden, T. (2011) 'Near real-time estimation of tropospheric water vapour content from ground based GNSS data and its potential contribution to weather now-casting in Austria', *Advances in Space Research*, 47(10), pp. 1691-1703.

Kealy, J., Foster, J. and Businger, S. (2012) 'GPS meteorology: An investigation of ocean-based precipitable water estimates', *Journal of Geophysical Research*, 117, D17303.

King, M.A. (2009) 'The GPS contribution to the error budget of surface elevations derived from airborne LIDAR', *IEEE Transactions on Geoscience and Remote Sensing*, 47(No.3), pp. 874-883.

Kjørsvik, N.S., Øvstedal, O. and Gjevestad, J.G.O. (2009) 'Kinematic precise point positioning during marginal satellite availability', *International Association of Geodesy Symposia*. pp. 691-699.

Kleijer, F. (2001) 'Mapping function induced bias in tropospheric delay estimation using GPS', *Physics and Chemistry of the Earth Part a-Solid Earth and Geodesy*, 26(6-8), pp. 467-470.

Kouba, J. (2008) 'Implementation and testing of the gridded Vienna Mapping Function 1 (VMF1)', *Journal of Geodesy*, 82(4-5), pp. 193-205.

Kouba, J. (2009) 'A simplified yaw-attitude model for eclipsing GPS satellites', *GPS Solutions*, 13(1), pp. 1-12.

Krabill, W.B., Abdalati, W., Frederick, E.B., Manizade, S.S., Martin, C.F., Sonntag, J.G., Swift, R.N., Thomas, R.H. and Yungel, J.G. (2002) 'Aircraft laser altimetry measurement of elevation changes of the greenland ice sheet: technique and accuracy assessment', *Journal of Geodynamics*, 34(3-4), pp. 357-376.

Kuo, Y.H., Schreiner, W.S., Wang, J., Rossiter, D.L. and Zhang, Y. (2005) 'Comparison of GPS radio occultation soundings with radiosondes', *Geophysical Research Letters*, 32, L05817.

Lagler, K., Schindelegger, M., Bohm, J., Krasna, H. and Nilsson, T. (2013) 'GPT2: Empirical slant delay model for radio space geodetic techniques', *Geophysical Research Letters*, 40(6), pp. 1069-1073.

Landau, H. (1989) 'Precise kinematic GPS positioning - Experiences on a land vehicle using TI 4100 receivers and software', *Bulletin Géodésique*, 63(1), pp. 85-96.

Leandro, R.F., Langley, R.B. and Santos, M.C. (2008) 'UNB3m_pack: A neutral atmosphere delay package for radiometric space techniques', *GPS Solutions*, 12(1), pp. 65-70.

Leandro, R.F., Santos, M.C. and Navstar (2006) 'Wide area based precise point positioning', *Proceedings of the 19th International Technical Meeting of the Satellite Division of the Institute of Navigation, ION GNSS 2006*. pp. 2272-2278.

Lee, S.-W., Kouba, J., Schutz, B., Kim, D.H. and Lee, Y.J. (2013) 'Monitoring precipitable water vapor in real-time using global navigation satellite systems', *Journal of Geodesy*, 87(10-12), pp. 923-934.

Li, P. and Zhang, X. (2014) 'Integrating GPS and GLONASS to accelerate convergence and initialization times of precise point positioning', *GPS Solutions*, 18(3), pp. 461-471.

Li, X., Dick, G., Ge, M., Heise, S., Wickert, J. and Bender, M. (2014) 'Real-time GPS sensing of atmospheric water vapor: Precise point positioning with orbit, clock, and phase delay corrections', *Geophysical Research Letters*, 41(10), pp. 3615-3621.

Li, Z., Muller, J.P. and Cross, P. (2003) 'Comparison of precipitable water vapor derived from radiosonde, GPS, and Moderate-Resolution Imaging Spectroradiometer measurements', *Journal of Geophysical Research-Atmospheres*, 108(D20), 4651.

Li, Z., Muller, J.P., Cross, P. and Fielding, E.J. (2005) 'Interferometric synthetic aperture radar (InSAR) atmospheric correction: GPS, moderate resolution Imaging spectroradiometer (MODIS), and InSAR integration', *Journal of Geophysical Research-Solid Earth*, 110(B3), B03410.

Li, Z., Muller, J.P., Cross, P., Albert, P., Fischer, J. and Bennartz, R. (2006) 'Assessment of the potential of MERIS near-infrared water vapour products to correct ASAR interferometric measurements', *International Journal of Remote Sensing*, 27(2), pp. 349-365.

Li, Z., Fielding, E. J., & Cross, P. (2009) 'Integration of InSAR time series analysis and water vapour correction for mapping postseismic deformation after the 2003 Bam, Iran Earthquake', *IEEE Transactions on Geoscience and Remote Sensing*, 47(9), pp. 3220-3230.

Li, Z., Elliott, J., Feng, W., Jackson, J., Parsons, B., Walters, R. (2011) 'The 2010 MW 6.8 Yushu (Qinghai, China) earthquake: constraints provided by InSAR and body wave seismology', *Journal of Geophysical Research: Solid Earth,* 116(B10), B10302.

Liou, Y.A., Huang, C.Y. and Teng, Y.T. (2000) 'Precipitable water observed by ground-based GPS receivers and microwave radiometry', *Earth Planets and Space*, 52(6), pp. 445-450.

Liu, J., Liang, H., Sun, Z. and Zhou, X. (2006) 'Validation of the Moderate-Resolution Imaging Spectroradiometer precipitable water vapor product using measurements from GPS on the Tibetan Plateau', *Journal of Geophysical Research-Atmospheres*, 111, D14103.

Liu, X. (2008) 'Airborne LiDAR for DEM generation: some critical issues', *Progress in Physical Geography*, 32(1), pp. 31-49.

Liu, Y., Chen, Y. and Baki Iz, H. (2000) 'Precision of precipitable water vapour from radiosonde data for GPS solutions', *Geomatica*, 54(2), pp. 171-175.

Lock, A.P., Brown, A.R., Bush, M.R., Martin, G.M. and Smith, R.N.B. (2000) 'A new boundary layer mixing scheme. Part I: Scheme description and single-column model tests', *Monthly Weather Review*, 128(9), pp. 3187-3199.

Lyard, F., Lefevre, F., Letellier, T. and Francis, O. (2006) 'Modelling the global ocean tides: Modern insights from FES2004', *Ocean Dynamics*, 56, pp. 394-415.

Macpherson, S.R., Deblonde, G. and Aparicio, J.M. (2008) 'Impact of NOAA ground-based GPS observations on the Canadian regional analysis and forecast system', *Monthly Weather Review*, 136(7), pp. 2727-2746.

Marreiros, P., Joana Fernandes, M. and Bastos, L. (2013) 'Evaluating the feasibility of GPS measurements of SSH on board a ship along the Portuguese West Coast', *Advances in Space Research*, 51(8), pp. 1492-1501.

Martín, A., Anquela, A.B., Berne, J.L. and Sanmartin, M. (2012) 'Kinematic GNSS-PPP results from various software packages and raw data configurations', *Scientific Research and Essays*, 7(3), pp. 419-431.

Martin, I. (2013) *GNSS precise point positioning: The enhancement with GLONASS*. Ph.D thesis. School of Civil Engineering and Geosciences, Newcastle University.

McCarthy, D.D. and Petit, G. (2004) 'IERS Conventions 2003', *IERS Technical Note 32*.

McCarthy, D. D., and B. Luzum (2010), IERS Conventions (2010), *IERS Technical Note* No. 36, ISSN 1019-4568.

McMillin, L.M., Zhao, J., Raja, M.K.R.V., Gutman, S.I. and Yoe, J.G. (2007) 'Radiosonde humidity corrections and potential Atmospheric Infrared Sounder moisture accuracy', *Journal of Geophysical Research-Atmospheres*, 112, D13S90.

Mendes, V.B., Collins, J.P. and Langley, R.B. (1995) 'The Effect ofTropospheric Propagation Dela Errors in Airborne GPS Precision Positioing', *ION GPS-95, 8th International Technical Meeting of teh Satellite Division of the Institute of Navigation*. Palm Springs, CA, 12-15 September 1995.

Middleton, J.H., Cooke, C.G., Kearney, E.T., Mumford, P.J., Mole, M.A., Nippard, G.J., Rizos, C., Splinter, K.D. and Turner, I.L. (2013) 'Resolution and accuracy of an airborne scanning laser system for beach surveys', *Journal of Atmospheric and Oceanic Technology*, 30(10), pp. 2452-2464.

Moninger, W.R., Mamrosh, R.D. and Pauley, P.M. (2003) 'Automated meteorological reports from commercial aircraft', *Bulletin of the American Meteorological Society*, 84(2), pp. 203-216.

Montenbruck, O., Hauschild, A., Steigenberger, P., Hugentobler, U., Teunissen, P. and Nakamura, S. (2013) 'Initial assessment of the COMPASS/BeiDou-2 regional navigation satellite system', *GPS Solutions*, 17(2), pp. 211-222.

Niell, A.E. (1996) 'Global mapping functions for the atmosphere delay at radio wavelengths', *Journal of Geophysical Research-Solid Earth*, 101(B2), pp. 3227-3246.

Niell, A.E., Coster, A.J., Solheim, F.S., Mendes, V.B., Toor, P.C., Langley, R.B. and Upham, C.A. (2001) 'Comparison of measurements of atmospheric wet delay by radiosonde, water vapor radiometer, GPS, and VLBI', *Journal of Atmospheric and Oceanic Technology*, 18(6), pp. 830-850.

Ning, T., Haas, R., Elgered, G. and Willen, U. (2012) 'Multi-technique comparisons of 10 years of wet delay estimates on the west coast of Sweden', *Journal of Geodesy*, 86(7), pp. 565-575.

Pan, L., Cai, C., Santerre, R., Zhu, J., (2014) 'Combined GPS/GLONASS precise point positioning with fixed GPS ambiguities' *Sensors,* 14, pp. 17530-17547

Parkinson, C.L. (2003) 'Aqua: An Earth-observing satellite mission to examine water and other climate variables', *Ieee Transactions on Geoscience and Remote Sensing*, 41(2), pp. 173-183.

Paroscientific (2009) *Digiquartz® Pressure Instrumentation User's Manual for Model 735 Intelligent Display And Model 745 High Accuracy Laboratory Standard* [Online]. Available at: http://www.paroscientific.com/manuals/8004-001.pdf.

Paroscientific (2011) *Digiquartz® pressure instrumentation: Broadband meteorological measurement systems*. [Online]. Available at: http://www.paroscientific.com/pdf/met4DataSheet.pdf.

Penna, N.T., Bos, M.S., Baker, T.F. and Scherneck, H.G. (2008) 'Assessing the accuracy of predicted ocean tide loading displacement values', *Journal of Geodesy*, 82, pp. 893-907.

Petrie, E.J., Hernandez-Pajares, M., Spalla, P., Moore, P. and King, M.A. (2011) 'A review of higher order ionospheric refraction effects on dual frequency GPS', *Surveys in Geophysics*, 32(3), pp. 197-253.

Píriz, R., Calle, D., Mozo, A., Navarro, P., Rodríguez, D. and Tobías, G. (2009) 'Orbits and clocks for GLONASS precise-point-positioning', *22nd International Technical Meeting of the Satellite Division of the Institute of Navigation 2009, ION GNSS 2009*. pp. 1812-1821.

Poli, P., Moll, P., Rabier, F., Desroziers, G., Chapnik, B., Berre, L., Healy, S.B., Andersson, E. and El Guelai, F.Z. (2007) 'Forecast impact studies of zenith total delay data from European near real-time GPS stations in Metéo France 4DVAR', *Journal of Geophysical Research*, 112, D06114.

Prasad, A.K. and Singh, R.P. (2009) 'Validation of MODIS Terra, AIRS, NCEP/DOE AMIP-II Reanalysis-2, and AERONET Sun photometer derived integrated precipitable water

vapor using ground-based GPS receivers over India', *Journal of Geophysical Research-Atmospheres*, 114, D05107.

Raja, M.K.R.V., Gutman, S.I., Yoe, J.G., McMmillin, L.M. and Zhao, J. (2008) 'The validation of AIRS retrievals of integrated precipitable water vapor using measurements from a network of ground-based GPS receivers over the contiguous United States', *Journal of Atmospheric and Oceanic Technology*, 25(3), pp. 416-428.

Rocken, C., Johnson, J., Van Hove, T. and Iwabuchi, T. (2005) 'Atmospheric water vapor and geoid measurements in the open ocean with GPS', *Geophysical Reasearch letters*, 32, L12813.

Rocken, C., Van Hove, T. and Ware, R. (1997) 'Near real-time GPS sensing of atmospheric water vapor', *Geophysical Research Letters*, 24(24), pp. 3221-3224.

Rocken, C., Vanhove, T., Johnson, J., Solheim, F., Ware, R., Bevis, M., Chiswell, S. and Businger, S. (1995) 'GPS/STORM-GPS sensing of atmospheric water-vapor for meteorology', *Journal of Atmospheric and Oceanic Technology*, 12(3), pp. 468-478.

Saastamoinen, J. (1972) 'Atmospheric correction for the troposphere and stratosphere in radio ranging of satellites', in Henriksen, S.W., Mancini, A. and Chovitz, B.H. (eds.) *The Use of Artificial Satellites for Geodesy, Geophys. Monogr.* Washington, D. C.: AGU, pp. 247-251.

Santerre, R. (1991) 'Impact of GPS satellite sky distribution', *Manuscripta Geodaetica*, 16, pp. 28-53.

Schmid, R., Steigenberger, P., Gendt, G., Ge, M. and Rothacher, M. (2007) 'Generation of a consistent absolute phase-center correction model for GPS receiver and satellite antennas', *Journal of Geodesy*, 81(12), pp. 781-798.

Shan, S., Bevis, M., Kendrick, E., Mader, G.L., Raleigh, D., Hudnut, K., Sartori, M. and Phillips, D. (2007) 'Kinematic GPS solutions for aircraft trajectories: Identifying and minimizing systematic height errors associated with atmospheric propagation delays', *Geophysical Research Letters*, 34, L23S07.

Shi, J. and Cannon, M.E. (1995) 'Critical error effects and analysis in carrier phase-based airborne gps positioning over large areas', *Bulletin Geodesique*, 69(4), pp. 261-273.

Skaloud, J. (2002) 'Direct georeferencing in aerial photogrammetric mapping', *Photogrammetric Engineering and Remote Sensing*, 68(3), pp. 207-210.

Skone, S., Gao, Y., Al-Fanek, O., Tao, W., Zhang, Y., Heroux, P. and Collins, P. (2006) 'Atmospheric moisture estimation using GPS on a moving platform', *Proceedings of*

*the 19th International Technical Meeting of the Satellite Division of the Institute of Navigation, ION GNSS 2006*, pp. 1891-1901.

Smith, E.K. and Weintraub, S. (1953) 'The constants in the equation for atmospheric refractive index at radio frequencies', *Proceedings of the IRE*, 41(8), pp. 1035-1037.

Smith, T.L., Benjamin, S.G., Gutman, S.I. and Sahm, S. (2007) 'Short-range forecast impact from assimilation of GPS-IPW observations into the Rapid Update Cycle', *Monthly Weather Review*, 135(8), pp. 2914-2930.

Springer, T., Schönemann, E., Agrotis, L., Dilssner, F. and Enderle, W. (2013) 'GNSS analysis in a multi-GNSS and multi-signal environment', *AGU 2013 Fall meeting*. San Fransico, CA.

Stewart, M.P., Penna, N.T. and Lichti, D.D. (2005) 'Investigating the propagation mechanism of unmodelled systematic errors on coordinate time series estimated using least squares', *Journal of Geodesy*, 79(8), pp. 479-489.

Teke, K., Nilsson, T., Boehm, J., Hobiger, T., Steigenberger, P., Garcia-Espada, S., Haas, R. and Willis, P. (2013) 'Troposphere delays from space geodetic techniques, water vapor radiometers, and numerical weather models over a series of continuous VLBI campaigns', *Journal of Geodesy*, 87(10-12), pp. 981-1001.

Teng, W.-H., Huang, C.-Y., Ho, S.-P., Kuo, Y.-H. and Zhou, X.-J. (2013) 'Characteristics of global precipitable water in ENSO events revealed by COSMIC measurements', *Journal of Geophysical Research-Atmospheres*, 118(15), pp. 8411-8425.

Thomas, I.D., King, M.A., Clarke, P.J. and Penna, N.T. (2011) 'Precipitable water vapor estimates from homogeneously reprocessed GPS data: An intertechnique comparison in Antarctica', *Journal of Geophysical Research-Atmospheres*, 116, D04107.

Tiemeyer, B., Cannon, M. E., Lachapelle, G., Schanzer, G. (1994) 'Satellite navigation for high-precision aircraft navigation with emphasis on atmospheric effects', *IEEE 1994 Position Location and Navigation Symposium*, pp. 394-401.

Tomás, R., Li, Z., Liu, P., Singleton, A., Hoey, T., Cheng, X. (2014) 'Spatiotemporal characteristics of the Huangtupo landslide in the Three Gorges region (China) constrained by radar interferometry', *Geophysical Journal International*, 197(1), pp. 213-232.

Tralli, D.M., Dixon, T.H. and Stephens, S.A. (1988) 'Effect of wet tropospheric path delays on estimation of geodetic baselines in the gulf of california using the global positioning system', *Journal of Geophysical Research-Solid Earth and Planets*, 93(B6), pp. 6545-6557.

Utsumi, N., Seto, S., Kanae, S., Maeda, E.E. and Oki, T. (2011) 'Does higher surface temperature intensify extreme precipitation?', *Geophysical Research Letters*, 38, L16708.

Vey, S., Dietrich, R., Ruelke, A., Fritsche, M., Steigenberger, P. and Rothacher, M. (2010) 'Validation of precipitable water vapor within the NCEP/DOE reanalysis using global GPS observations from one decade', *Journal of Climate*, 23(7), pp. 1675-1695.

Vomel, H., Selkirk, H., Miloshevich, L., Valverde-Canossa, J., Valdes, J., Kyroe, E., Kivi, R., Stolz, W., Peng, G. and Diaz, J.A. (2007) 'Radiation dry bias of the vaisala RS92 humidity sensor', *Journal of Atmospheric and Oceanic Technology*, 24(6), pp. 953-963.

von Engeln, A. and Nedoluha, G. (2005) 'Retrieval of temperature and water vapor profiles from radio occultation refractivity and bending angle measurements using an Optimal Estimation approach: a simulation study', *Atmospheric Chemistry and Physics*, 5, pp. 1665-1677.

Wallace, J.M. and Hobbs, P.V. (1977) *Atmospheric science: An introductory Survey*. Orlando, Florida: Academic Press, Inc.

Wallace, J.M., Lim, G.H. and Blackmon, M.L. (1988) 'Relationship between cyclone tracks, anticyclone tracks and baroclinic wave-guides', *Journal of the Atmospheric Sciences*, 45(3), pp. 439-462.

Wang, B. and Ding, Q.H. (2006) 'Changes in global monsoon precipitation over the past 56 years', *Geophysical Research Letters*, 33(6), L06711.

Wang, J. and Zhang, L. (2008) 'Systematic errors in global radiosonde precipitable water data from comparisons with ground-based GPS measurements', *Journal of Climate*, 21(10), pp. 2218-2238.

Wang, J., Zhang, L., Dai, A., Immler, F., Sommer, M. and Voemel, H. (2013) 'Radiation dry bias correction of Vaisala RS92 humidity data and its impacts on historical radiosonde data', *Journal of Atmospheric and Oceanic Technology*, 30(2), pp. 197-214.

Wang, J., Zhang, L., Dai, A., Van Hove, T. and Van Baelen, J. (2007) 'A near-global, 2-hourly data set of atmospheric precipitable water from ground-based GPS measurements', *Journal of Geophysical Research-Atmospheres*, 112, D11107.

Webb, S.R., Penna, N.T., Clarke, P.J., Webster, S., Martin, I. and Bennitt, G. (2014) 'Estimation of zenith wet delay using kinematic GNSS precise point positioning over a range of altitudes', *journal of atmospheric and Oceanic Technology, [in review]*.

Wen, Y., Li, Z., Xu, C., Ryder, I., Bürgmann, R. (2012) 'Postseismic motion after the 2001 Mw 7.8 Kokoxili earthquake in Tibet observed by InSAR time series', *Journal of Geophysical Research: Solid Earth*, 117(B8), B08405.

Wentz, F.J. and Schabel, M. (2000) 'Precise climate monitoring using complementary satellite data sets', *Nature*, 403(6768), pp. 414-416.

Whiteman, D.N., Demoz, B., Di Girolamo, P., Comer, J., Veselovskii, I., Evans, K., Wang, Z., Cadirola, M., Rush, K., Schwemmer, G., Gentry, B., Melfi, S.H., Mielke, B., Venable, D. and Van Hove, T. (2006) 'Raman lidar measurements during the International H2O Project. Part I: Instrumentation and analysis techniques', *Journal of Atmospheric and Oceanic Technology*, 23(2), pp. 157-169.

Williams, S.D.P. and Penna, N.T. (2011) 'Non-tidal ocean loading effects on geodetic GPS heights', *Geophysical Research Letters*, 38, p. L09314.

Wilson, D.R. and Ballard, S.P. (1999) 'A microphysically based precipitation scheme for the UK Meteorological Office Unified Model', *Quarterly Journal of the Royal Meteorological Society*, 125(557), pp. 1607-1636.

Wolfe, D.E. and Gutman, S.I. (2000) 'Developing an operational, surface-based, GPS, water vapor observing system for NOAA: Network design and results', *Journal of Atmospheric and Oceanic Technology*, 17(4), pp. 426-440.

Zhang, X. and Forsberg, R. (2007) 'Assessment of long-range kinematic GPS positioning errors by comparison with airborne laser altimetry and satellite altimetry', *Journal of Geodesy*, 81(3), pp. 201-211.

Zhao, S. H., Lu, X. S., Wang, Q. F., Hu, G. R., Ogaja, C. (2009) 'Analysis and evaluation of various tropospheric modeling approaches for high-precision GPS kinematic positioning over medium ranges and at high altitudes: Case study', *Journal of Surveying Engineering,* 135(2), pp. 66-71.

Zumberge, J.F., Heflin, M.B., Jefferson, D.C., Watkins, M.M. and Webb, F.H. (1997) 'Precise point positioning for the efficient and robust analysis of GPS data from large networks', *Journal of Geophysical Research-Solid Earth*, 102(B3), pp. 5005-5017.